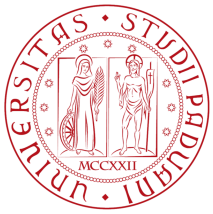

UNIVERSITÀ DEGLI STUDI DI PADOVA

Department of Civil, Environmental and Architectural Engineering

Master degree in Environmental Engineering

Master thesis

Modeling the consolidation of coastal marshes in the Venice Lagoon by a coupled 3D mixed finite element approach

Supervisor

Prof. Eng. Pietro Teatini

Co-supervisors

Dr. Eng. Claudia Zoccarato

Candidate

Francesco Gatto

2025879

Academic Year 2022/2023

Contents

List of Figures

List of Tables

1 Introduction

Salt marshes are coastal landforms that are flooded during high tides. They develop and thicken with soils mainly composed of clay, silty clay and peat. Worldwide, salt marshes provide key ecosystem services to coastal communities such as carbon sequestration [1](they can sequester and store carbon at efficient rates), trophic enrichment of coastal waters, nursery areas for fish species, permanent or transient habitat for aquatic invertebrates, and resting areas for migratory birds [2]. Salt marshes also protect shorelines from erosion by buffering wave action and trapping sediments [3]. The estimated total value of these ecosystem services is disproportionately high given that salt marshes cover less than 1% the of Earth's surface.

Salt marshes are threatened by multiple anthropogenic pressures such as freshwater inflow reduction, land-use change, and development resulting in fragmentation and habitat loss, biological invasions, and pollution. Furthermore, salt marshes are threatened by natural hazards such as sea storms, flooding, and sea-level rise, which are predicted to increase in intensity and frequency with climate change. It is estimated that since the mid-20th century, the world's salt marshes have being lost at a rate of 1–2% annually, resulting on an estimated loss of about 35% between 1970 and 2015 worldwide [4].

Long-term survivability of coastal marshes is largely dependent on their capability to gain elevation and keep up with relative sea-level rise. Several factors influence the vertical accretion of coastal marshes such as the deposition of sediments brought over the marsh platform by the lagoon water during high tide condition and the biochemical processes responsible for the decomposition of the organic matter. Also, the presence of alophyte plants the influence mineral sediment deposition by slowing water velocities, and add organic matter to the soil surface [5].

Natural compaction (autocompaction) of recently deposited sediments is one of the most important processes controlling marshes accretion. A recent study over East River Marsh (Connecticut, USA) assessed the contribution of mechanical compression and biodegradation to compaction of salt-marsh sediments and their subsequent influence on relative sea level (RLS) reconstructions [6]. From the comparison between RSL reconstruction from a sediment core and a previously-published RSL reconstruction

obtained from compaction-free basal sediments the authors observed a significant difference in reconstructions between 1100 and 1800 CE (Common Era). They concluded that the observed differences between the records can feasibly be attributed only to sediment compaction of the core.

Other recent studies started to demonstrate that subsurface processes (eg. soil compaction, pore pressure change) exert important influence on platform elevation in many wetland systems [7] [8].

To quantify the loss of surface elevation of the marsh platforms due to sediments autocompaction it is necessary to characterize the geomechanical properties of these soils. These soils are very susceptible to compaction. They are composed by clay, silt and sand in different fractions with an organic content that may be very high (Loss of Ignition, LOI 50%), in particular at shallow depths. Laboratory tests (shear test, oedometric test) are generally used to characterize the geomechanical properties of the soils composing salt marshes. A study conducted at Greatham Creek (Cowpen Marsh, Tees Estuary, UK) on different sediment samples [9], aimed to investigate the one-dimensional compression behavior, revealed that soil heterogeneity largely affects the soil behavior in compression. For example soils with higher initial voids ratios are more compressible than samples with initially denser structures.

Marsh soils behavior to compression depends significantly on preconsolidations stresses, i.e. the maximum effective stress experienced by the soil during its life. If the effective stress remains below the preconsolidation threshold, the soil behaves as an elastic material. If this value is surpassed its behavior become plastic, i.e. characterized by permanent deformation even after the soil is unloaded. Analysis of physical properties and oedometer compression tests demonstrates that, contrary to the general assumptions of existing models, sediments composing salt marsh landforms exhibit varying degrees of overconsolidation, paricularly due to desiccation [9]. A study conducted on sediments collected from two marshes at Tillingham marsh, East England and Warton marsh, Northwest England, revealed that, due to high stresses measured, even under the worst possible conditions vertical total stresses applied by storm surges would not be able to produce irrecoverable displacement, as has been observed in some US marshes [10].

In addiction to the preconsolidation stress, sediment compaction process is controlled by

many other factors. Organic content exerts a key control on the structure, density and compressibility of intertidal sediments with statistically significant relationships between LOI and initial voids ratio and compression indices [11]. Flooding frequency and duration, and eco-sedimentary conditions, such as the presence or absence of surface biomass are also important factors influencing salt marshes compaction [11].

The main issue on the laboratory tests is that the reliability of the results is intrinsically related to the disturbance of soil samples collected in-situ. However, the reliability of lab tests outcomes is largely questionable on loose soils as those composing salt marshes. To overcome this problem and to characterize the hydro-geomechanical parameters governing marsh autocompaction, a series of in-situ loading experiments was conducted in different sites of the Venice Lagoon [12]. The experiments were aimed to monitor marshes compaction in terms of vertical displacements and pressure change in undisturbed conditions under a controlled load. The final goal of these tests is to understand the mechanical response to external stressors of these recently deposited compressible soils in terms of vertical displacements. This information will allow to anticipate the fate of tidal marshes which is threatened by the future sea level rise, land subsidence, and possible changes of sediment availability.

The aim of this thesis is to analyse these in-situ experiments to characterize the salt marshes from a geomechanical view point and to understand which are the most important parameters driving their compaction. Subsequently, a numerical model solving the coupled groundwater flow and equilibrium equations in a 3D setting using a mixed finite element approach has been implemented to interpret the in-situ experiments. The datasets are described in details, followed by a presentation of the modelling approach. Finally the calibration procedure adopted to match the measurements is shown and the results discussed. A discussion session provides a summary of the most important parameters derived to characterize the hydro-geomechanical behaviors of the salt marshes in the Venice Lagoon.

2 Study area: the Venice Lagoon

The experiments were conducted on few salt marshes within the Venice Lagoon (Fig. 2.1). The natural salt marshes are intertidal environments, whose terrain is subject to alternating submersion and emersion as a result of normal tidal fluctuations [13]. In natural salt marshes, the tide initially spreads along the sinuous branches of the canals, becoming more and more subtle entering the minor creeks (the "ghebi") and the small internal unvegetated zones (the "chiari"), providing the vital functions of the lagoon. The alternated presence of small ponds, channels and vegetation made it difficult to carry out the experiments. F Each salt marsh is characterised by a specific sediment stratification and a zonation of the type of vegetation [5]. The majority of the sediments accreting the salt marsh platform derives from the marsh border erosion and from the bottom of the lagoon, transported by waves, tides and hydrodynamic processes [14]. The silt is combined with clay and sand, creating an heterogeneous interbedding stratigraphy with different thicknesses [15]. Moreover, the peculiarity of this kind of environment is the presence of low vegetation with its root zone extending up to approximately 20 cm from the surface.

Soil stratigraphy varies from site to site according to the quantity and quality of sediments deposited over the marsh platform over time. The continuous sediments deposition and autocompaction makes salt marshes an ever-changing environment: the deep soil layers are subjected to the load of the new deposited sediments. As a result soil vertical profile is characterized by a deep layer which is more consolidated, than the superficial ones.

The experiments were conducted at La Grisa, Campalto, and Le Saline marshes (Fig. 2.1). Each of them is characterised by specific stratigraphy and geomechanical properties which will be discussed in the next sections. La Grisa marshland is located in the southern basin of the Venice Lagoon near Chioggia (VE), Campalto and Le Saline are located in the northern basin.

A dense network of monitoring stations were established in the Venice Lagoon. They record, for example, tidal fluctuations (e.g., at Punta della Salute, Fig. 2.1) and atmospheric pressure (e.g., Palazzo Cavalli,Fig. 2.1), which are two important quantities for the correct interpretation of the measurements acquired during the loading experiments.

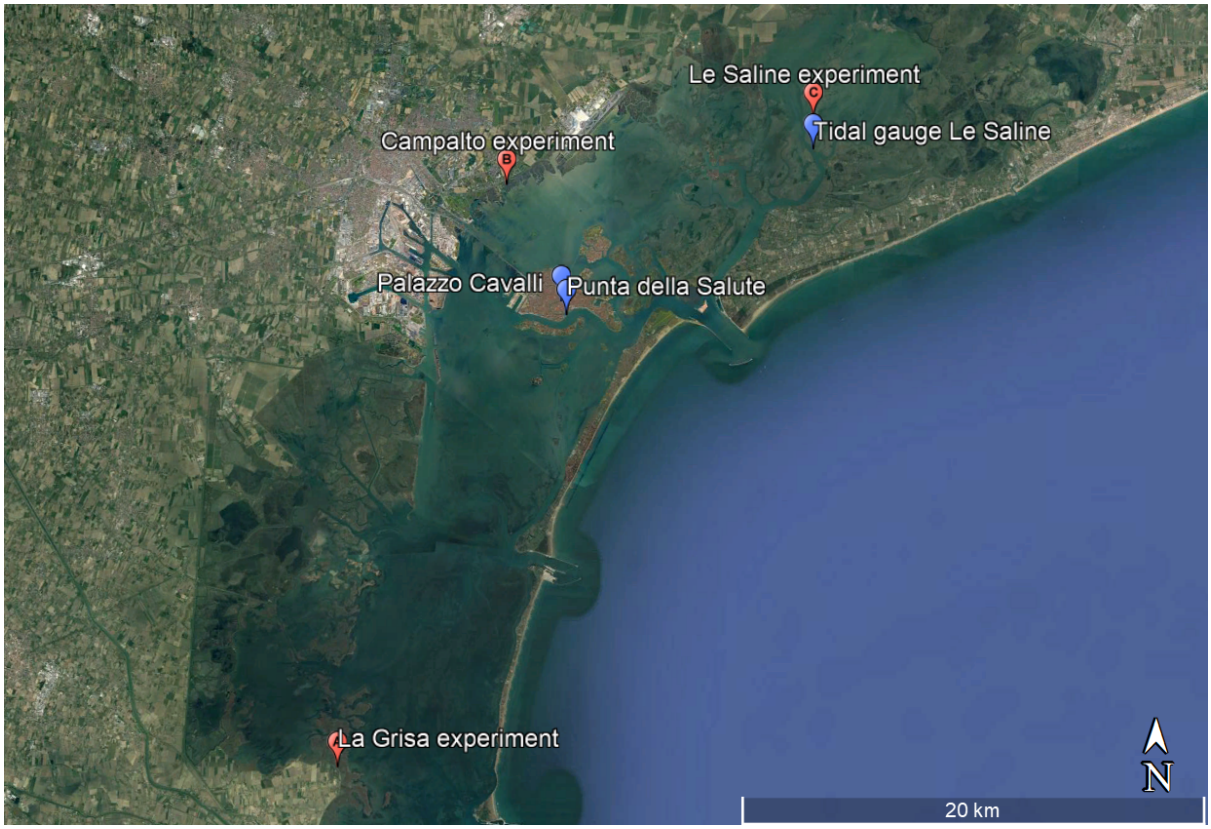

Figure 2.1: Map of the Venice Lagoon with the locations of the loading experiments, the tide gauges (Punta della Salute, Le Saline), and the atmospheric pressure station (Palazzo Cavalli).

2.1 Geological surveys

A number of shallow cores were carried out in the La Grisa, Campalto and Le Saline salt marshes to reconstruct the soil stratigraphy. The sedimentological analyses along a few transects revealed the stratigraphic lateral variability of the sites. In each site the upper 20 cm thickness mainly consist of organic material rich in roots and plants remains. The abundance of organic material highlights that the main source of accretion for these salt marshes is controlled by organic matter production, with the deposition of inorganic sediments transported by wave action and tide being more limited. Below the root zone the soil stratigraphy of the three sites is very different.

2.1.1 La Grisa

Fig. 2.2 shows the lithological sequence at La Grisa. Below the root zone (20 cm), moving from top to bottom, soil is characterized by 10 and 25 cm of silty with plant remains and silty-sand deposits. Below, there is a 45 cm layer of laminated very-fine sand to

silty clay with a fining upward trend. This kind of stratigraphy demonstrates the impact effect in the past of Brenta river on building-up the marsh in this area. This latter sediments were transported to the lagoon by the Brenta River when it flowed into the lagoon [16]. Subsequent diversion operations caused the input of inorganic sediment to decrease dramatically, resulting in a abundance of organic materials in the upper layers.

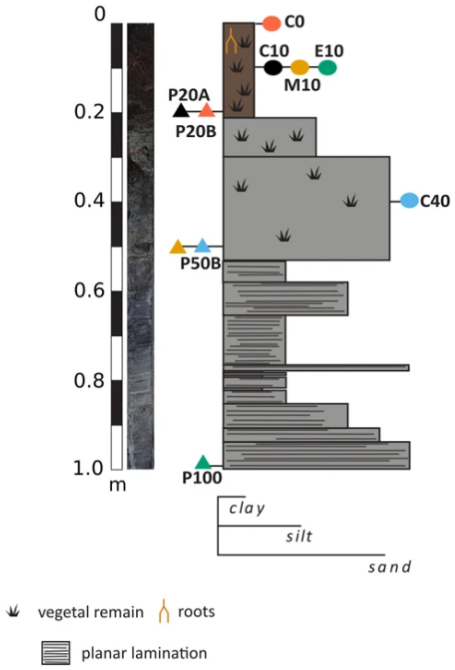

Figure 2.2: Soil stratigraphy at La Grisa. Modified after [12].

2.1.2 Campalto

The Campalto salt marshes have a peculiar history, they developed when dry land became part of the lagoon after the Osellino canal was built. The sedimentological analysis along a transect crossing the loading area, allow us to reconstruct the soil stratigraphy up to a depth of 150 cm below the ground level. The upper 10 cm, are characterized by a brownish silty clay with high organic content consisting of plants remains and roots. In the next 20 cm (depth from 10 to 30 cm) the organic content decreases with more silty clay goes from brown to gray. The layer from 30 to 63 cm below the ground level is composed by gray clay with few plants remains. The successive soil layers consist of silty clay with few organic content that becomes clayey silt in the deeper layers (113-134 cm). Other core drillings were carried out at different distances from the channel to investigate soil heterogeneity. Moving from areas of the salt marsh close to the lagoon bound towards the

tidal channel, the vertical soil profile varies significantly, expecially for the intermediate layers, with the depth of the consolidated layer (represented in yellow, Fig. 2.3) that almost doubles. This trend highlight that in areas of the salt marsh close to lagoon the amount new deposited material is higher if compared to the innermost areas: coastal areas are in fact more subjected to tidal oscillations and wave action that transport new sediments over the marsh platform.

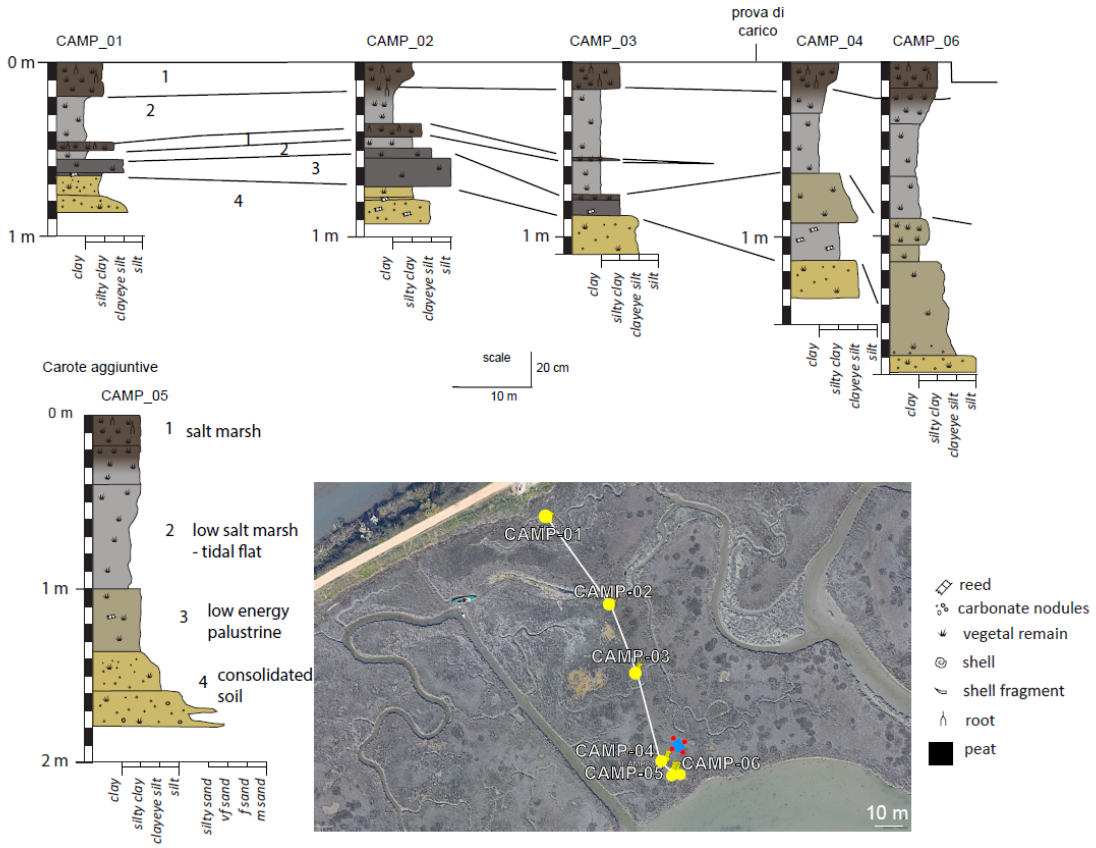

Figure 2.3: Stratigraphic soil profile at Campalto.

2.1.3 Le Saline

At Le Saline the experiment was conducted on a salt marsh close to Lio Piccolo. Unlike the other two sites, the salt marsh is entirely surrounded by water from the lagoon ensuring an higher exchange of sediments transported by water. The formation of this salt marsh is more recent than the two previously discussed. However, as in the precedent cases, the uppermost 20 cm are rich in organic material (roots and plant remains) which decreases with depth (Fig. 2.4). Below the first layer (0-20 cm), composed by clayey silt and organic material, three layers with a coarsening downward trend are detected: they are composed

by clayey silt (20-40 cm), silt (40-55 cm) and sandy silt (55-145 cm), respectively (Fig. 2.4). The deeper part (145-200 cm) consists of silty clay rich in shells and shell fragments and it's more consolidated than the shallower soil.

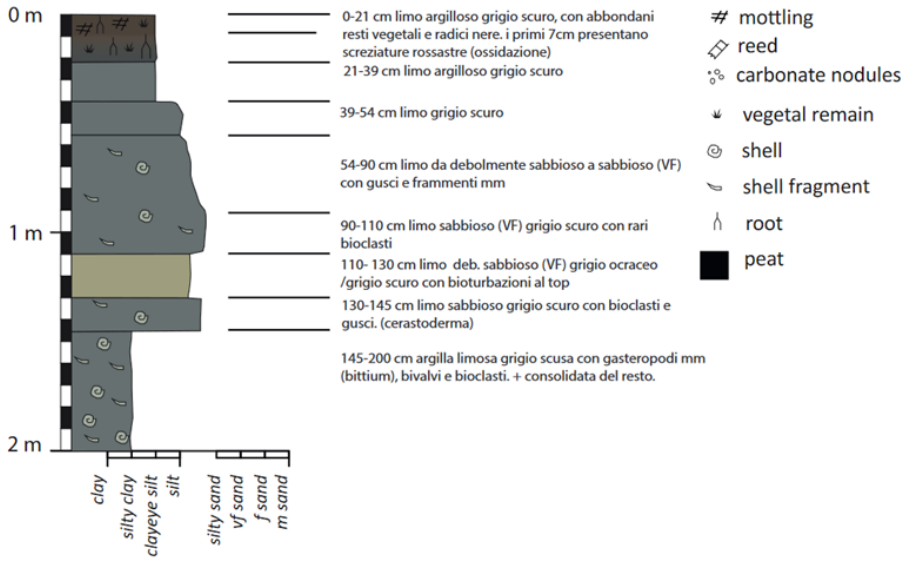

Figure 2.4: Stratigraphic soil profile at Le Saline.

2.2 Geotechnical investigations

A few soil samples were collected at La Grisa and Campalto, and characterized in the lab by traditional geotechnical tests. As discussed in the introduction (Section 1) the reliability of lab tests outcomes is largely questionable on loose soils as those composing salt marshes. The sampling of these soils is challenging due to the nature of the sediments that compose them. However, these tests give an insight of the geomechanical behavior of salt marshes. They provide an estimate of the most important geomechanical parameters to be used as initial guesses during the modeling procedure.

Oedometer tests are performed by applying different loads to a soil sample and measuring the deformation response. The results from these tests are used to investigate how a soil in the field will deform in response to a change in effective stress. The test is performed in the oedometer, which consists of a rigid steel ring inside which a cylindrical soil specimen (possibly taken from an undisturbed sample) is inserted. Porous septa are placed on the ends of the specimen to allow drainage of the water contained in the specimen along the vertical direction only. The whole is placed in a cell that is filled with water to constantly

maintain a fully saturated condition. A rigid plate is placed over the upper porous septum of the specimen where a vertical load is applied and progressively increased. The behavior vs time of the vertical settlement of the specimen is measured. The soil samples are subjected to loading-unloading phases.

2.2.1 La Grisa

Oedometric tests were performed on samples at 0.16, 0.65 and 0.8 m depth collected from La Grisa marsh. Before the implementation of the oedometric test, preliminary analysis on the soil samples were carried out to characterize the marsh soils. The specific weight of the solid grains was around 2.7 g/cm^3 and the initial void ratio was varying between 5 to 3 moving from depth of 0.16 m to 0.8 m.

The Table 2.1 displays the results of the oedometer test for the shallowest sample in term of deformations ϵ, void ratio e and oedometric modulus M.

The oedometric modulus M reported in Table 2.3 is given by the ratio between effective stress variation and volumetric deformations. At La Grisa, M varies from 0.05 to 0.87 MPa and between 2.27 and 9.14 MPa for 0.16 and 0.80 m depth, respectively. The testing stress ranged from 3 to 100 kPa.

The oedometric compressibility curve (Fig. 2.5) represents the relationship between void ratio and the vertical effective stress in a semi-logarithmic plot (Fig. 2.6) . From this chart, the following indexes can be obtained:

- C_c is the compression index and represent the slope of the curve during the loading phase
- C_r is the recompression index, i.e. the slope of the reloading part of the curve

Considering similar effective stress ranges maintained during the in-situ loading experiments introduce in Section 1 that will be described in the next Section 3 (5.6 kPa and 11.3 kPa) the values of the main indexes have been calculated for the 3 soil samples (Table 2.2). The value of C_c is 0.2 at 0.65 and 0.8 m depth. C_c could not be computed at 0.16 m due to a non-distinguishable single slope of the void index - effective stress curve (Fig. 2.5). The Cr values amount to 0.07 and 0.01 at 0.16 and 0.65 m depth, respectively. At 0.8 m depth C_r assumes a negative value, which is non-physical. The ratio

Step	σ_z (kPa)	ϵ (%)	e	M (MPa)
1	2.7	4.168	4.738	0.06
2	4.0	6.635	4.591	0.05
3	2.7	6.566	4.595	
4	4.0	6.573	4.594	
5	7.3	9.55	4.416	0.11
6	4.0	9.469	4.421	
7	7.3	9.782	4.402	
8	15.3	15.558	4.056	0.14
9	7.3	15.551	4.057	
10	15.3	15.588	4.055	
11	30.4	21.121	3.723	0.27
12	15.3	21.508	3.700	0.00
13	30.4	21.942	3.674	
14	123.0	42.041	2.471	0.87
15	60.6	41.925	2.477	
16	30.4	41.406	2.509	
17	15.3	41.113	2.526	
18	7.3	40.466	2.565	
19	2.7	40.238	2.578	

Table 2.1: Summary of the oedometric test carried out on the sample from La Grisa at depth 0.16 m

Depth from soil surface	C_c	C_r	s
0.16 m	/	0.07	/
0.65 m	0.2	0.01	20
0.80 m	0.2	/	/

Table 2.2: Oedometric indexes for the three soil samples collected from La Grisa salt marsh.

s of compressibility during loading (i.e., partially irreversible deformation) and unloading (i.e., only reversible deformation) can be estimated as $s = \frac{C_c}{C_r}$.

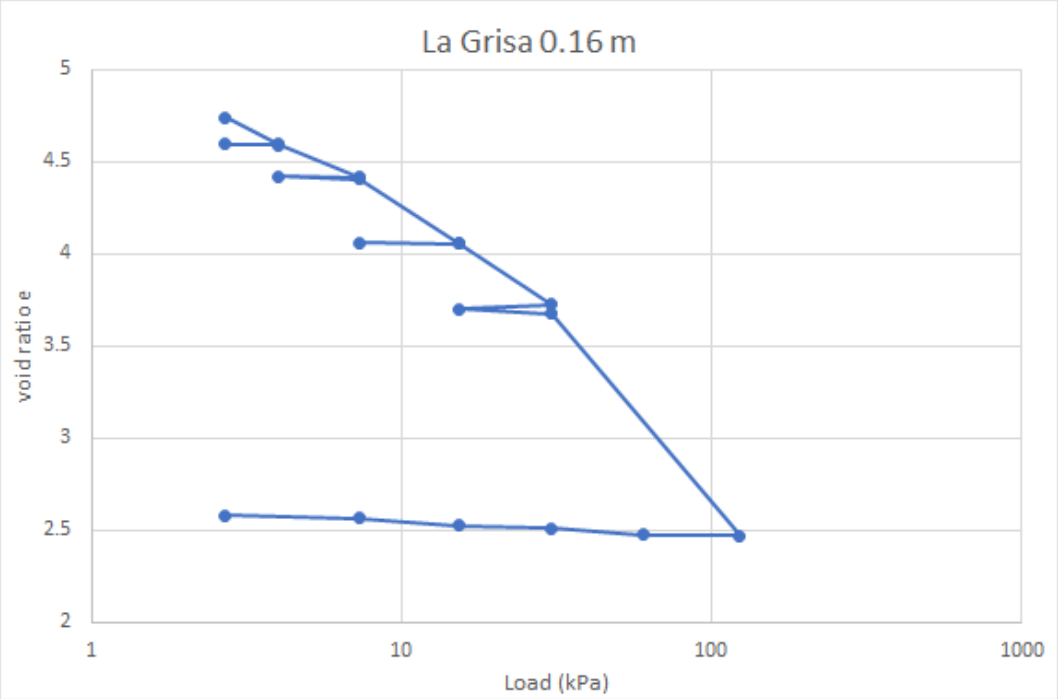

Figure 2.5: Oedometric compressibility curve for the soil sample at depth 0.16 m.

2.2.2 Campalto

The oedometric tests were carried out on three samples, collected at Campalto salt marsh, originally located at the depth ranges 0.03-0.05 m, 0.25-0.28 m and 0.5-0.53 m.

Before the implementation of test oedometric test, preliminary analysis on soil samples were carried out to characterize the marsh soils. An extremely high initial void ratio around 10 was obtained for the sample between depths 0.03 and 0.05 m. For deeper samples initial void ratios were around 2. The specific weight of solid grains of the three soil samples ranges between 2 and 3 g/cm^3.

The Table 2.3 displays the results of the oedometer test for the shallowest sample in term of deformations ϵ, void ratio e and oedometric modulus M.

The oedometric modulus M reported in Table 2.3 is given by the ratio between effective stress variation and volumetric deformations. It represents the soil stiffness and it varies with stress. M ranges from 0.1 to 1.16 MPa, from 0.42 to 2.86 MPa and between 0.53 and 2.36 MPa for 0.05, 0.25 and 0.5 m depth, respectively. The stress interval applied during the oedometric tests ranged from 2.4 to 123 kPa.

Considering similar effective stress ranges (5.6 kPa and 11.3 kPa) maintained during the in-

Step	σ_z (kPa)	ϵ (%)	e	M (MPa)
1	2.4	1.285	9.531	
2	4.0	2.429	9.409	0.14
3	8.0	4.809	9.155	0.17
4	16.0	13.122	8.269	0.10
5	32.5	23.326	7.180	0.16
6	16.0	23.125	7.201	
7	4.0	21.867	7.336	
8	8.0	21.895	7.333	
9	16.0	22.584	7.259	1.16
10	32.5	25.376	6.961	0.59
11	62.6	37.844	5.631	0.24
12	123.0	50.255	4.307	0.49
13	62.6	49.751	4.361	
14	16.0	46.209	4.739	

Table 2.3: Summary of the oedometric test carried out on the sample Campalto 0.03-0.05 m.

situ loading experiments introduced in Section 1 that will be described in the next Section 3 the values of the main indexes have been calculated for the 3 soil samples (Table 2.4). Oedometric laboratory experiments confirms that organogenic marshes (high LOI values) are always positively correlated with compression indices and void ratios, leading to higher consolidation rates compared to minerogenic marshes. The most superficial samples, rich in organic material (see Section 2.1) is indeed characterized by much higher values of compression and recompression indexes if compared to the deeper samples. The ratio s of compressibility during loading (i.e., partially irreversible deformation) and unloading (i.e.,

Depth from soil surface	Cc	Cr	s
0.03-0.05 m	2.94	0.130	23
0.25-0.28 m	0.20	0.018	11
0.50-0.53 m	0.11	0.018	6

Table 2.4: Oedometric indexes for the 3 soil samples collcted from Campalto salt marsh.

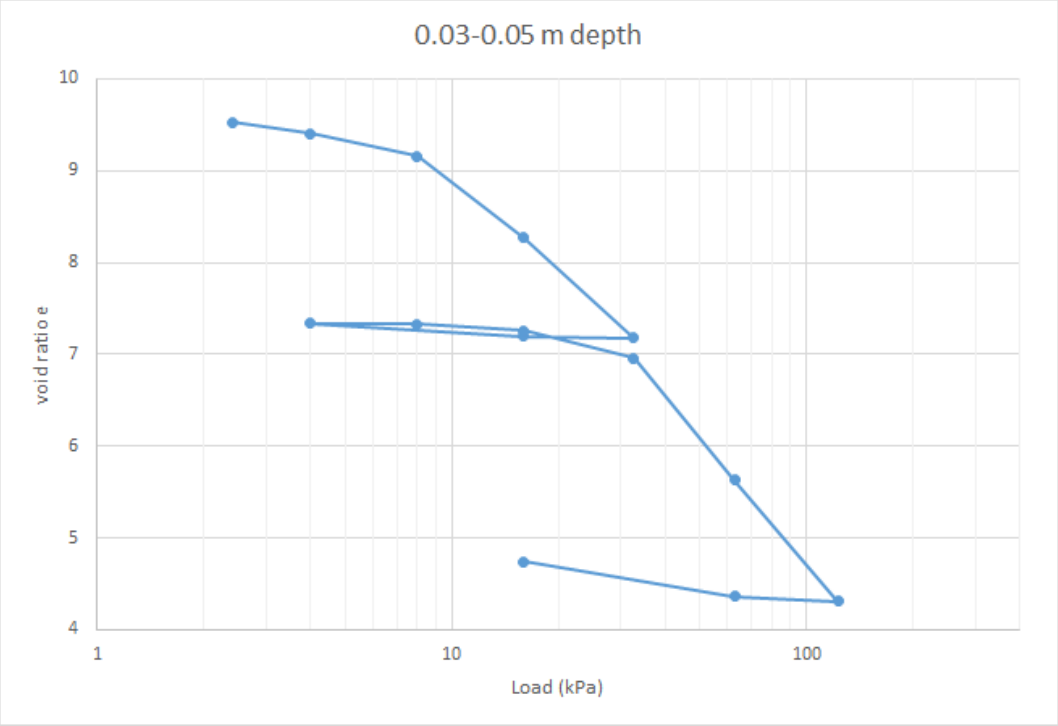

Figure 2.6: Oedometric compressibility curve for the soil sample at Campalto (depth 0.03-0.05 m).

only reversible deformation) decreases with depth as well as all the other indexes. The ratio s has been estimated as the ratio between compression and recompression indexes: $s = \frac{C_c}{C_r}$ For the considered samples the compressibility during the loading is much larger (about one oder of magnitude) than in the unloading phase.

3 The in-situ loading experiment

The consolidation model implemented in this thesis is built to interpret the in-situ experiments conducted in three marshlaands located within the Venice Lagoon, Italy, and charcterized by different depositional environments (Fig. 2.1). For few days, during the experiment, marsh compaction was monitored under a controlled loading condition.

3.1 Description of the in-situ experiments

The loading experiment has been carried out in different sites maintaining similar operating conditions. It consists of two loading-unloading phases:

1. In the first phase, a load of 5.6 kPa is applied within 15 minutes and maintained constant for $\sim$ 24 hours. Then, it is quickly removed.

2. The second phase starts after approximately one day from since the unloading phase. A load of 11.3 kPa is applied within 30 minutes and maintained for few days before the final unloading phase.

The loading phases are enough long to appreciate both primary and secondary consolidation processes. The experiment is built to emulate an oedometric lab test with the advantage that it is performed in undisturbed field conditions. The time span of the loading-unloading phases has been chosen as a compromise to monitor primary and secondary compression and contain the duration due to obvious logistic challenges in its management.

Eight 500-l polyethylene tanks, with dimensions $78\times69\times104$ cm^3, arranged in two rows of four tanks each filled with sea water pumped from the nearest creek are used to impose a constant load. The tanks can be filled accordingly to the desired load. During the first phase only the first row is filled with water while during the second phase all of them are filled. The tanks are equipped with caps which are opened during the unloading phases. Pumping and unloading procedures last approximately 15 minutes for the first phase and 30 minutes for the second one. The tanks are interconnected by plastic tubes to assure the same water level during the experiment stages, hence to guarantee a uniform load distribution. The tanks are placed on four wooden pallets positioned over a reinforced geotexile to guarantee a uniform load distribution on the marsh surface and reduce

buoyancy forces on the tanks in high tide conditions. This configuration allow to transfer the load on a surface large enough (around 4 m^2) to assume that deformations are basically only vertical (as in the oedometric test) at least below the central portion of the system. The marsh response accounts for and averages local-scale heterogeneities of the deposits which in general can't be smoothed at smaller spatial scales.

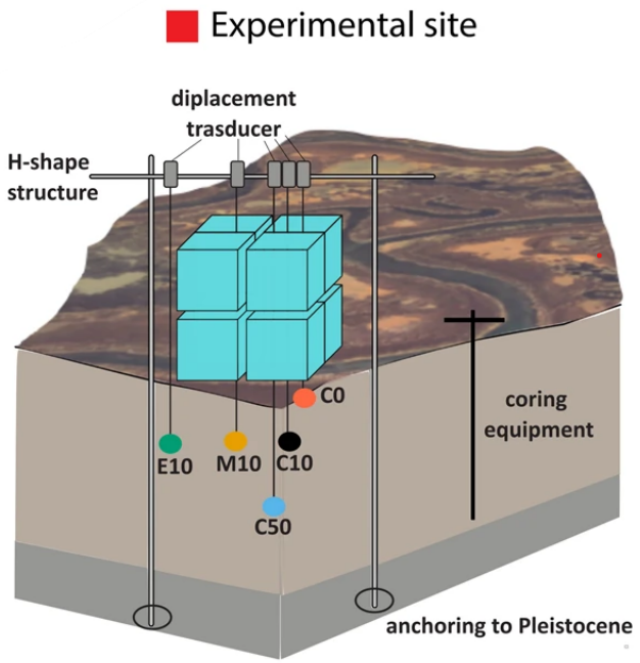

Figure 3.1: Sketch of the experimental set-up showing the position of the monitoring instruments and the H-shaped structure used as stable reference for the displacement transducers and anchored on the Pleistocene sediments (after [12]).

The experimental setup is equipped with a monitoring system consisting of both pressure transducers that record groundwater pressure and displacements transducers that measure vertical displacements. The sensors are positioned within the space left between the tanks. The displacements transducers are placed at different positions and depths: in correspondence of the load center, at the side of the loaded area and in an intermediate position on soil surface, at 0.1 m and 0.5 m below the marsh surface and they measure vertical displacements (Fig. 3.1). They are five (C0, C10, C50, E10, M10) in all the tests and they are encoded by using a capital letter that indicate their position with respect to the center of the loading area (C stands for central, E for external and m for middle) and

a number that express their deployment depth in centimeters (Fig. 3.3).

The experimental setups are equipped with six or five pressure loggers, according to the test, deployed at three different depths below the loading area: 0.2 m, 0.5 m and 1.0 m. The pressure transducers are identified by a capital letter "P" that indicates the type of sensor used, followed by a number which indicates the depth of location. Another capital letter at the end of the sensor acronym indicates the side of the experiment where they are placed (Fig. 3.3). Both displacements sensors and pressure transducers provide measures with a time resolution of one minute.

The next paragraph describes all the available data collected at the experimental sites that have been used to build up the model.

3.2 Available data

Model setup and its calibration require many empirical data. The data available for the model come from different sources:

- tidal data and atmospheric pressure;
- measurements of displacements and pressures from sensors during the experiments;
- geological surveys: litho-stratigraphy of the marshland subsurface described in the previous chapter;
- geotechnical investigations: oedometric tests described in the previous chapter.

3.3 Atmospheric and tidal data

The records of atmospheric pressure and tide are fundamental for the model calibration, expecially for the simulation of the evolution of the pore-water pressure during the loading experiments. The measures of pressure collected by the six pressure transducers during the test include also atmospheric pressure and the effect of tide which need to be removed to compare measures with model output.

In the experiments of Campalto, and la Grisa the tidal behaviour was recorded with a tidal gauge specifically established during the tests while at Le Saline site, the tidal data were collected from the closest station (Laguna Nord Le Saline, coordinates 45° 29'

44.13895" N, 12° 28' 19.09607" E) of the "Rete Telemareografica della Laguna di Venezia". All the tidal heights are referred to the same reference system which is tidal zero of Punta della Salute station (coordinates 45°25' 50.49" N, 12° 20' 11.97" E).

As concern records of atmospheric pressure, they are collected by the station of Palazzo Cavalli (coordinates 45° 26' 11.15679" N, 12° 20' 0.72675" E) (Fig. 2.1). Tidal oscillations were obtained subtracting the atmospheric pressure from the tidal gauge records.

3.4 Measures of displacements and pressure during the loading test

Data collected at the three loading test sites are illustrated in the next subsections.

3.4.1 La Grisa experiment

The experiment carried out in La Grisa (southern basin of the Venice Lagoon) took place from October 27, 2020 to November 2, 2020. The loading history was slightly different respect to the cases described in the next subsections. It was characterized by a longer second cycle which last one day more than in Le Saline and Campalto experiments while the first loading cycle and recovery period were equal (Fig. 3.2). The experiment consisted of two loading-unloading cycles:

- The first loading cycle started at 16:37 of October 27. A load of 5.6 kPa (first line of tanks was filled) has been imposed to the marsh in around 15 minutes and it lasted for about 22 hours. Then, the soil was completely unloaded.
- The second loading cycle started at 15:48 of October 29. The load of 11.3 kPa (all the tanks are filled with water) was imposed in around 30 minutes and maintained for 72 hours before the final unloading.

Five pressure transducers and five displacements transducers were placed in different positions of the loading area (Fig. 3.3) to measure pore-pressure change and vertical settlements induced by the load. Sensor C50 was placed at a deployment depth of 0.4 m due to the presence of a stiff-silty sand layer.

In the first loading phase, the load reached 5.6 kPa and it was kept constant for 24 hours.

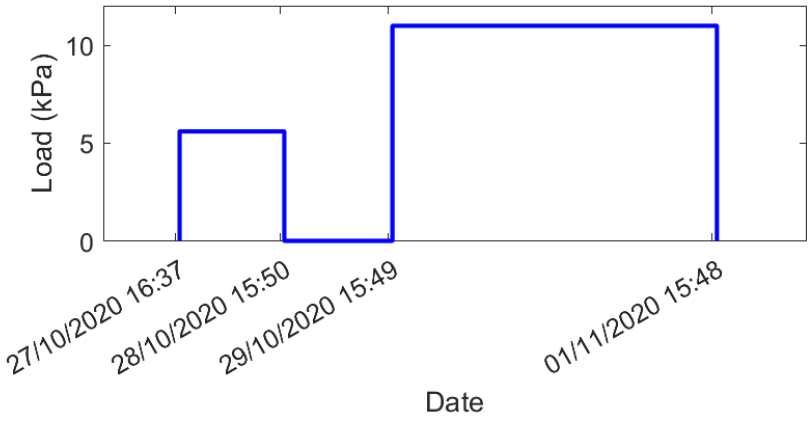

Figure 3.2: Load applied on the marsh surface following the various loading and unloading phases with the filling and emptying of the tanks.

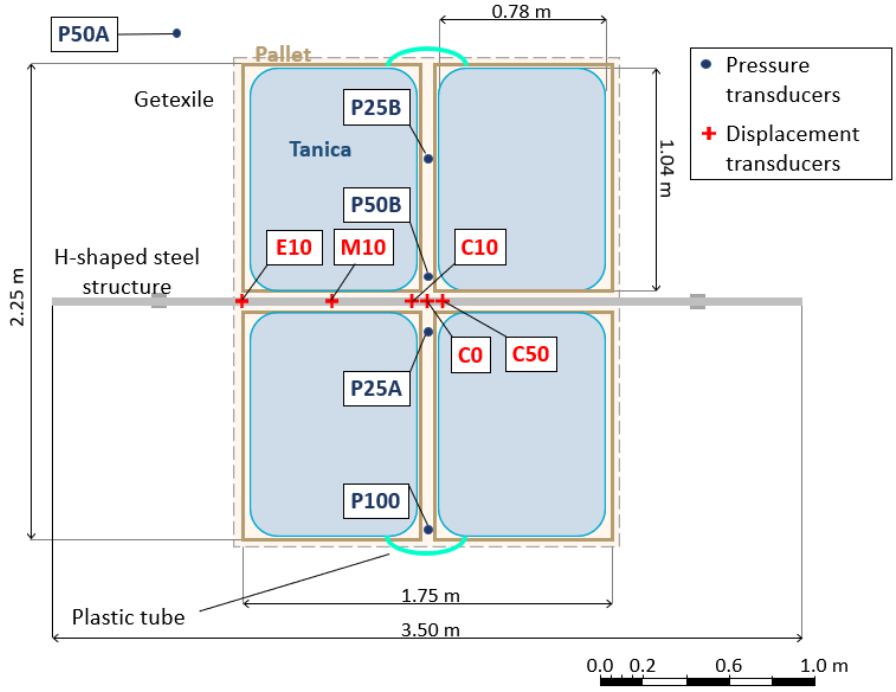

Figure 3.3: Plan view with dimensions, equipment (tanks, pallet, reference steel structure), location of the sensors to measure vertical displacements (red crosses) and pore-water pressure (blue dots). The sensor coding is representative of the deployment depth (in cm).

The black vertical lines in Fig. 3.4a represent the start of (un)loading phases. The maximum settlement of the marsh surface (sensor C0) equals 10.2 mm while sensors C10 and M10 measured 4.4 and 3.4 mm, respectively. Maximum displacements observed by sensors C50 and E10 were much lower and equal to 1.1 and 0.4 mm, respectively. After emptying the tanks (October 28 at 16:00), the load was kept null for 24 hours with a consequent recovery of displacements. A maximum rebound of 50%, 40%, 60%, –7%, 67% of the maximum settlement was measured for C0, C10, M10, C40, and E10, respectively. At the beginning of the second loading phase (October 29 at 15:49) the load was increased to 11.3 kPa (all the 8 tanks are filled) and maintained constant for 72 hours. The settlements induced by the second load summed to the residual displacements after the recovery period reaching a maximum settlement on the marsh surface (C0) of 32 mm. C10, M10, E10 and C40 record a settlement up to 18, 15, 1 and 2 mm, respectively. At the end, the tanks were emptied and the rebound was monitored for about 24 hours. The sensors accumulated a permanent displacement of about 22, 13, 10 2 and 2 for C0, C10, M10, C40 and E10, respectively, which correspond to a rebound of 30-40% for sensors C0, C10 M10 and E10 and around 20% for C40, of the maximum displacement.

It is useful to consider differences between displacements measures at different depths to understand the degree of compaction of the different soil layers (Fig. 3.4):

- The difference C0-C10 defines the compaction of the shallowest soil layer (0 - 10 cm);
- The difference between C10 and C50 represents the compaction of the intermediate layer from 10 to 50 cm;
- The sensor C50 gives us indication of soil compaction in the deeper layers.

Compaction of the deep soil layers was basically negligible when compared to the shallow ones. The shallowest layer (C0-C10) compacted of 6 mm during the first loading phase and of about 13 mm in the second. For the intermediate layer the trend was quite different. The observed compaction was lower (3 mm) than the one occurred in the shallowest layer of soil while loss of elevation for the intermediate layer was higher (16 mm) than the first layer during the second loading phase. Similar patterns can be observed also during the rebounds. The recovery of the shallowest layer was equal to 2.5 and 5 mm after the first and the second loading phase, respectively, while the measured rebound for the

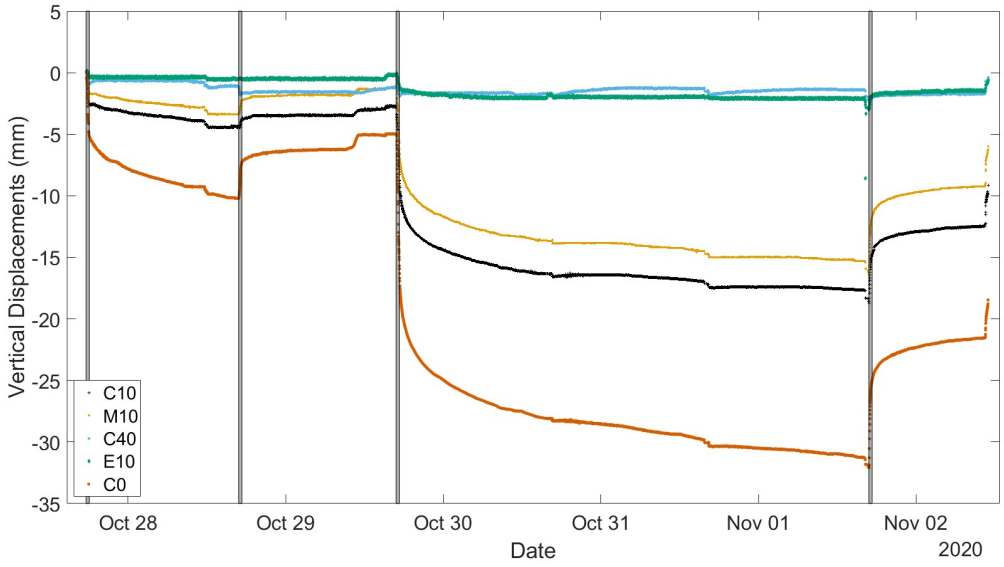

(a) Measured displacements during La Grisa experiment

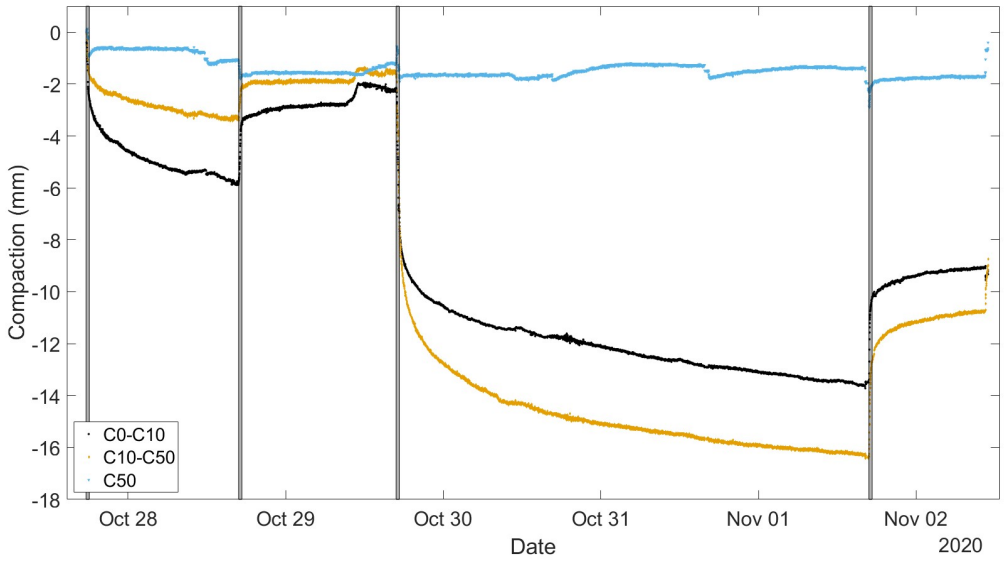

(b) Compaction of the different soil layers in the center of the loading area

Figure 3.4: Vertical displacement and compaction registered by each sensor versus time measured during loading and unloading phases at the La Grisa in-situ test.

intermediate were about 1 and 6 mm. From these measurements, It is plausible that:

- Since displacements recorded by C40 were much smaller than the others, stiffness of deeper soils was much higher than shallow layers.
- Compaction of the shallow and intermediate layer were comparable even if the thickness of the intermediate layer (C10-C40) is three times larger. This means that compressiblity of the shallowest layer was plausibly larger than the one of the

intermediate layer.

The plots in Fig. 3.4b show evident creep deformations following the load application after the overpressure dissipation.

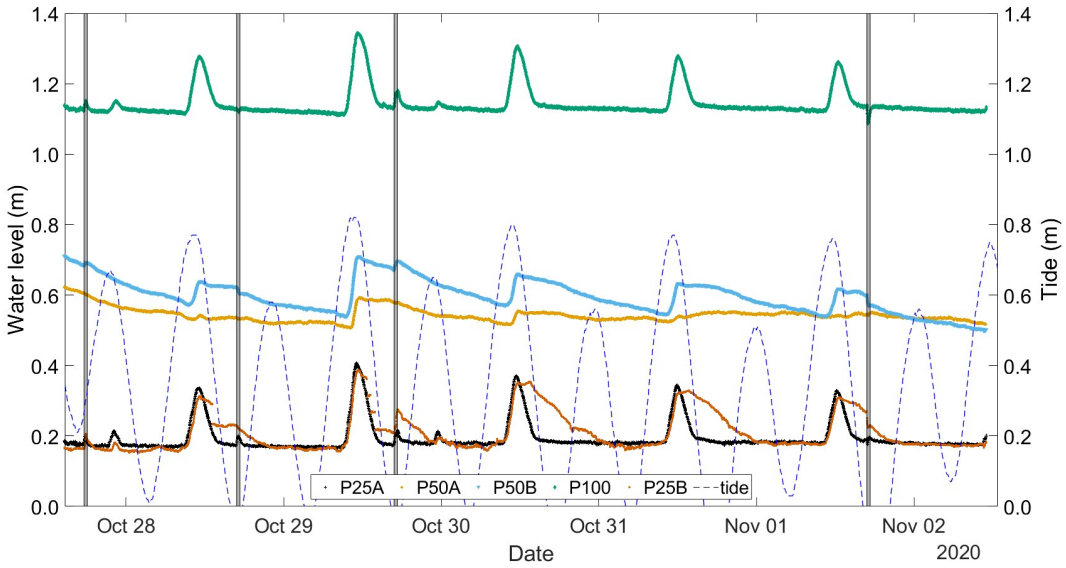

Figure 3.5: Pore-water pressure (left axis) and tidal water level (right axis) measured during the loading and unloading phases at various depths during the La Grisa in-situ experiment. P25, P50, and P100 refer to deployment depth equal to 0.25, 0.5 and 1.0 m below the marsh surface. Letters A and B identify sensors located on the two sides of the experiment.

Pore-water pressure evolution during the experiment is depicted in Fig. 3.5 together with tidal level fluctuations. The water level followed the tidal oscillations when the marsh platform was submerged. The dissipation of the (under)overpressures produced by the (un)loading followed the tidal evolution in P20A and P100, but it lagged significantly in P20B, P50A, and P50B. From the plots it is possible to highlight the different pressure behavior even for pressure transducers deployed at the same depth. The highly heterogeneous lithology distribution along the vertical direction and in horizontal direction was likely responsible of these particular behaviors of pore-water pressure evolution.

3.4.2 Campalto experiment

The in-situ loading experiment was carried out in Campalto marshland between 13/07/2021 and 17/07/2021. The experiment consists of two loading-unloading cycles:

- The first loading cycle started at 14:47 of July 13. A load of 5.6 kPa (first line of

tanks was filled) has been imposed to the marsh in around 15 minutes and it lasted for about 22 hours. Then, the soil was completely unloaded.

- The second loading cycle started at 12:40 of July 15. The load of 11.3 kPa (all the tanks are filled with water) was imposed in around 30 minutes and maintained for 54 hours before the final unloading.

Fig. 3.6 represents the loading steps imposed during the experiment.

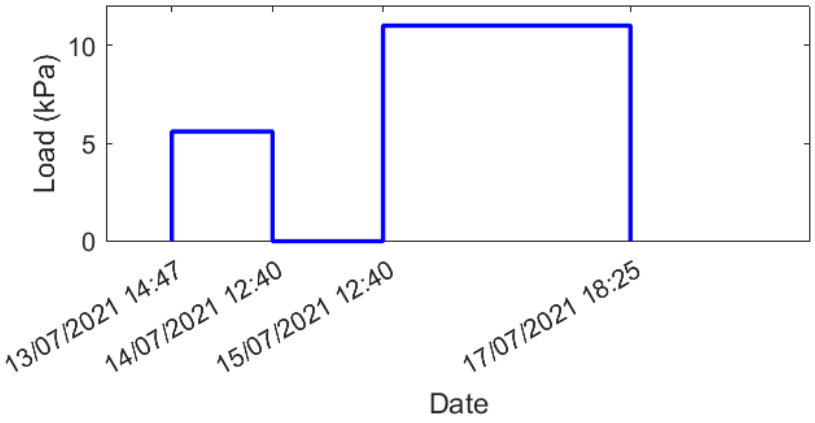

Figure 3.6: Load applied on the marsh surface following the various loading and unloading phases with the filling and emptying of the tanks.

The in-situ apparatus was equipped with five dial indicators (C0, C10, M10, E10, C50) located at 0 cm, 10 cm and 50 cm, from the marsh surface and six pressure loggers (P20A, P20B, P50A, P50B, P100A, P100B) positioned at three different depths, i.e. 20 cm, 50 cm and 100 cm (Fig. 3.7).

The data collected by the five displacement transducers, represented in Fig. 3.8a, show that the marsh compaction varies significantly as a function of depth and position with respect to the center. The black vertical lines represent the start of (un)loading phases.

During the loading application the soil was compressed, experimenting the primary consolidation process which is characterized by the dissipation of pore-water overpressure which consequently leaded to vertical displacements. After the excess of pore-water

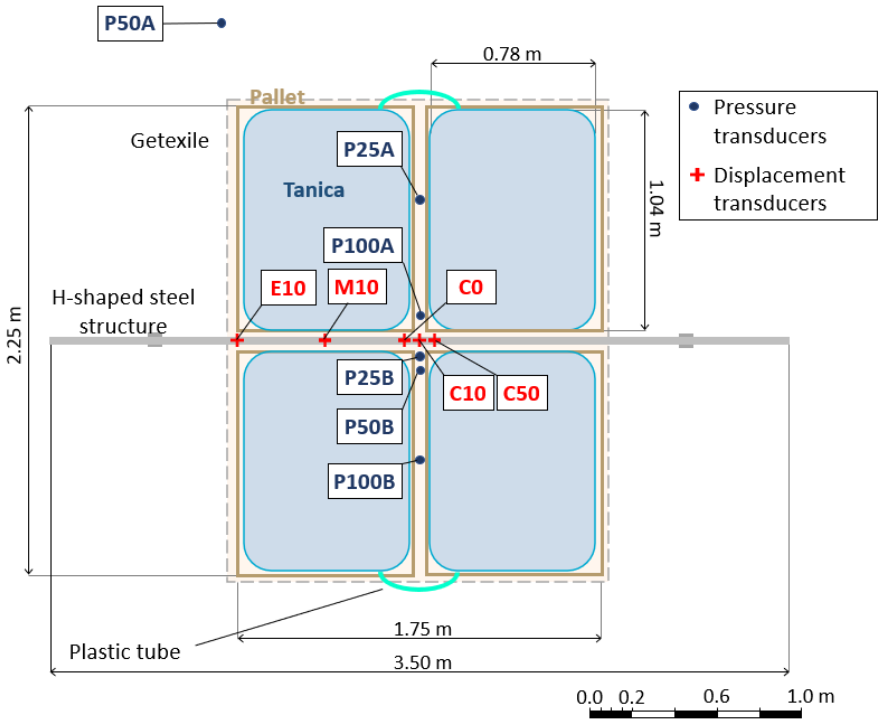

Figure 3.7: Plan view with dimensions, equipment (tanks, pallet, reference steel structure), location of the sensors to measure vertical displacements (red crosses) and pore-water pressure (blue dots). The sensor coding is representative of the deployment depth (in cm).

pressure was dissipated, the secondary consolidation occured. In this phase, the settlement was due to viscous deformations occurring at constant loading conditions. In the second phase, it is possible to notice that even if the load remained constant, the displacements slowly increased (Fig. 3.8a). Those settlements were due to the secondary consolidation process.

At the end of the first loading cycle, the maximum settlement of the land surface (sensor C0) equals 1.9 mm which was very similar to settlements recorded by sensors C50 and C10 (1.7 mm and 1.6 mm, respectively). The maximum displacements was recorded by sensor M10 (2.8 mm) and the minimum by the sensor E10 (0.6 mm) located at the edge of the loading area. After the first unloading, only part of the deformations was recovered. The maximum measured rebounds for sensors C0, C10, M10, E10 and C50 were equal to 40%, 44%, 66%, 74%, 13% of the maximum settlement. At the end of the second loading cycle (11.3 kPa), C0 collected a final settlement of 16 mm while M10, C10, E10, C50 reached a maximum displacement of 11.5 mm, 9.5 mm, 3 mm and 4 mm, respectively. Finally, the soil was unloaded and at the end of the experiment (after 24 hours), the sensors

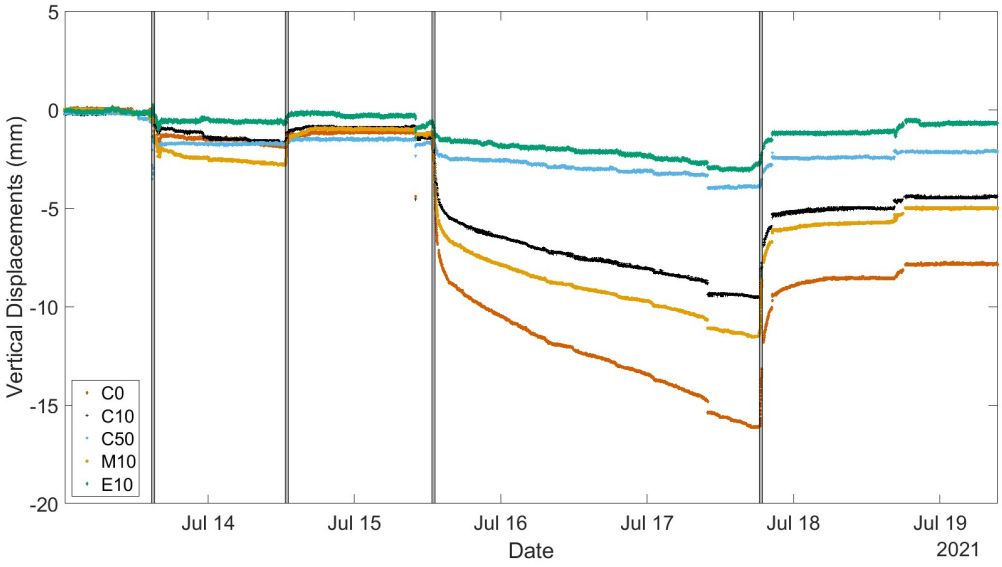

(a) Vertical displacement registered by each sensor versus time measured during loading and unloading phases at Campalto. C0, C10 and C50 are located directly below the load center and refer to the marsh surface, and 0.1 and 0.5 m (0.5 m) depth. E10 and M10 refer to a 0.1 m depth at the edge of the loaded area and in an intermediate position, respectively.

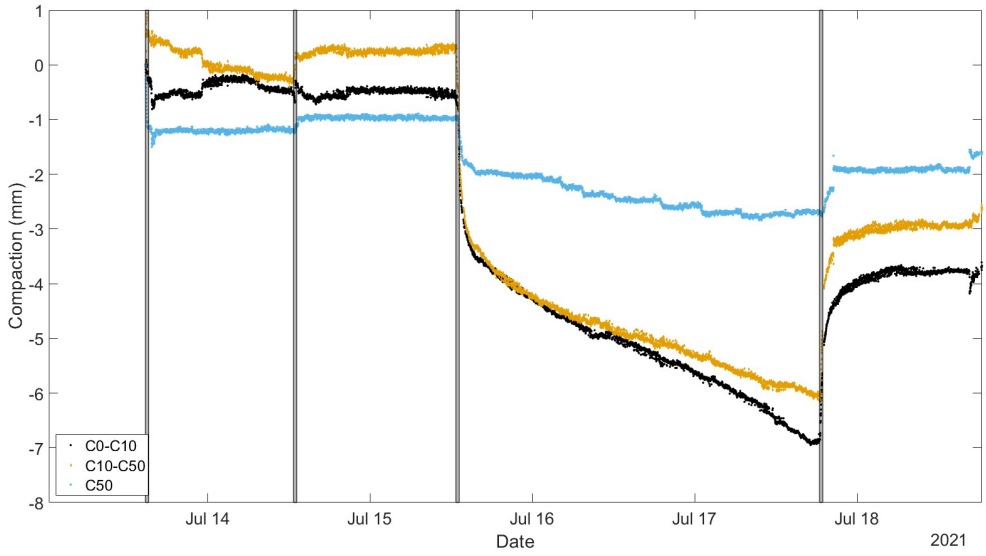

(b) Compaction of the different soil layers in the center of the loading area.

Figure 3.8: Vertical displacement and compaction registered by each sensor versus time measured during loading and unloading phases at the Campalto in-situ test.

accumulated a permanent displacement of about 8.6 mm, 5.7 mm, 5 mm, 1.2 mm and 2.5 mm for sensors C0, M10, C10, E10, C50, respectively, that correspond to a maximum rebound of $46\%, 50\%, 47\%, 60\%, 40\%$ of the maximum settlement. The displacements due to secondary consolidation were significant in the second loading cycle expecially for sensors C0, C10 and M10.

It is useful to express the results also in terms of compaction of the different soil layers. In Fig. 3.8b the difference between displacements measured by sensors C0 and C10 (C0-C10) provides the vertical compaction of the shallowest soil layer with thickness 0.1 m. Compaction C10-C50 expresses the compaction of the intermediate layer (thickness 0.4 m) and C50 describes the response of the deepest layers. The compaction of the deepest soil layer was much lower than the others ones because the soil was less affected by the load and its compressibility was higher than the superficial layers. As concern the shallowest layer (C0-C10), the compaction during the first cycle of loading-unloading was very limited (below 1 mm) while it reached 7 mm by the end of the second loading phase. The rebound equaled 3.5 mm corresponding to about 50% of the maximum compaction. The compaction of the intermediate layer was positive during the whole first cycle, meaning that vertical displacements measured on the soil surface were lower then the ones measured at 0.1 m below the ground level, which is a non sense from a theoretical point of view and it may be related to errors during the experiment measurements. Compaction and rebound of the intermediate layer (C10-C50) induced by the second loading-unloading cycle were about the same of the first layer even if its thickness was four times higher than the latter. This was due to the fact that compressibility of this salt marsh decreases with depth. Effect of creep deformations decreased with depth (C0-C10 compaction curve is steeper than C10-C50 and C50 curves).

The pore-water pressure observed during the Campalto experiment depicted in Fig. 3.9 together with the tidal water level which was measured by a tidal gauge specifically established during the experiment. Note that the tidal gauge was not able to record water level below 0.4 m most likely because it was not submerged. Pressure transducers provided measure of pore-water pressure, expressed in kPa, with a temporal resolution of 1 minute which have been purified by atmospheric pressure and converted to meters of water column. The evolution of pore-pressure during the experiment reflected the load behavior. During the two loading phases there was the formation of an excess of pore-water pressure that was then immediately dissipated when the load remain constant. On the other hand, during the unloading phases there was the formation of an under-pressure which was then dissipated after few hours. The amount of (under)over-pressures was function of the load intensity, depth and position of the pressure logger. Tide played a foundamental role in pore-water pressure records. During high tide conditions, when the marshland

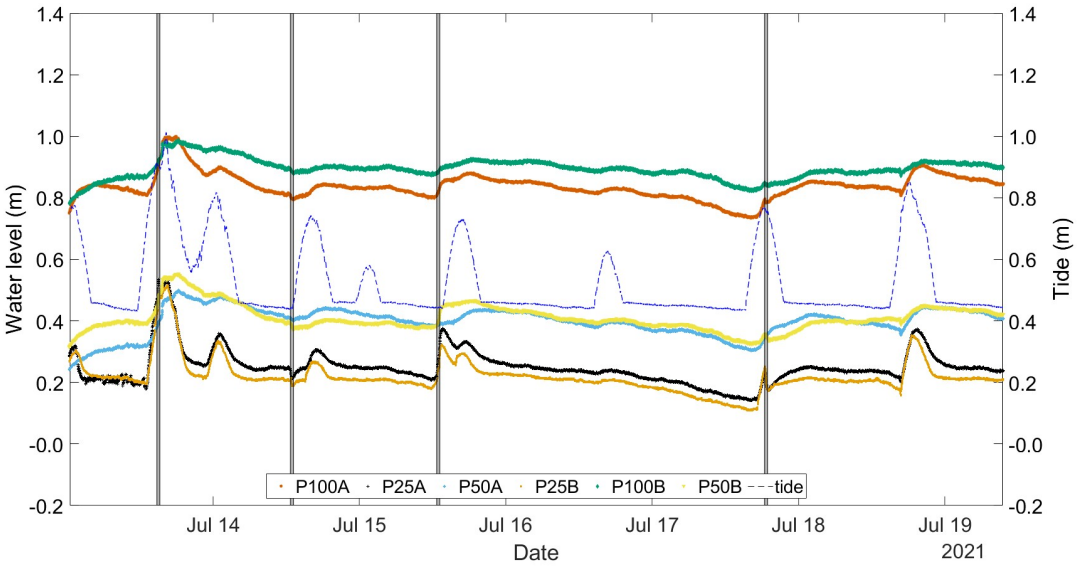

Figure 3.9: Pore-water pressure (left axis) and tidal water level (right axis) measured during the loading and unloading phases at various depths during the Campalto in-situ experiment. P25, P50, and P100 refer to deployment depth equal to 0.25, 0.5 and 1.0 m below the marsh surface. Letters A and B identify sensors located on the two sides of the experiment.

was submerged the pore-water pressure followed the tidal level. First loading and second unloading were carried out during high tide conditions. In this situation the effect of the tide was added to that of the load while during the second loading (12:40 of July 15) the measured overpressures were due exclusively to the imposed load. Overall, the perturbation caused by the (un)loading operations amounted to a few centimeters. The largest variability was observed for the shallower sensors (P25A, P25B) while perturbations decreased with depth. As expected, the deeper soil layers were less affected by the loading effect.

3.4.3 Le Saline experiment

The loading experiment was conducted at Le Saline (North of Venice Lagoon) marshland between 06/09/2022 and 10/09/2022. The experiment is composed by two loading-unloading cycles:

- In the first cycle, the loading started at 14:00 of September 6 and after 15 minutes the final target of 5.6 kPa was reached. Then the load was maintained constant for about 1 day and finally the soil was completely unloaded.

- The second loading cycle started at 10:45 of September 8. A load of 11.3 kPa imposed in 30 minutes was maintained constant for about 2 days before the final unloading.

In Fig. 3.10 the loading cycles are presented.

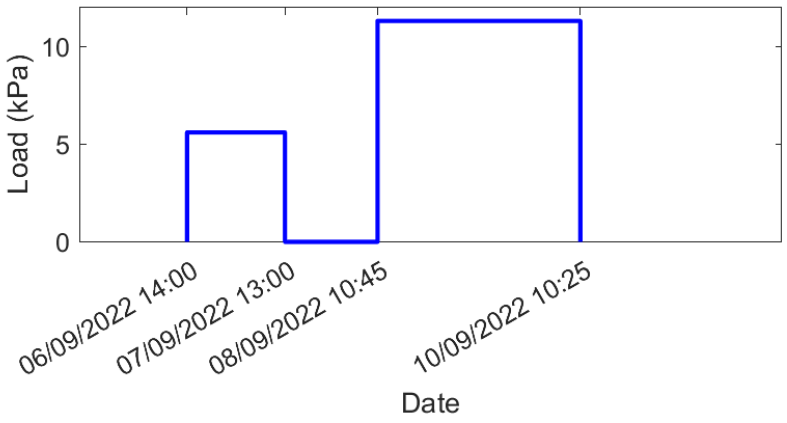

Figure 3.10: Load applied on the marsh surface following the various loading and unloading phases with the filling and emptying of the tanks.

The experiment was equipped with five displacement transducers (C0, C10, E10, M10, C50) and six pressure loggers (P25A, P25B, P50A, P50B, P100A, P100B) located at different depths and positions according to the plant of the experiment (Fig. 3.11).

The distribution of the sensors was basically the same of the one used during the Campalto experiment. C0, C10, C50 and P100A, P25B were located in the center of the loading area, P50B, P25A and M10 were placed in intermediate position, E10 and P100B were situated on the edges of the load while P50A was far from the pallets.

The data collected from the five displacements transducers with time resolution of one minute are presented in Fig. 3.12a.

Displacements measured during the Le Saline experiment were larger than the ones measured in Campalto in both loading cycles proving that soil is more compressible. At the end of the first loading cycle, the maximum settlement measured on the marsh surface

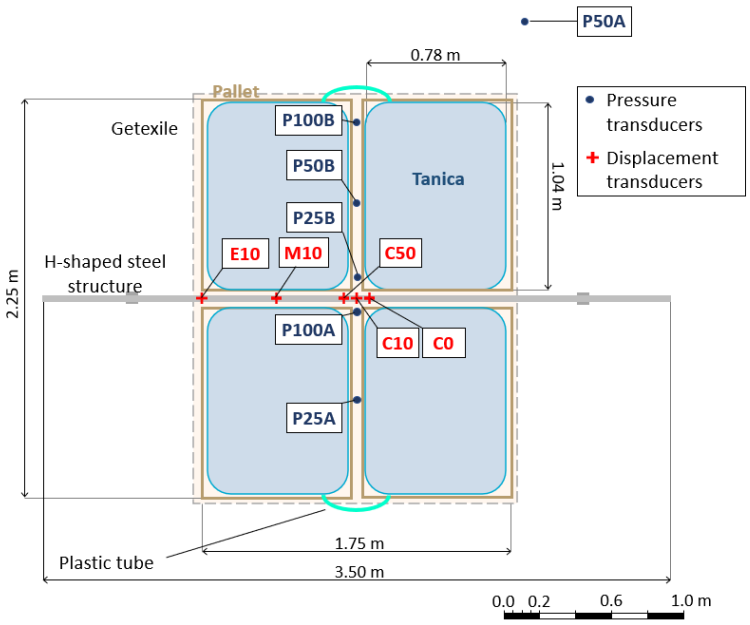

Figure 3.11: Plan view with dimensions, equipment (tanks, pallet, reference steel structure), location of the sensors to measure vertical displacements (red crosses) and pore-water pressure (blue dots). The sensor coding is representative of the deployment depth (in cm).

(sensor C0) was equal to 7.8 mm while sensors C10, M10, E10 and C50 recorded 4.1 mm, 3.2 mm, 1.4 mm and 2.8 mm, respectively. After the unloading was completed the soil recovered part of the deformations induced by the load. After one day of recovery the measured rebounds for the sensors C0, C10, M10, E10 and C50 were 40%, 35%, 35%, 45% and 25% of the maximum settlement. As regard the second loading phase of 11.3 kPa the maximum vertical settlements, reached at the end of the loading test, are 32 mm, 23.5 mm, 18.4 mm, 14.3 mm and 6 mm for sensors C0, C10, M10, C50 and E10, respectively. Then, the soil was completely unloaded and the maximum rebound, after around 1 day, was 8 mm for the most superficial sensor (C0), 5 mm for sensors C10, M10, only 1.5 mm for E10 and C50 and 8 mm for the most superficial sensor (C0) which correspond to 30% 25%, 30%, 30%, and 15% of the maximum settlement.

Comparing the displacements trends (in terms of maximum displacements and rebounds) of Le Saline with the ones observed in Campalto it is possible to deduce that Le Saline saltmarsh is more compressible (observed displacements are higher) and more plastic (rebounds were lower) than Campalto.

The vertical settlements were characterized by evident creep deformation (secondary consolidation). The displacements curves are characterized by a smooth transient behaviour

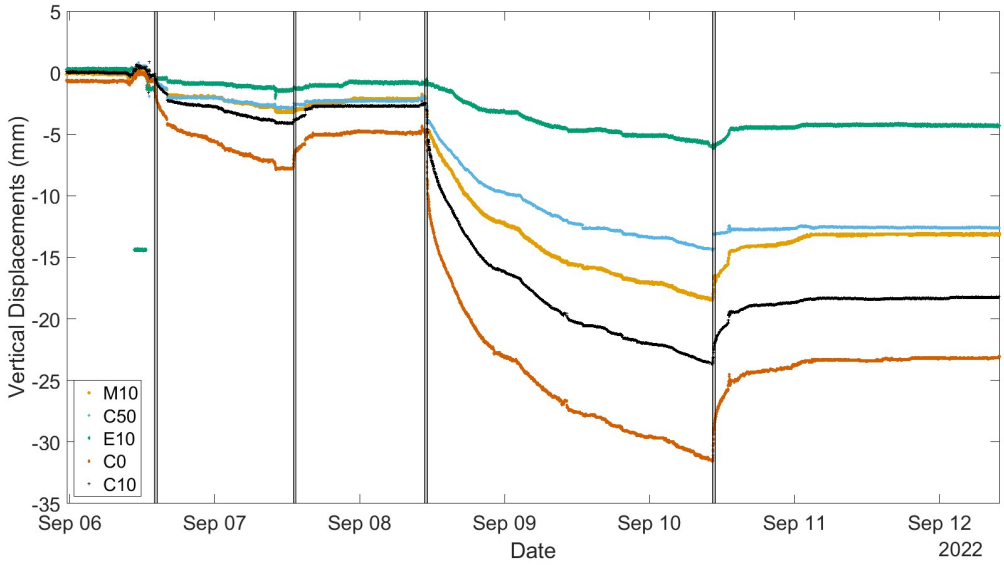

(a) Measured displacements during Le Saline experiment.

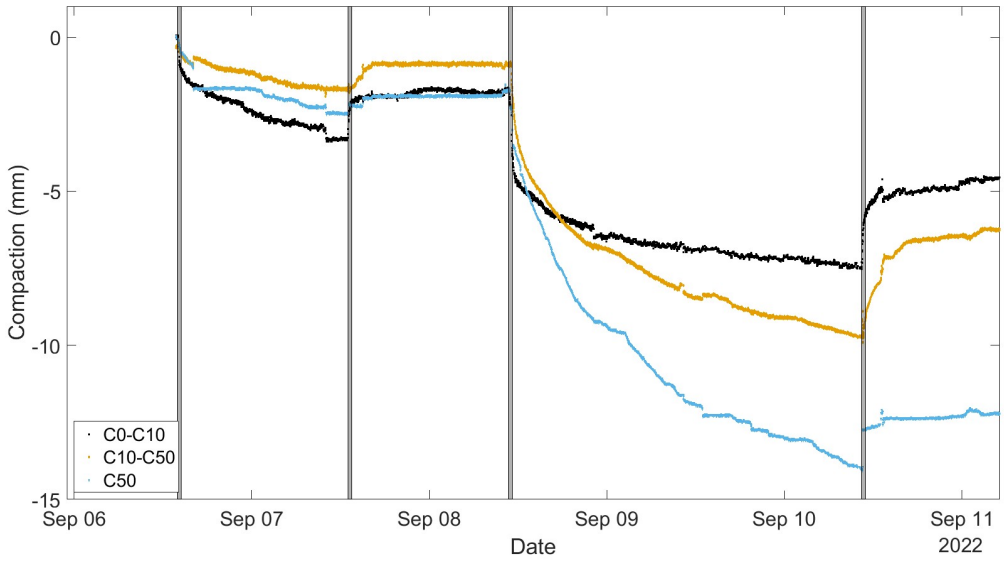

(b) Compaction of the different soil layers in the center of the loading area.

Figure 3.12: Vertical displacement and compaction registered by each sensor versus time measured during loading and unloading phases during the Le Saline in-situ test.

typical of secondary consolidation settlements. However, there was no evident transition from primary to secondary consolidation as in the case of Campalto where a rapid increase of displacements in correspondence of load application, followed by a plateau in which displacements increased very slowly, was observed.

It is useful to express the results also in terms of compaction of the different soil layers. In Fig. 3.12b the difference between displacements measured by sensors C0 and C10

(C0-C10) provides the vertical compaction of the shallowest soil layer with thickness 0.1 m. Compaction C10-C50 expresses the compaction of the intermediate layer (thickness 0.4 m) and C50 describes the response of the deepest layers.

The results presented in Fig. 3.12b highlighted that compaction of the different soil layers was very different proving that soil heterogeneity played and important role. The shallowest layer (C0-C10) compacted by 4 mm by the end of the first loading cycle and then it recovered about half of the total deformation At the end of the second loading phase the compaction was equal to 8 mm with a final rebound of 3 mm. The intermediate layer (C10-C50) displayed a completely different behavior when subjected to the two loading cycles. The compaction at the end of the first loading phase was very low (1.3 mm) and it was almost completely recovered after the soil was unloaded denoting that this soil layer displayed an elastic behavior. At the end of the second loading phase the layer compacted by 9 mm with a final recovery of 3.4 mm (40% of the total compaction). Considering that the compaction of the first two layers during the second loading cycles were similar and considering that intermediate layer was four times thicker that the shallowest one we can conclude that, plausibly, the upper layer was more compressible. As regard the deep layer (C50) in first cycle the compaction amounted to 3 mm with almost zero recovery (almost perfectly plastic behavior) after the unloading while in second cycle the measured compaction reached 14 mm by the end of the loading phase followed by a small rebound of 1.5 mm. From the plots in Fig. 3.12b, it is evident that the importance of creep deformations increased with depth. Compaction C0-C10 is interpretable with a visco-elasto-plastic model while the other two layers had more difficult behavior to interpret.

The six pressure transducers collected pore-water pressure measurement during the experiment with a sampling frequency of one minute. Pressure data expressed as meter of water column are plotted together with tide in Fig. 3.13.

Pressure evolution during the test was strongly affected by the tide. The peaks of pore-water pressure observed when the load was constant were caused exclusively by tidal oscillations. The magnitude of those peaks amounted on average to 0.2 m for all the pressure transducers. In correspondence the loading-unloading operations measured pressure was given by two contributions: (under)overpressure induced by the (un)loading

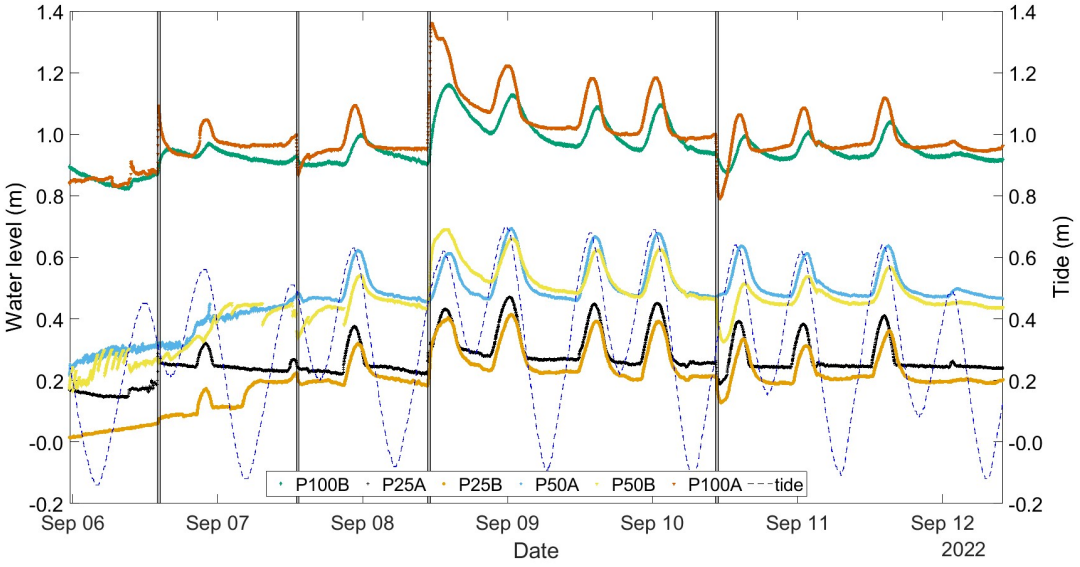

Figure 3.13: Pore-water pressure (left axis) and tidal water level (right axis) measured during the loading and unloading phases at various depths during the Le Saline in-situ experiment. P25, P50, and P100 refer to deployment depth equal to 0.25, 0.5 and 1.0 m below the marsh surface. Letters A and B identify sensors located on the two sides of the experiment.

and the effect of the tidal oscillations. Tidal effect become relevant if loading or unloading operations are carried out during high tide conditions. In such condition the symmetric tidal pressure curve becomes asymmetric due to the effect of the load as we can notice in Fig. 3.13 during the second loading.

As expected, the highest pore-water pressure variations were observed during the second loading cycle, just at the end of the operations of pumping and unloading, expecially for pressure transducer P100A which recorded an overpressure of 0.4 m and an underpressure of 0.2 m. As concern the sensor P50A which was located outside from the loading area, the measured pore-water pressure was not affected at all by the effect of the load and its oscillations were due only to the tide. It was also possible to notice that measures of pressure collected on the side "B" of the loading area were characterized by some lag if compared to the ones on the side "A" (see pressure transducers P100A and P100B).

3.4.4 Discussion on the results of the in-situ experiments

The records from the in-situ loading experiments provide new insights that progress our understanding of the hydro-geomechanical behavior of coastal marshes. The results of the

	First loading phase					
	C0-C10		C10-C50		C50	
Site	Compac.	Rebound	Compac	Rebound	Compac	Rebound
La Grisa	6.0	40	3.0	30	2.0	0
Campalto	0.5	0	0.0	0	1.0	20
Le Saline	4.0	50	1.3	70	3.0	20

Table 3.1: The Table presents the compaction, expressed in mm, for the three soil soil layers (shallow, intermediate and deep) and the rebounds, expressed as percentage (%) of the maximum compaction, in the first loading phase for the three experiments.

	Second loading phase					
	C0-C10		C10-C50		C50	
Site	Compac.	Rebound	Compac.	Rebound	Compac.	Rebound
La Grisa	13.0	40	16.0	40	2.0	0
Campalto	7.0	50	6.0	50	2.5	50
Le Saline	8.0	40	9.0	40	14.0	10

Table 3.2: The Table presents the maximum compaction (compac.), expressed in mm, for the three soil soil layers (shallow, intermediate and deep) and the rebounds, expressed as percentage (%) of the maximum compaction, in the second loading phase for the three experiments.

three in-situ experiments in terms of maximum compaction and rebounds are summarized in Tables 3.1 and 3.2, for the first and the second loading phase.

The results demonstrate that, within the same coastal system, compaction can spatially be highly variable and largely depends on the characteristics of the soil that composes the marsh landform, i.e. on the specific depositional environments where a marsh grows and thickens. Campalto site was characterized by the lowest deformations in both loading phases and by the highest rebounds at least for the second loading phase (Tab. 3.2), thus suggesting suggesting that here the soil has already experienced a larger preconsolidation. In the shallow (C0-C10) and intermediate layers (C10-C50), La Grisa was the site showing the highest degree of compaction in both loading phases followed by Le Saline and Campalto. At Le Saline, the compaction of the deeper soil layers was much larger that the other two sites, plausibly due to recent formation of this salt marsh. The rebounds at the end of the first loading cycles varied according to the site and the considered soil layer. In

the second loading phase rebounds amounted to $\sim$ 40-50% for shallow and intermediate layer.

The cross-comparison of results from laboratory tests, presented in Subsections 2.2.2 2.2.1 and the loading experiments in the field allows to evaluate the pros and cons of the in-situ testing approach. Unfortunately, no laboratory tests were conducted for Le Saline in-situ test. We can compare two loading stages, i.e. four and eight tanks filled by seawater respectively amounting to $\sim$ 5.6 kPa and $\sim$ 11.3 kPa, and two depth intervals, between the marsh surface and 0.1 m and from 0.1 to 0.5 m (0.4 m at La Grisa) depth using records provided by sensors C0, C10, and C50 (C40 at La Grisa). At La Grisa field deformations of the top 0.1-m interval were 5.5% and 13% for the half and full load, respectively. The values decreased respectively to 0.9% and 5.3% in the deeper interval (0.1-0.4 m) . Oedometric lab tests provide 7.9% and 12% at 0.16 m, 0.8% and 1.8% at 0.65 m, 0.3% and 0.4% at 0.8 m depth for 5.6 and 11.3 kPa, respectively. At Campalto field, for the top 0.1-m interval deformations were 0.5% and 7% and for the half and full load, respectively. Deformations in the deeper interval (0.1-0.5 m) , amounted to 0% and 1.5% for 5.6 and 11.3 kPa, respectively. Oedometric lab tests provide 3.4% and 8.2% at 0.05 m, 1.0% and 2.1% at 0.25 m, 0.7% and 1.2% at 0.5 m depth for 5.6 and 11.3 kPa, respectively. The general consistency between field and lab quantifications demonstrates that the loading test design ensures the validity of the oedometric assumption, i.e. vertical deformation with precluded lateral expansion.

A second interesting outcome is related to marsh behavior during the unloading phase when the water tanks were being emptied. Soil is more deformable during loading than during unloading, as only part of the deformation is reversible. The ratio s, introduced in the Subsection 2.2 represents the ratio compressibility during loading (i.e. partially irreversible deformation) and unloading (i.e. only reversible deformation). The results achieved at La Grisa and Campalto provide values of s $\sim$2 being the rebounds $\sim$ 40-50% (Tab. 3.1 3.2). Such a highly recoverable response of the shallowest marsh soil is unexpected, also compared with the Cc and Cr provided by the lab oedometric tests carried out on the samples collected in the two sites suggesting s $\sim$5-20, with a decreasing trend with depth.

(a) **(b)**

Figure 3.14: Shallow (a) and deep (b) portable tests.

3.5 The portable loading test

Since the loading test is demanding in terms of field work and logistics, a downscaled version version has been designed. This portable test has been conducted at Le Saline and La Grisa in the same area where the large-scale loading tests took place. The aim of the test is to study the response of marsh soils to loading-unloading conditions in terms of vertical displacements. The experimental setup (Fig. 3.14) consists of a steel cylinder with a diameter of 32 cm and a height of 30 cm embedded into the ground. A porous glass is placed above the cylinder to allow the water drainage. On top of the glass the load is induce by three weights of 20 kg each (10.7 kPa). This load is very close to the load imposed during the second loading cycle of the large-scale tests. The load is imposed instantaneously by placing the 3 weights and it is maintained for about 45 minutes, then the load is removed. The monitoring of the unloading phase lasts about 10 minutes. A digital sensor, fixed on steel bars connected to the steel cylinder, record vertical displacements during both the loading and the unloading phases. The tests were conducted in different sites and at two different depths, i.e. on the marsh surface and at a depth of 20 cm below the surface.

At Le Saline, six downscaled loading tests were conducted from 05/09/2022 to 10/09/2022,

Figure 3.15: Locations of the loading tests conducted at Le Saline. Downscaled tests are encoded using the P capital letter that stands for Portable, SAL stands for Le Saline and they are numbered from 1 to 6. “LS-SAL” identify the large-scale test position.

during the large-scale test, in different locations as it is shown in the map of Fig. 3.15.

The records of vertical displacements are presented in Fig. 3.16. The letters "D" and "S" stand for deep and shallow tests, respectively. Notice that in the first two tests (P1-SAL, P2-SAL) the applied load was one-third lower than the others (two disks were used instead of three) and it was conducted only at the marsh surface.

All the plots display a similar behavior which is characterized by rapid shifts in displacements in correspondence of load application or removal followed by plateaus where settlements remain more or less steady since the load remains constant. As expected, the vertical movement of ground level (S-shallow) was grater than displacements measured at a depth of 20 cm (D-deep). Excluding the test P5-SAL which was conducted on the "ghebo" (minor channel crossing the salt marshes of the Venice Lagoon), displacements measured at marsh surface ranged from 8 mm to 12 mm while for the deep tests vertical settlements varied from 6 mm to 11 mm. As regard test P5-SAL the measured displacements at surface were twice those of the other trials. We can conclude that soil on the small channels was much more compressible than the marshland platform which was covered

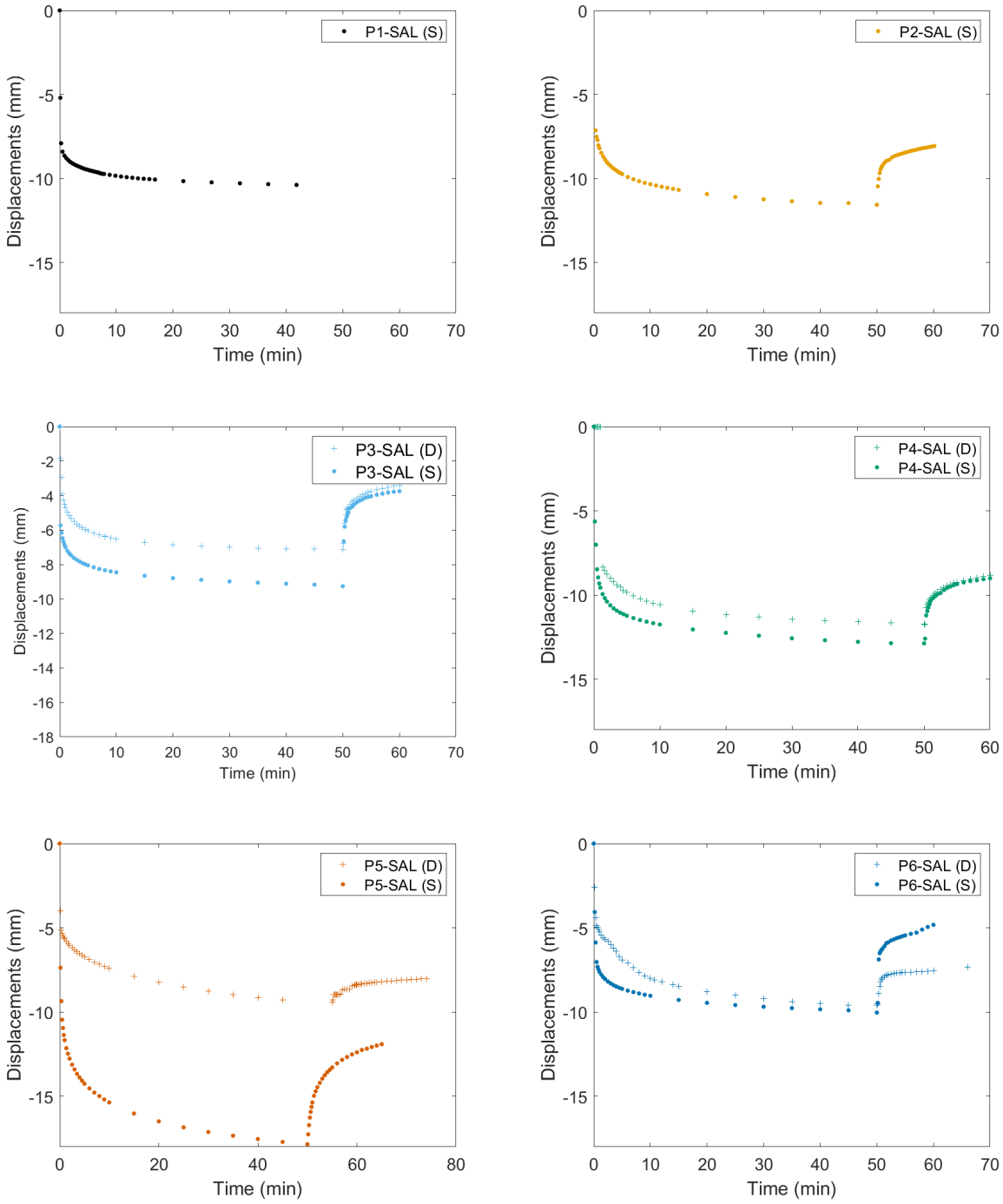

Figure 3.16: Displacements measured in time during the downscaled loading tests performed in six different sites of Le Saline salt-marsh. Downscaled tests are encoded using the P capital letter that stands for Portable, SAL stands for Le Saline. They are numbered from 1 to 6. The letters "D" and "S" stand for deep and shallow test, respectively.

by vegetation. Such difference in displacements can be attributable to plant roots that significantly increased the soil stiffness [17]. The effect of roots on stiffness was supported by the fact that displacements P5-SAL5 (D), measured at 20 cm below soil surface where

roots were no more present or, at least, their distribution was less dense, were similar to the ones of the other tests. The compaction of the uppermost 20 cm amounted, on average, for shallow tests, to 10 mm, meaning a deformation $\epsilon = \frac{dH}{H} = 0.05 = 5\%$ where H is the thickness of the soil layer. A rough estimate of the oedometric modulus M_{ed} which is the inverse of soil compressibility can be provided as: $M_{ed} = \frac{1}{C_m} = \frac{\Delta\sigma_{ef}}{\Delta\epsilon} = \frac{0.0107}{0.05} = 0.214$ MPa.

In all the experiments, the rebound at marsh surface (S) was higher than the one measured at 20 cm (D) and it amounted to about 50% of the total settlements in tests P6-SAL (S) and P3-SAL (S). The rebound was equal to about one third of the total displacement for the other shallow tests and it was even lower for the deep ones.As regard the differences in settlements between tests conducted at same depth vegetation type and soil heterogeneity were the most important causes.

The measured displacements collected during the downscaled tests can be compared with the ones of the Le Saline large-scale test presented in Fig. 3.12a taking into account that the loading area, loading procedure and monitoring time were completely different. The imposed load equal to 10.7 kPa was close to 11.3 kPa which was the load maintained during the second loading phase during the large scale test. The loading areas for the large-scaled and the downscaled tests were respectively, 4 m^2 and 0.055 m^2. According the theory, loading area is strictly related to depth. As it is shown in Fig. 3.17, for a rectangular loading area of 1.75 m×2.1 m, the soil is influenced by the load up to a depth of about 3 m but its intensity decrease with depth. The soil perceives the effect of the total load only up to a depth of 0.6 m (0.8 q curve) in case of the large-scale loading test. For the downscaled tests this depth was even lower. Making a proportion and considering that the diameter of the disks is 0.275 m, in the portable test the soil is influenced by 80% of the load only for the first 0.1 m. Since the loading phase lasted only 50 minutes the viscous behavior could not be characterized in the downscaled tests while in large scale tests it constitutes relevant part of the total displacement. Concluding, because of the factors explained above, the maximum vertical displacements recorded during the downscaled test were significantly lower than the ones of the large-scale test. Considering only the first 45 minutes of the second cycle of the large-scale test, after the load application (complete filling of the tanks) sensors recorded surface settlement was about 8 mm which was consistent with what we observed in the downscaled tests.

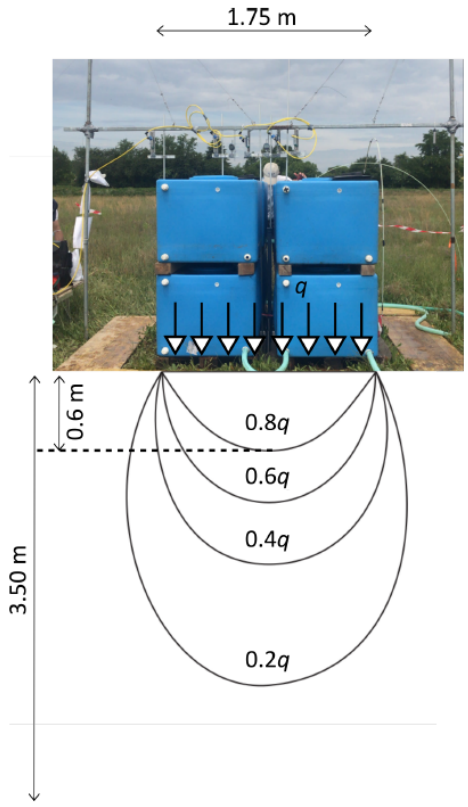

Figure 3.17: Load propagation with depth (after [12]).

At La Grisa, the downscaled tests were conducted on March 30, 2023 in two different locations of the marshland (Fig. 3.18). For each test, both surface (S) and deep (D) vertical displacements have been investigated. The experimental setup was the same used in Le Saline. Rebound was monitored for longer time than Le Saline to allow for the completion of the recovery process.

The first test (P1-LG) took place close to the large-scale experiment conducted at La Grisa in October 2020 while the second one (P2-LG) was conducted near the embankment that separates the marshland from the countryside. The results of the two tests are presented in Fig. 3.19.

In the test P1-LG (Fig. 3.19a) maximum recorded displacements were 16 mm and 10 mm for the shallow (S) and the deep (D) test, respectively. Records of the test P2-LG were in disagreement with what has been observed previously in Le Saline and in the first La Grisa experiment. In this case (Fig. 3.19b) the maximum vertical displacements measured on the marshland surface (10 mm) were lower than the ones at 20 cm below the ground level (14 mm). This behavior suggests that the superficial soil layer (between 0 and 20 cm)

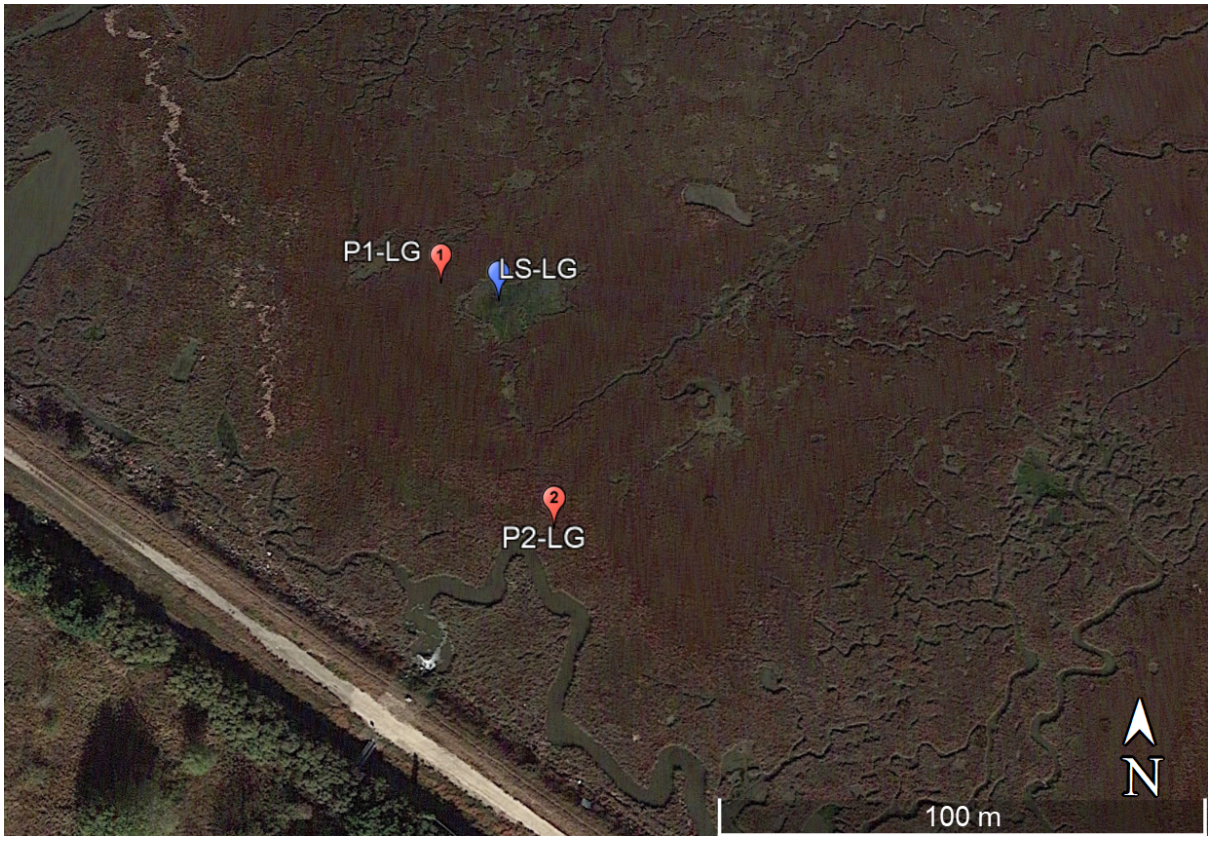

Figure 3.18: Locations of the downscaled tests at La Grisa site. Downscaled tests are encoded using the P capital letter that stands for Portable, LG stands for La Grisa and they are numbered from 1 to 2. 'LS-LG' identify the large-scale test position.

is stiffer than the deep layers due to plant roots or an higher inorganic fraction.

The compaction of the uppermost 20 cm amounted for the shallow downscaled test (P1-LG (S)) to 15 mm thus corresponding to a deformation $\epsilon = 7.5\%$ which was larger respect to what we observed at Le Saline. The estimated oedometric modulus amounted to $M_{ed} = \frac{1}{C_m} = \frac{\Delta\sigma_{ef}}{\Delta\epsilon} = 0.143$ MPa which was coherent with the results obtained from the laboratory oedometric test on soil samples presented in Section 2.2.1 for similar values of effective stress. From the comparison of the two oedometric modules computed it is possible to conclude that La Grisa salt-marsh was more compressible than Le Saline, at least for the investigated soil layer.

The rebounds were coherent with what observed in Le Saline. The marsh recovered more displacements at marsh surface with a rebound equal to about 50% of the maximum settlement. The rebounds measured at a depth of 20 cm are equal to 30% and 40% of the maximum settlement respectively for tests P1-LG and P2-LG.

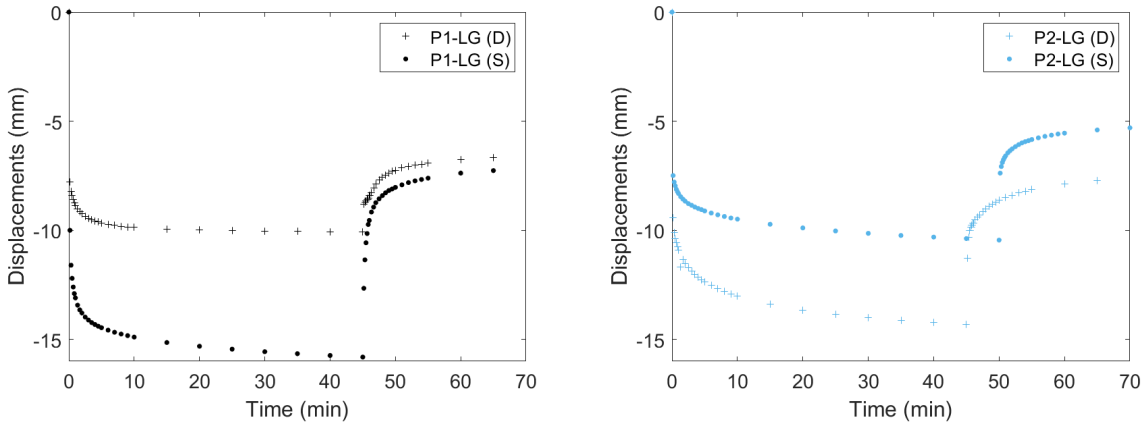

(a) **(b)**

Figure 3.19: Vertical displacements recorded at marsh surface (S) and at 20 cm depth (D) during La Grisa downscaling testing. Downscaled tests are encoded using the P capital letter that stands for Portable, LG stands for La Grisa. The letters "D" and "S" stand for deep and shallow test, respectively.

Results of test P1-LG (collected in the same area where large-scale test was conducted three years before Fig. 3.18) can be compared with the ones collected during the large-scale test. Considering only the first 45 minutes of the second cycle of the large-scale test, after the load application (complete filling of the tanks) sensors C0 and C10 reads 15 mm and 8 mm of settlement which are perfectly coherent with the measurements of the downscaled test. If we analyze the whole loading cycle of the large-scale test final deformations become much larger due to creep process, which can't be characterized in the downscaled tests due to the limited duration of the experiment and due to the limited loading area.

4 Numerical Model

4.1 Theory of poroelasticity

Soft soils such as sand and clay consist of small particles, and often the pore space between the particles is filled with water. In soil mechanics this is denoted as a saturated or partially saturated porous medium. The deformation of such porous media depends upon the stiffness of the porous material, and upon the behaviour of the fluid in the pores. The simultaneous deformation of the porous material and the flow of the pore fluid is the subject of the theory of consolidation, often denoted as poroelasticity [18].

The theory was developed originally by Terzaghi [19] for the one-dimensional case, and extended to three dimensions by Biot [20] [21]. In his original theory Terzaghi postulated that the deformations of a soil were mainly caused by a rearrangement of the system of the particles, and that the compression of the pore fluid and of the solid particles can practically be disregarded. In a saturated soil this means that a volume change of an element of soil can only occur by a net flow of the fluid with respect to the solid particles. This system of assumptions often is a good approximation of the real behaviour of soft soils, especially clay, and also soft sands. Such soils are highly compressible (deformations may be as large as several percents), whereas the constituents, particles and fluid, are very stiff. In later presentations of the theory, starting with those of Biot, compression of the pore fluid and compression of the particles has been taken into account. This generalization has made it possible to also consider the deformations of stiffer materials such as sandstone and other porous rocks, which are very important in the engineering of deep reservoirs of oil or gas [18].

In the case that the soil is completely saturated and it undergoes variations of the conditions representing external stressors, for instance groundwater extraction or an increasing load on the surface, the solid skeleton will be deformed and, as a consequence, the pore fluid will flow through the matrix. Such behaviour implies the variation of the stress state. Part of the geostetic load (i.e. the weight of the saturated medium) is supported by the hydrostatic pressure of the water in the pores and another part by the so-called effective stress, i.e. the stress exchanged by the grains at the contact points.

Therefore, the soil load is sustained both by the water and by the solid particles. For this reason, to describe properly this phenomenon, the set of equations needed is made up on one hand by a flow model, describing the interstitial fluid movement, and on the other hand by a structural one (geomechanical model), regarding, instead, the soil equilibrium. Those two sets of equations are coupled, forming a system of equations [18].

4.1.1 Flow model

The water movement in a porous medium is controlled by Darcy's law [22] according to which the water flux is proportional to the hydraulic gradient through a constant called hydraulic conductivity:

$$\boldsymbol{q} = \boldsymbol{k}\nabla h \tag{4.1}$$

Where:

- $\boldsymbol{k}$ is the hydraulic conductivity tensor
- ∇h is the gradient of the hydraulic head with $h = \int_{z}^{z_0} dz + \int_{p}^{p_0} \frac{dp}{\gamma}$ where p is pore-water pressure and z is vertical coordinate.
- ∇ is the differential operator: $\frac{\partial}{\partial x} + \frac{\partial}{\partial y} + \frac{\partial}{\partial z}$.

Assuming the soil is fully saturated (all the pores are filled with water) Darcy's velocity can be rewritten as:

$$\boldsymbol{v} = n(\boldsymbol{v}_w - \boldsymbol{v}_s) \tag{4.2}$$

If the soil is completely saturated only two phases are present and assuming that solid grains are uncompressible and water has compressibility β the state equations for the solid and the liquid phase respectively are:

$$\gamma_s = const \tag{4.3}$$

$$\gamma_w = \gamma_{w0} e^{\beta}(p - p_0) \tag{4.4}$$

One of the major principles of the theory of consolidation is that the mass of the two components, water and solid particles, must be conserved. The equations of mass conservation of the solids and the fluid can be established by considering the flow into

and out of an elementary volume fixed in space. Mass conservation equation is called also continuity equations and reads for the solid and the fluid respectively:

$$-\nabla[(1-n)\gamma_s \boldsymbol{v}_s] = \frac{\partial[(1-n)\gamma_s]}{\partial t} \tag{4.5}$$

$$-\nabla(n\gamma_w \boldsymbol{v}_w) = \frac{\partial(n\gamma_w)}{\partial t} \tag{4.6}$$

Manipulating them, using Darcy's law to express the velocity of the fluid with the assumption of $\boldsymbol{v_s} = 0$, the state equation for the fluid, the flow model is obtained:

$$\nabla[\boldsymbol{k}(\nabla z + \frac{\nabla p}{\gamma})] = n\beta\frac{\partial p}{\partial t} + \frac{\partial \epsilon}{\partial t} \tag{4.7}$$

Where ϵ is the volumetric deformation of the porous medium:

$$\epsilon = \epsilon_x + \epsilon_y + \epsilon_z = \frac{\partial u}{\partial x} + \frac{\partial v}{\partial y} + \frac{\partial w}{\partial z} = \nabla \boldsymbol{u}$$

Equation 4.7 represent the flow equation which is not enough to fully describe the consolidation process because soil deformations are unknown. The system has 4 unknowns: the soil displacements along the 3 main directions u, v, w and pore-water pressure p. It's necessary to introduce a new set of equations able to express deformations in function of pore-water pressure change through the equilibrium equations.

4.1.2 Geomechanical model

Geomechanical model is based on the equilibrium equations which are obtained by considering the stresses acting on the six faces of a cubic elementary volume. The equilibrium equations along the 3 coordinate directions are:

$$\begin{aligned}
\frac{\partial \sigma_{tot,xx}}{\partial x} + \frac{\partial \tau_{tot,xy}}{\partial y} + \frac{\partial \tau_{tot,xz}}{\partial z} &= 0 \\
\frac{\partial \tau_{tot,yx}}{\partial x} + \frac{\partial \sigma_{tot,yy}}{\partial y} + \frac{\partial \tau_{tot,yz}}{\partial z} &= 0 \\
\frac{\partial \tau_{tot,zx}}{\partial x} + \frac{\partial \tau_{tot,zy}}{\partial y} + \frac{\partial \sigma_{tot,zz}}{\partial z} &= 0
\end{aligned} \tag{4.8}$$

This set of equation is expressed in terms of total stresses: σ_{tot} indicate the total normal stresses and the subscripts stay for the direction along which they develop. τ_{tot} represents

the total shear stress and the first subscript stays for the direction along which they develop and the second one for the direction orthogonal to the plane that contains them. By selecting the proper reference system the stress tensor become symmetric meaning that $\tau_{ij} = \tau_{ji}$.

Total stresses are related to effective stresses by the Terzaghi's principle [19] according following equations:

$$\begin{aligned} \sigma_{tot,xx} &= \sigma_{xx} + \alpha p \quad & \tau_{tot,xy} &= \tau_{xy} \quad & \tau_{tot,xz} &= \tau_{xz} \\ \sigma_{tot,yy} &= \sigma_{yy} + \alpha p \quad & \tau_{tot,yx} &= \tau_{yx} \quad & \tau_{tot,yz} &= \tau_{yz} \\ \sigma_{tot,zz} &= \sigma_{zz} + \alpha p \quad & \tau_{tot,zx} &= \tau_{zx} \quad & \tau_{tot,zy} &= \tau_{zy} \end{aligned} \tag{4.9}$$

where:

- σ represent the normal effective stress and τ the shear stress
- p is the pore-water pressure
- α is the Biot's coefficient which is given by $\alpha = 1 - \frac{C_{grain}}{C_b}$ with C_{grain} compressibility of the solid grains and C_b compressibility of the porous medium. At shallow depths, the compressibility of solid grains C_{grain} is much lower than the compressibility of the porous medium C_b, resulting in $\alpha = 1$.

Eqs. 4.9 are sobstituted in eqs. 4.8 to obtain the Cauchy equilibrium equations in terms of effective stresses:

$$\begin{aligned} \frac{\partial \sigma_{xx}}{\partial x} + \frac{\partial \tau_{xy}}{\partial y} + \frac{\partial \tau_{xz}}{\partial z} &= \frac{\partial p}{\partial x} \\ \frac{\partial \tau yx}{\partial} + \frac{\partial \sigma_{yy}}{\partial y} + \frac{\partial \tau_{yz}}{\partial z} &= \frac{\partial p}{\partial y} \\ \frac{\partial \tau_{zx}}{\partial x} + \frac{\partial \tau_{yz}}{\partial y} + \frac{\partial \sigma_{zz}}{\partial z} &= \frac{\partial p}{\partial z} \end{aligned} \tag{4.10}$$

To develop the equations needed for the structural model, some simplifying assumptions are needed to describe the mechanics of the soil behaviour:

- soil is assumed isotropic;
- only small displacements and deformations are considered, so the derivatives further the first order can be neglected;

- the deformations take place mainly in the solid skeleton, being the soil particles incompressible;
- Terzaghi's effective stress principle holds, meaning that the deformations of the medium depend only on the variation of the effective intergranular stress.

In the flow model the unknowns are displacements and not stresses, it's necessary to recast equilibrium equations in terms of displacements. In the elastic case, Hook's law express the relationships between the effective stress tensor σ and the strain tensor ϵ for an elastic isotropic medium:

$$\begin{bmatrix} \sigma_{xx} \\ \sigma_{yy} \\ \sigma_{zz} \\ \tau_{xy} \\ \tau_{xz} \\ \tau_{yz} \end{bmatrix} = \frac{E}{(1+\nu)(1-2\nu)} \begin{bmatrix} 1-\nu & \nu & \nu & 0 & 0 & 0 \\ \nu & 1-\nu & \nu & 0 & 0 & 0 \\ \nu & \nu & 1-\nu & 0 & 0 & 0 \\ 0 & 0 & 0 & \frac{1-2\nu}{2} & 0 & 0 \\ 0 & 0 & 0 & 0 & \frac{1-2\nu}{2} & 0 \\ 0 & 0 & 0 & 0 & 0 & \frac{1-1\nu}{2} \\ \end{bmatrix} \begin{bmatrix} \epsilon_{xx} \\ \epsilon_{yy} \\ \epsilon_{zz} \\ \epsilon_{xy} \\ \epsilon_{xz} \\ \epsilon_{yz} \end{bmatrix} \tag{4.11}$$

Hook's law 4.11 links stresses to deformations using only two parameters in case of elastic isotropic medium: E is the Young's modulus representing the longitudinal stiffness and ν is the Poisson ratio which express the transversal one.

In case of small deformations stress and strain are related to displacements (u, v, w) according to the De Saint-Venant principle:

$$\begin{aligned} \epsilon_{xx} &= \frac{\partial u}{\partial x} & \sigma_{xx} &= 2\mu\frac{\partial u}{\partial x} + \lambda\epsilon \\ \epsilon_{yy} &= \frac{\partial v}{\partial y} & \sigma_{yy} &= 2\mu\frac{\partial v}{\partial y} + \lambda\epsilon \\ \epsilon_{zz} &= \frac{\partial w}{\partial z} & \sigma_{zz} &= 2\mu\frac{\partial w}{\partial z} + \lambda\epsilon \\ \epsilon_{xy} &= 0.5(\frac{\partial u}{\partial y} + \frac{\partial v}{\partial x}) & \tau_{xy} &= \mu(\frac{\partial u}{\partial y} + \frac{\partial v}{\partial x}) \\ \epsilon_{xz} &= 0.5(\frac{\partial u}{\partial z} + \frac{\partial z}{\partial x}) & \tau_{xz} &= \mu(\frac{\partial u}{\partial z} + \frac{\partial w}{\partial x}) \\ \epsilon_{zy} &= 0.5(\frac{\partial w}{\partial y} + \frac{\partial v}{\partial z}) & \tau_{yz} &= \mu(\frac{\partial v}{\partial z} + \frac{\partial w}{\partial y}) \end{aligned} \tag{4.12}$$

Where μ and λ are called Lame's constants which are functions the physical parameters E and ν: $\mu = \frac{E}{2(1+\nu)}$ and $\lambda = \frac{\nu E}{(1-2\nu)(1+\nu)}$

Stress-strain relationship provided by Hook's law (Eqs. 4.11) are sobstituted in eqs.4.10 and then deformations and stresses are expressed in function of displacements using De Saint-Venant equations 4.12. The equilibrium equations for a porous medium subjected to pressure variations within it written in terms of displacements read:

$$\begin{aligned} \mu\nabla^2\boldsymbol{u} + (\lambda+\mu)\frac{\partial \boldsymbol{\epsilon}}{\partial x} &= \frac{\partial p}{\partial x} \\ \mu\nabla^2\boldsymbol{u} + (\lambda+\mu)\frac{\partial \boldsymbol{\epsilon}}{\partial y} &= \frac{\partial p}{\partial y} \\ \mu\nabla^2\boldsymbol{u} + (\lambda+\mu)\frac{\partial \boldsymbol{\epsilon}}{\partial z} &= \frac{\partial p}{\partial z} \end{aligned} \tag{4.13}$$

Eqs. 4.13 represent the structural model in four unknowns: u, v, w, p. Eqs. 4.13 is coupled with the flow model 4.7 to obtain a system of four equations in four unknowns that can be solved numerically.

In the non-elastic case, the nonlinear law describing the relationship between stress and strain, expressed in differential terms is $d\sigma = D(\sigma)d\epsilon$ [23]:

$$\begin{bmatrix} d\sigma_{xx} \\ d\sigma_{yy} \\ d\sigma_{zz} \\ d\tau_{xy} \\ d\tau_{xz} \\ d\tau_{yz} \end{bmatrix} = \frac{E(1-\nu)}{(1+\nu)(1-2\nu)} \begin{bmatrix} 1 & \frac{\nu}{1-\nu} & \frac{\nu}{1-\nu} & 0 & 0 & 0 \\ \frac{\nu}{1-\nu} & 1 & \frac{\nu}{1-\nu} & 0 & 0 & 0 \\ \frac{\nu}{1-\nu} & \frac{\nu}{1-\nu} & 1 & 0 & 0 & 0 \\ 0 & 0 & 0 & \frac{1-2\nu}{2(1-\nu)} & 0 & 0 \\ 0 & 0 & 0 & 0 & \frac{1-2\nu}{2(1-\nu)} & 0 \\ 0 & 0 & 0 & 0 & 0 & \frac{1-2\nu}{2(1-\nu)} \end{bmatrix} \begin{bmatrix} d\epsilon_{xx} \\ d\epsilon_{yy} \\ d\epsilon_{zz} \\ d\epsilon_{xy} \\ d\epsilon_{xz} \\ d\epsilon_{yz} \end{bmatrix} \tag{4.14}$$

$D(\sigma)$ is the constitutive matrix of the isotropic medium and it is funcion of the stress for nonlinear materials. The coefficient $\frac{E(1-\nu)}{(1+\nu)(1-2\nu)}$ in 4.14, which represents the ratio between the vertical load P and the relative compaction of a rock sample loaded in oedometric conditions, is the inverse of the vertical compressibility C_m:

$$\frac{1}{C_m} = \frac{E(1-\nu)}{(1+\nu)(1-2\nu)} \tag{4.15}$$

In our model, C_m is a nonlinear hysteretic function of the vertical stress σ and ν is a constant. The function linking compressibility and vertical stress is the constitutive law which as been defined consistently with the results of the oedometric tests on soil samples.

4.2 Coupled model

In a fully coupled model the governing equations are reformulated by combining the fluid and structural equations of motion that are solved and integrated in time simultaneously. In the case of uncoupled model instead, at first the flow equation is solved for for pressure which is then used as an input for the structural model. Uncoupled model are less computationally intensive then coupled ones. The advantage of a fully coupled model is that it's more accurate especially when the forcing factor directly affects the stress field. The numerical model implemented in this thesis to solve the Biot's consolidation equations is a 3D fully coupled mixed finite element model developed by Ferronato et al. [24] and then by Castelletto et al. [25]. Equations 4.1, 4.7, and 4.13 form a coupled partial differential system defined on a 3-D domain in which the unknowns are the displacements $\boldsymbol{u} = (u, v, w)$, the pressures p and the fluxes $\boldsymbol{q}$. To minimize the instabilities in the pore pressure solutions a fully coupled mixed finite element formulation is developed. The fluid pore pressure and flux are approximated in the lowest order Raviart–Thomas mixed space, while linear hexahedral FEs are used for the displacements. The second such choice is that a mixed formulation for the flow problem is element-wise mass conservative meaning that mass balance at element scale is respected on the contrary of what happen with standard finite element method. The lowest-order continuous, lowest-order Raviart–Thomas, and piecewise constant spaces are used for the approximation of displacement, Darcy's velocity, and fluid pore pressure, respectively. The finite elements method is a Galerkin variational method [26]: the discretized functions are piecewise polynomials. This implies that the coefficients of the linear combination of the approximated solution are exactly functions on the nodes, elements, faces and centroids, defined by the discretization.

4.2.1 Variational formulation

The variational formulation, also known as weak formulation, allows to find solutions to problems modeled through PDEs. The finite element method starts with the reformulation of a given differential equation into an equivalent variational problem. In this step

differential equations are transformed into algebraic equations easier to solve. The partial differential system composed by equations 4.7, 4.13, 4.1 with proper initial 4.17 and boundary 4.16 conditions is solved numerically using a variational formulation. In order to solve the problem the domain Ω is discretized in n_e elements with n_n nodes and n_f faces. The unknowns of the fully coupled model are:

- vector of displacements in the 3 directions $\boldsymbol{u} = (u, v, w)$ calculated for each node
- water flux $\boldsymbol{q}$ across each element face
- pore-water pressure p computed on the baricenter of each element

The variational formulation is described following the article from Ferronato et al. [24]. Model solution require proper initial and boundary conditions. Two types of boundary conditions have been used in this model: Dirichlet boundary conditions state the value that the solution function f to the differential equation must have on the boundary of the domain while Neumann boundary conditions specify the normal derivative of the unknown function at a boundary. Boundary conditions, on the 3D domain Ω with frontier Γ can be written as:

$$\begin{cases} \boldsymbol{u}(\boldsymbol{x},t) = \boldsymbol{u}_D(\boldsymbol{x},t) & over \quad \Gamma_D \\ \boldsymbol{\sigma}_{tot}(\boldsymbol{x},t)\boldsymbol{n}(\boldsymbol{x}) = \boldsymbol{t}_N(\boldsymbol{x},t) & over \quad \Gamma_N \\ p(\boldsymbol{x},t) = p_D(\boldsymbol{x},t) & over \quad \Gamma_p \\ \boldsymbol{v}(\boldsymbol{x},t)\cdot\boldsymbol{n}(\boldsymbol{x}) = \boldsymbol{q}_N(\boldsymbol{x},t) & over \quad \Gamma_q \end{cases} \tag{4.16}$$

Initial conditions are expressed as:

$$\begin{cases} \boldsymbol{u}(\boldsymbol{x},0) = \boldsymbol{u}_0(\boldsymbol{x}) \\ p(\boldsymbol{x},t) = p_0(\boldsymbol{x}) \end{cases} \tag{4.17}$$

In Eqs. 4.16 and 4.17 $\Gamma_D \cup \Gamma_N = \Gamma_p \cup \Gamma_q = \Gamma$, $\boldsymbol{\sigma}_{tot}$ is the tensor of total stresses function of position and time, $\boldsymbol{n}$ is the outer normal to Γ function of position and $\boldsymbol{x}$ is the position vector in the 3D space.

The displacement vector $\boldsymbol{u}(\boldsymbol{x},t)$ is approximated in a functional space generated by continuous piecewise linear polynomials l_i, where $i = 1, ..., n_n$, recalling that n_n is the

total number of nodes in the domain, n_e is the number of elements, n_f is the number of faces. The medium displacement $\boldsymbol{u}(\boldsymbol{x},t)$ is hence defined as:

$$\boldsymbol{u}(\boldsymbol{x},t) = \begin{bmatrix} u(\boldsymbol{x},t) \\ v(\boldsymbol{x},t) \\ w(\boldsymbol{x},t) \end{bmatrix} \simeq \begin{bmatrix} \sum_{i=1}^{n_n} l_i(\boldsymbol{x}) u_i(t) \\ \sum_{i=1}^{n_n} l_i(\boldsymbol{x}) v_i(t) \\ \sum_{i=1}^{n_n} l_i(\boldsymbol{x}) w_i(t) \end{bmatrix} = N_u(\boldsymbol{x})\boldsymbol{u}(t) \tag{4.18}$$

Pore-water pressure p, which is computed in the baricenter of each element, is approximated in the space of piecewise constant polynomials as:

$$p(\boldsymbol{x},t) \simeq \sum_{j=1}^{n_e} h_j(\boldsymbol{x}) p_j(t) = \boldsymbol{h}^T(\boldsymbol{x})\boldsymbol{p}(t) \tag{4.19}$$

where $h_j(x)$ is the basis function equal to one for the j-th element and equal to 0 elsewhere.

The Darcy's velocity vector $\boldsymbol{q}$ across each element face is approximated in the lowest order Raviart-Thomas mixed space:

$$\boldsymbol{q}(\boldsymbol{x},t) \simeq \sum_{k=1}^{n_f} \boldsymbol{w}_k(\boldsymbol{x}) q_k(t) = W(\boldsymbol{x})\boldsymbol{q}(t) \tag{4.20}$$

$q_k(t)$ represent the water flux across the faces of the elements of the mesh and $\boldsymbol{w}_k(t)$ are vectorial functions defined in $\mathbb{R}^3$ associated with the k-th face that belongs to the j-th hexaedron.

The aim now is to write the coupled system 4.7, 4.13 and 4.1 in weak form: the main idea of the weak form is to turn the differential equation into an integral equation. For Eq. 4.13 the integral form is obtained by minimizing the total potential energy in the domain by applying the virtual work principle:

$$\int_\Omega \boldsymbol{\epsilon}^{v,T} \boldsymbol{\sigma}_{tot} d\Omega = \int_\Omega \boldsymbol{u}^{v,T} \boldsymbol{b} d\Omega + \int_{\Gamma_N} \boldsymbol{u}^{v,T} \boldsymbol{t}_n d\Gamma \tag{4.21}$$

where:

- $\boldsymbol{\epsilon}$ is the vector of deformations defined as $\boldsymbol{\epsilon} = B_u \boldsymbol{u}$ with B_u the strain elastic matrix
- $\boldsymbol{t}_N$ is the normal tension

- $\boldsymbol{b}$ is the volumetric force acting on the porous medium
- v apex identifies the virtual variables
- $\boldsymbol{\sigma}_{tot}$ is the total stress vector

According to Terzaghi principle indtroduced before Eq. 4.9 total stress vector can be rewritten as:

$$\boldsymbol{\sigma}_{tot} = \boldsymbol{\sigma} - \alpha p \boldsymbol{i} \tag{4.22}$$

with $\boldsymbol{i}$ being the Kronecker delta in vectorial form $[1,1,1,0,0,0]^T$ and $\boldsymbol{\sigma}$ is the effictive stress vector $\boldsymbol{\sigma} = [\sigma_x, \sigma_y.\sigma_z, \tau_x y, \tau_x z, \tau_y z]^T = D_e \boldsymbol{\epsilon}$ where D_e is the elastic constant matrix defined in Eq. 4.11. Equation 4.21 becomes:

$$(\int_\Omega B_u^T D_e B_u d\Omega)\boldsymbol{u} - \int_\Omega \alpha B_u^T \boldsymbol{i} p d\Omega = \int_\Omega N_u^T \boldsymbol{b} d\Omega + \int_{\Gamma_N} N_u^T \boldsymbol{t}_N d\Gamma \tag{4.23}$$

Replacing pore pressure approximation 4.19 into 4.23 the discrete form of equation 4.13 is given:

$$K\boldsymbol{u} - Q\boldsymbol{p} = \boldsymbol{f_1} \tag{4.24}$$

where:

- $K = \int_\Omega B_u^T D_e B_u d\Omega$
- $Q = \int_\Omega \alpha B_u^T \boldsymbol{I} \boldsymbol{h}^T d\Omega$
- $\boldsymbol{f_1} = \int_\Omega N_u^T \boldsymbol{b} d\Omega + \int_{\Gamma_N} N_u^T \boldsymbol{t}_N d\Gamma$

The equation 4.24 represents the structural model expressed in discrete form: it's now necessary to write also the other two equations composing the PDEs system using the weak formulation. The integral form of equations 4.1 and 4.7 is obtained by applying a standard Galerkin approach. It's a weighted residual method that start start with an estimate of the the solution and demand that its weighted average error is minimized. Using the approximations 4.18, 4.20 and 4.19 the integral forms of the flow model and Darcy's law are:

$$\int_\Omega \boldsymbol{h} \nabla \cdot \boldsymbol{q} d\Omega + \int_\Omega \boldsymbol{h} \frac{\partial n \beta p}{\partial t} d\Omega + \int_\Omega \boldsymbol{h} \frac{\partial \alpha \nabla \cdot \boldsymbol{u}}{\partial t} d\Omega = \int_\Omega \boldsymbol{h} f d\Omega \tag{4.25}$$

$$\int_\Omega W^T \bar{\boldsymbol{k}}^{-1} \boldsymbol{q} d\Omega + \int_\Omega W^T \nabla p d\Omega = 0 \tag{4.26}$$

Where the Biot's coefficient α, fluid compressibility β and the porosity n are assumed to be constant in time and $\bar{k}^{-1} = \frac{k}{\rho g}$ is given by hydraulic conductivity tensor divided by the specific weight of the fluid. Applying the weak form for the last integral in Eq. 4.26 the semi-discrete mixed finite elements form for flow model and Darcy's law is:

$$B^T \boldsymbol{q} + P\boldsymbol{p} + Q^T \boldsymbol{u} = \boldsymbol{f_2} \tag{4.27}$$

$$A\boldsymbol{q} - B\boldsymbol{p} = \boldsymbol{f_3} \tag{4.28}$$

with:

- $A = \int_\Omega W^T \bar{\boldsymbol{k}}^{-1} W d\Omega$ is the mass matrix which is multiplied by the the Darcy's velocity $\boldsymbol{q}$
- $B = \int_\Omega \boldsymbol{\omega} \boldsymbol{h}^T d\Omega$ is the coupling matrix between velocity and displacements and $\boldsymbol{\omega}$ is a vector with components equal to $div \boldsymbol{w}_{nf}$ where n_f is the number of faces.
- $P = \int_\Omega n\beta \boldsymbol{h}\boldsymbol{h}^T d\Omega$, the capacity matrix
- $\boldsymbol{f_2}$ and $\boldsymbol{f_3}$ are vectors containing known terms: $\boldsymbol{f_2} = \int_\Omega \boldsymbol{h} f d\Omega$ and $\boldsymbol{f_3} = -\int_{\Gamma_p} p_D W^T \boldsymbol{n} d\Gamma$

The original system composed by PDEs is now expressed by differential-algebraic Equations 4.24, 4.27, 4.28, with the prescribed Dirichlet and Neumann boundary conditions.

4.2.2 Numerical implementation

The system of differential-algebraic equations 4.24, 4.27 and 4.28 is integrated in time using the θ-method: the time interval is divided in n_t subintervals $I_n = (t_n, t_{n+1})$ with $n = 0, 1, ..., n_t - 1$ and in each interval time derivatives are discretized by a first order incremental ratio while the other variables are approximated by a linear combination of the values at time t_n and $t_{n+1} = t_n + \Delta t_n$ with coefficients $(1 - \theta)$ and θ respectively. Making an example an intermediate instant τ is given by:

$$\tau = \theta(t + \Delta t) + (1 - \theta)t \tag{4.29}$$

θ is scalar varying from 0 to 1 and it controls accuracy and stability of the method.

The discrete solution obtained is the following:

$$\begin{aligned}
&\theta[K\boldsymbol{u}^{t+\Delta t} - Q\boldsymbol{p}^{t+\Delta t}] = (1-\theta)[Q\boldsymbol{p}^{t} - K\boldsymbol{u}^{t} + \boldsymbol{f}_1^{t}] + \theta\boldsymbol{f}_1^{t+\Delta t} \\
&\frac{Q^T\boldsymbol{u}^{t+\Delta t} + P\boldsymbol{p}^{t+\Delta t}}{\Delta t} + \theta B^T\boldsymbol{q}^{t+\Delta t} = (1-\theta)[\boldsymbol{f}_2^{t} - B^T\boldsymbol{q}^{t}] + \frac{Q^T\boldsymbol{u}^{t} + P\boldsymbol{p}^{t}}{\Delta t} + \theta\boldsymbol{f}_2^{t+\Delta t} \\
&\theta[A\boldsymbol{q}^{t+\Delta t} - B\boldsymbol{p}^{t+\Delta t}] = (1-\theta)[B\boldsymbol{p}^{t} - A\boldsymbol{q}^{t} + \boldsymbol{f}_3^{t}] + \theta\boldsymbol{f}_3^{t+\Delta t}
\end{aligned} \tag{4.30}$$

Rearranging Eqs. 4.30, the numerical solution at time t_{n+1} is obtained by solving the linear algebraic system:

$$\mathcal{A}\boldsymbol{z}^{t+\Delta t} = \boldsymbol{f}^{t} \tag{4.31}$$

where

$$\mathcal{A} = \begin{bmatrix} P & Q^T & \gamma B^T \\ Q & -K & 0 \\ \gamma B & 0 & -\gamma A \end{bmatrix} \quad \boldsymbol{z}^{t+\Delta t} = \begin{bmatrix} \boldsymbol{p}^{t+\Delta t} \\ \boldsymbol{u}^{t+\Delta t} \\ \boldsymbol{q}^{t+\Delta t} \end{bmatrix} \quad \boldsymbol{f}^{t} = \begin{bmatrix} \boldsymbol{f}^{p} \\ \boldsymbol{f}^{u} \\ \boldsymbol{f}^{q} \end{bmatrix} \tag{4.32}$$

and

$$\begin{aligned}
\boldsymbol{f}^{p} &= (\Delta t - \gamma)[\boldsymbol{f}_2^{t} - B^T\boldsymbol{q}^{t}] + Q^T\boldsymbol{u}^{t} + P\boldsymbol{p}^{t} + \gamma\boldsymbol{f}_2^{t+\Delta t} \\
\boldsymbol{f}^{u} &= \psi[K\boldsymbol{u}^{t} - Q\boldsymbol{p}^{t} - \boldsymbol{f}_1^{t}] - \boldsymbol{f}_1^{t+\Delta t} \\
\boldsymbol{f}^{q} &= (\Delta t - \gamma)[A\boldsymbol{q}^{t} - B\boldsymbol{p}^{t} - \boldsymbol{f}_3^{t}] - \gamma\boldsymbol{f}_3^{t+\Delta t}
\end{aligned} \tag{4.33}$$

with $\gamma = \theta\Delta t_n$ and $\psi = \frac{1-\theta}{\theta}$.

The non linearity is solved using an explicit scheme meaning that the soil compressibility C_m is calculated as a function of σ_z (Eq. 4.14), computed at the previous time step. Linear algebraic systems can be solved by applying the so called Krylov subspace methods: in paricular as $\mathcal{A}$ is a non-symmetric matrix, a global Bi-Conjugate Gradient Stabilized (Bi-CGStab is is one of the best known Krylov subspace methods) algorithm has been applyed t solve the linear system [27]. Bi-CGSTAB is an iterative method developed for the numerical solution of nonsymmetric linear system: the method start with an initial guess of the solution $\boldsymbol{x}_0$ and then the algorithm procedure is repeated until convergence that is when the prescribed residual is obtained. The convergence of iterative method can

be accelerated by using preconditioners [28]. Preconditioning consist on the application of a transformation, called the preconditioner, that conditions a given problem into a form that is more suitable for numerical solving methods: a preconditioner P of a matrix A is a matrix such that $P^{-1}A$ has a small condition number than A. In this case, a block preconditioner is applied to improve the convergence of the numerical scheme.

5 Model setup

The coupled model described in the previous chapter is applied to mimic the loading experiments carried out at the La Grisa, Campalto and Saline salt marshes, with the final purpose of characterizing the soil properties. In the following sections the 3D domain mesh, boundary and initial conditions, lithostratigraphy and material properties used in the modeling approach are presented.

5.1 3D domain

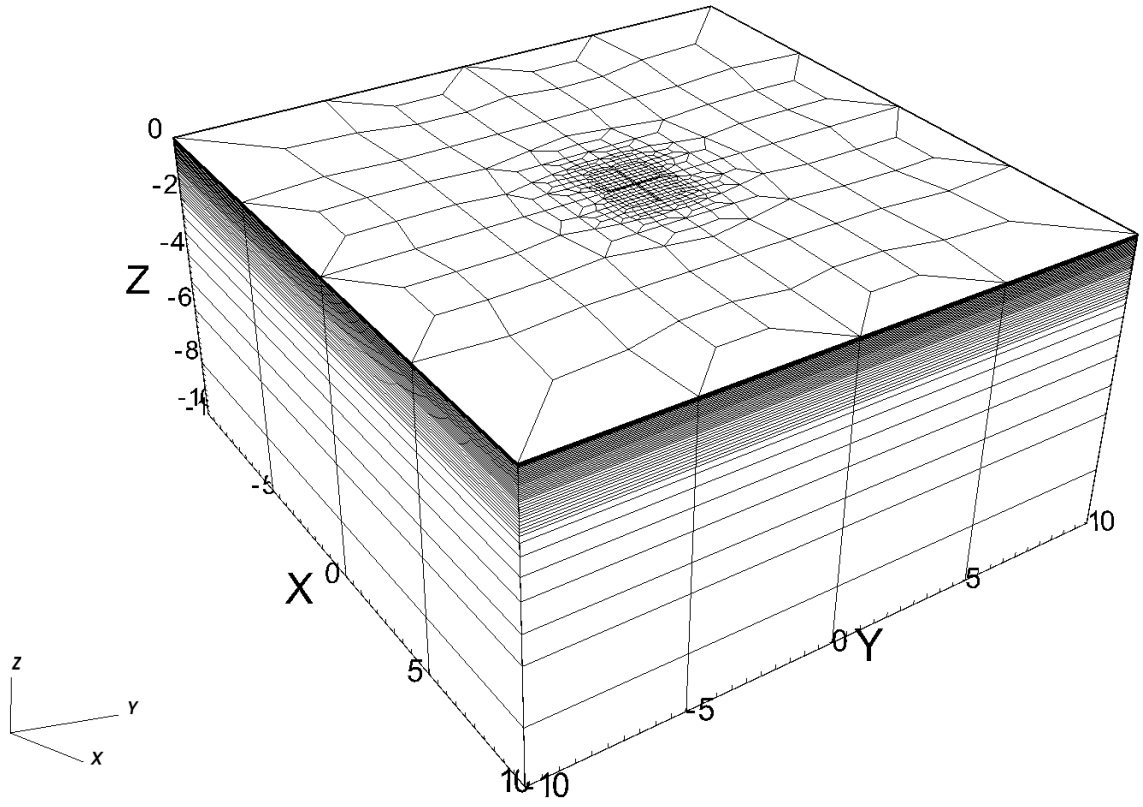

Figure 5.1: 3D mesh of the model domain

The first step of the model setup is the definition of the domain and its discretization. A 10 m×10 m surface area centered on the loading test, has been selected and discretized by a 2D mesh made by quadrilateral elements, generated by the program Automesh. The 3D domain has been created by projecting the nodes and of the 2D mesh along the vertical direction and extending the quadrilateral elements to hexahedral elements. This procedure results in a 3D domain of dimensions 10 m×10 m×10 m along x, y and z directions. The inner zone of the mesh, coinciding with the loading area, has a denser discretization

because, in this portion of the domain, a greater accuracy is required while moving towards the external boundaries the mesh become gradually coarser. A lighter discretization in the external zones allow to reduce the computational time of the simulation. Along the vertical direction, 47 layers of variable thickness have been defined according to the site lithostratigraphy. Shallow layers are more refined than the bottom ones to achieve a more accurate solution below the load. The 3D mesh is composed by 25872 nodes, 24910 elements and 75636 faces (Fig. 5.1).

5.2 Initial and boundary conditions

The second step consists of defining the initial and boundary conditions which are necessary to solve the coupled system of equations. Initial and boundary conditions are prescribed on nodes, elements or faces of the hexaedral elements depending on the considered variable. Displacements are defined on the nodes, pressures on the element centroid and flows on the element faces (Fig. 5.2).

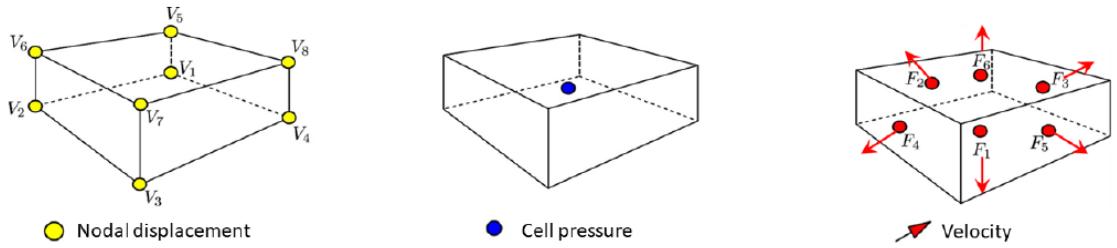

Figure 5.2: Variables definition on hexaedric elements

The model solves the equations with respect to an initial state, which is assumed equilibrated, displacements, pressures and flow vectors are initialized to zero in the whole domain. The initial stress distribution in the domain σ_{z0} is calculated as $\sigma_{z0} = \gamma_s z$ where $\gamma_s = 9$ kN/m^3 is the specific weight of the soil, assumed to be homogeneous, and z is the depth.

Two kinds of boundary conditions can be used in this model. Neumann boundary conditions specifies the values of the normal derivative of the unknown applied at the boundary of the domain and Dirichlet conditions specify the values of the unknown itself on the boundary.

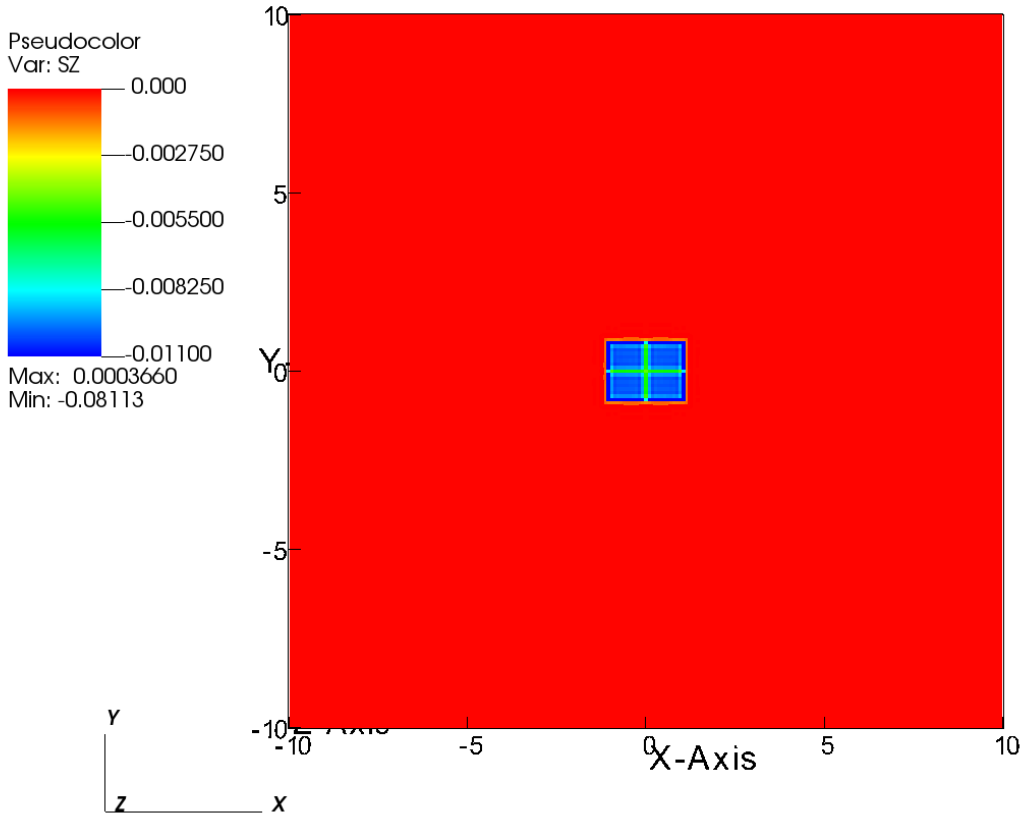

(a) Load applied on the surface nodes of the 3D mesh. The load is imposed on the nodes of the mesh corresponding to the four wooden pallets (in blue). The figure shows the distribution of vertical stress (SZ) expressed in MPa induced by the second loading phase of 11.3 kPa on the surface nodes.

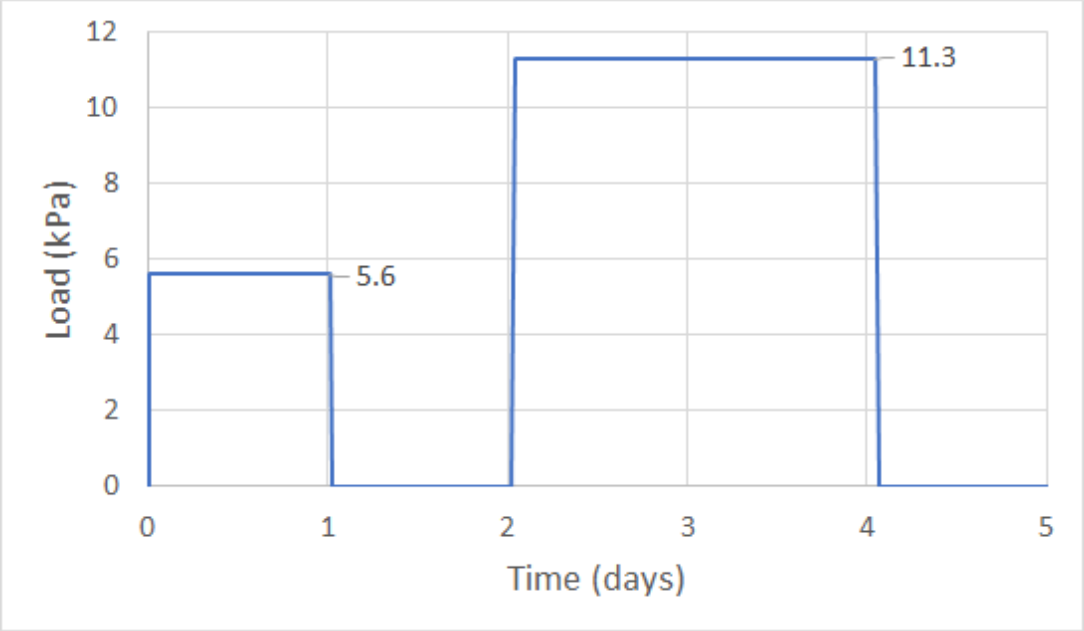

(b) Load evolution over time during the experiments

Figure 5.3: Modeling the load evolution during the experiments

The Neumann boundary conditions concerning the displacements are imposed underneath the loading area. The load imposed on the nodes reflects the in-situ loading-unloading operations during the experiments. In the first loading phase, the load equals 5.6 kPa and in the second phase it amounts to 11.3 kPa (Fig. 5.3b). The time required for the emptying or filling of the tanks is 15 minutes and 30 minutes for the first and the second phase resulting in a constant loading-unloading rate during the two cycles. It has been assumed that during the tank filling-emptying procedures the load increases-decreases linearly in time up to the desired value of 5.6 kPa or 11.3 kPa. In the model, the value of the load is imposed on the superficial nodes within the loading area, corresponding to the four wooden pallets (Fig. 5.3a). However, to take into account the finite elements discretization of the loading area and being A_e the area of the mesh elements constituting the loading area, the nodes corresponding to the vertices of the loading area have influence area $A_e/4$, those on the sides have influence area $A_e/2$ while for central nodes influence area is equal to A_e.

The Dirichlet boundary conditions are imposed as follows:

- vertical displacements are null on the bottom of the domain;
- horizontal displacements are null on the bottom and along the lateral boundaries;
- pressures are null (atmospheric pressure) on the surface faces and they follow an hydrostatic distribution along the lateral boundaries of the domain;
- flow is null trough the surface faces where the load is applied and trough the model bottom.

5.3 Materials and soil properties

The model is calibrated by a trial and error procedure searching for a proper set of hydro-geomechanical parameters that allow to reproduce satisfactorily the recorded data in both the loading-unloading cycles.

As presented in Chapter 2, each experimental site is characterized by a different vertical stratigraphy. The 3D mesh is divided in layers of different materials according to the vertical distribution of the soil layers observed in the field. Each layer is assumed to be homogeneous, meaning that a single set of parameters suffices to describe each material.

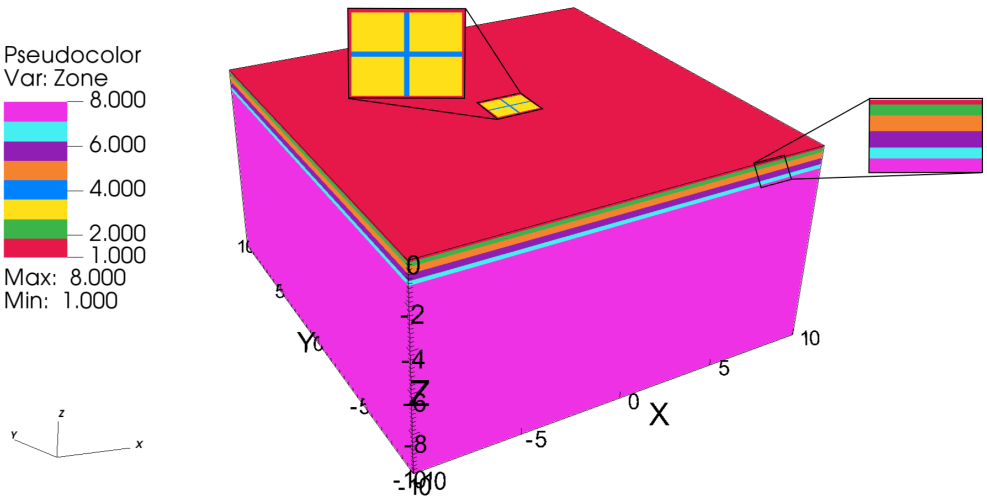

Figure 5.4: Graphycal representation of model layering defined for the the experiment of Campalto. The legend from 1 to 8 represent the 8 materials. On the mesh surface elements representing the wooden pallets and the geotexile are depicted in yellow and blue, respectively. The elasto-plastic (nonlinear) materials correspond to the two shallowest soil layers represented in red and green. The other colors represent the different soil layers. The last layer (in light purple) is stiffer than the upper ones and it is introduced to impose the boundary conditions sufficiently far from the soil units experiencing the local-related stress change.

The set of parameters describing the hydrogeomechanical properties of each layer consists of the hydraulic conductivity k, assumed to be isotropic, the Poisson's ratio ν, the Young's modulus E, the constitutive law parameters and the parameter s that express the ratio between the compressibility during the loading over the compressibility in unloading conditions. Porosity n and preconsolidation stress σ_p are assumed to be constant in the whole domain. n has been fixed to 0.44 in the three simulations, σ_p is different in the three models. The soil parameters that influence more the solution are the soil stiffness and the hydraulic conductivity.

Each layer can be modeled as linear elastic or elasto-plastic. In case of linear materials the soil stiffness is expressed with a constant Young's modulus E. For nonlinear materials, the soil stiffness is computed as a function of the preconsolidation stress σ_p, the constitutive law parameters, and s.

The chosen layering has to be representative of the field conditions. An example of layering is presented in Fig. 5.4 for the experiment of Campalto. The superficial elements below the loading area are constituted by four wooden pallets and the geotexile in the space between them. They are modeled assuming a stiffer (about 3 orders of magnitude) and

less permeable (about 2 orders of magnitude) material than those representing the soil layers. The upper soil layers up to a depth of 20-30 cm are assumed to be nonlinear (elasto-plastic behavior with hysteresis) while the deeper layers are modeled as linear. This choice reflects the displacement observations presented in the Chapter 3. At shallow depths, marsh soil behave as a nonlinear material with permanent deformations after each loading-unloading cycle, while at larger depths (C50) soil response to loading-unloading cycles seems to be more linear (deformations during loading phases are limited and they are almost completely recovered in unloading phases). Deep soil layer are, in fact, stiffer and more consolidated than the shallow ones due to the weight of the overlying sediments.

5.4 Constitutive laws and soil stiffness computation in case of linear and nonlinear materials

Constitutive laws relate the soil mechanical properties to the actual stress field.

The simplest constitutive relation is linear elasticity in which stresses and strains are related by constant coefficients. As explained in Section 4.1.2 the relationships between stresses and deformations are expressed by means of the Young's modulus and the Poisson's ratio which are constant, i.e. independent on stresses. In this case, when a soil is loaded it experiences a reduction in volume which is completely recovered when the load is removed.

However, a more representative behavior of shallow soils differs from the linear elastic assumption. In particular, natural soils display a nonlinear elasto-plastic behavior with elastic properties if the vertical effective stress value is smaller than a threshold value called the preconsolidation stress. This is maximum effective vertical stress a soil volume experienced in the past. When stress reaches and overcomes the past preconsolidation stress, the soil deformation is plastic, meaning that even removing completely the load a certain fraction of deformations is unrecoverable.

The model used in this thesis allows modeling linear elastic and nonlinear elasto-plastic soils. In the last case, the calculation of the soil stiffness depends on the value of the current effective stress and the preconsolidation stress as follows:

- if the effective stress σ_z is larger, in modulus, than the preconsolidation stress σ_p (virgin loading conditions), this latter must be updated, and the oedometric modulus

and soil compressibility are given with the empirical relationship:

$$\begin{aligned} M &= a\sigma_z^b + c \\ C_m &= \frac{1}{M} = \frac{1}{a\sigma_z^b + c} \end{aligned} \tag{5.1}$$

- if $\text{mod}\ \sigma_z < \text{mod}\ \sigma_p$ (unloading conditions) the compressibility is calculated according to the following procedure. First, the compressibility at the end of the loading phase, at the inversion point between loading and unloading, is given by Eq. 5.1 with $\sigma_z = \sigma_{z,max}$:

$$C_m^I = \frac{1}{a\sigma_{z,max}^b + c} \tag{5.2}$$

  Then, a constant compressibility in unloading conditions is calculated as:

$$C_m = C_m^I / s \tag{5.3}$$

  Where s is the ratio (greater than 1) between the soil compressibility in loading and unloading conditions at the inversion point between the two phases. At the inversion point between loading and unloading operations soil compressibility decreases suddenly depending on the value of s (the higher the value of s the higher the difference between the two compressibilities).

Finally, the soil stiffness E is calculated for nonlinear materials as a function of the soil compressibility and the Poisson's ratio:

$$E = \frac{(1-2\nu)(1+\nu)}{C_m(1-\nu)} \tag{5.4}$$

Since $E \propto \frac{1}{C_m}$, the soil stiffness during the loading phase results lower than the one during the unloading. As a result, some permanent deformations will remain after each loading-unloading cycle. Soil stiffness E is initialized in the domain according to the value of preconsolidation stress and initial stress σ_{z0}. If $\sigma_{z0} = \gamma_s z < \sigma_p$ initial compressibility is given by Eq. 5.3 with $\sigma_{z,max} = \sigma_{z0} - \sigma_p$. If $\sigma_{z0} < \sigma_p$ initial compressibility is calculated according to Eq. 5.1 with $\sigma_z = \sigma_{z0}$. Initial value of E is computed from Eq. 5.4 in both cases.

The plots in Fig. 5.5 qualitatively explain how the soil stiffness E varies during a loading-unloading cycle depending on the values of σ_z and σ_p for four different cases:

1. elastic material (Fig. 5.5a);
2. elasto-plastic material with $\sigma_{z0} < \sigma_p$ and $\sigma_{z,max} < \sigma_p$ (Fig. 5.5b);
3. elasto-plastic material with $\sigma_{z0} < \sigma_p$ and $\sigma_{z,max} > \sigma_p$ (Fig. 5.5c);
4. elasto-plastic with $\sigma_{z0} > \sigma_p$ and $\sigma_{z,max} > \sigma_p$ (Fig. 5.5d).

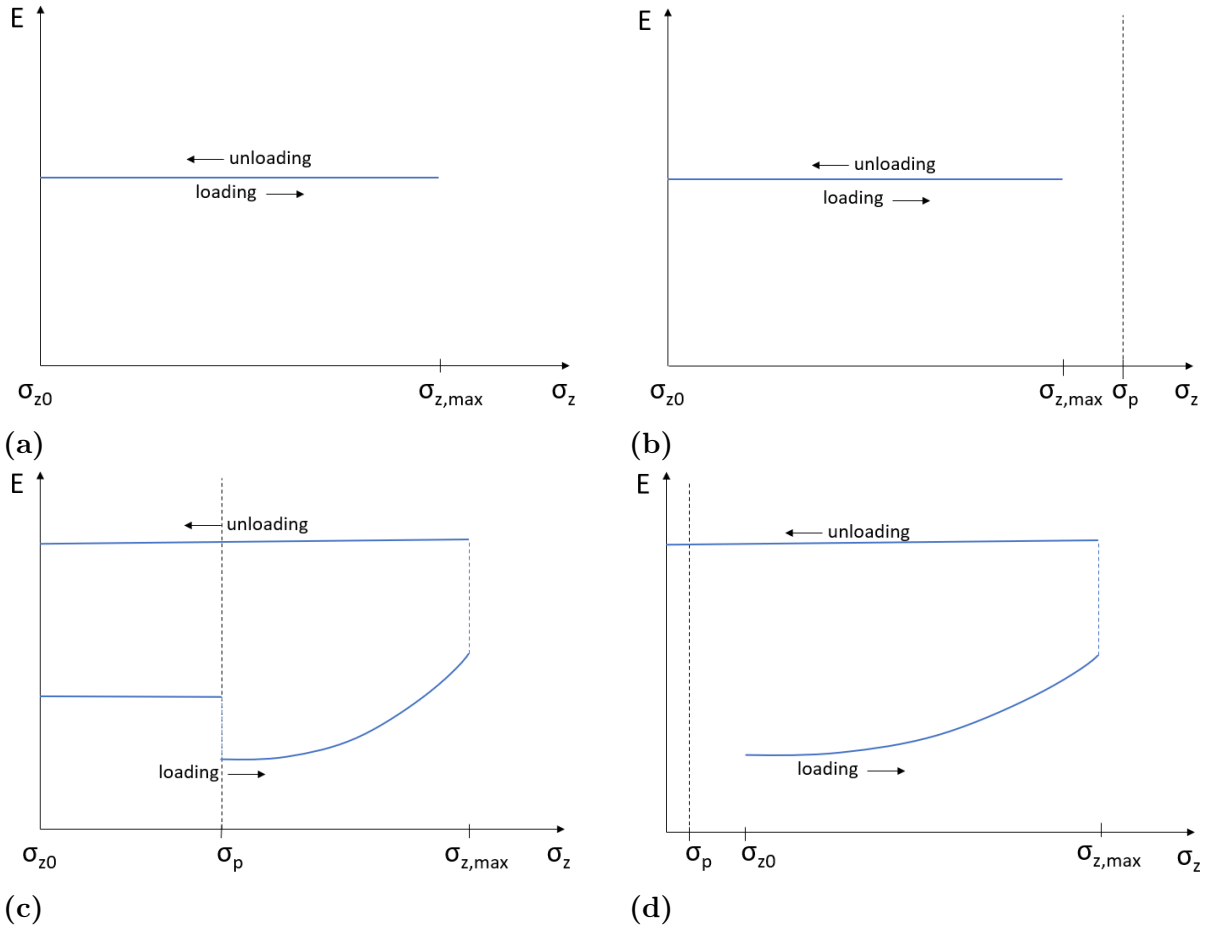

Figure 5.5: Soil stiffness behavior during a loading-unloading cycles in function of σ_z in four different cases. (a) For linear materials E is constant regardless of preconsolidation stress σ_p and vertical stress σ_z. The other three cases display the variation of E for the possible combinations of σ_z and σ_p for nonlinear materials. (b) If $\sigma_{z0} < \sigma_p$ and $\sigma_{z,max} < \sigma_p$ soil stiffness is constant because the preconsolidation threshold is never reached. (c) If $\sigma_{z0} < \sigma_p$ and $\sigma_{z,max} > \sigma_p$, E is constant until $\sigma_z = \sigma_p$, then it becomes function of σ_z (Eq. 5.1). At the inversion point between loading and unloading conditions, σ_z becomes lower than the updated σ_p, given by the loading phase, and E increases depending on the value of s (Eq. 5.3). E remains constant during the whole unloading phase. (d) If $\sigma_{z0} > \sigma_p$ and $\sigma_{z,max} > \sigma_p$, since the beginning of the loading phase, E increases as a function of σ_z. During unloading, the soil stiffness behavior is the same of case (c).

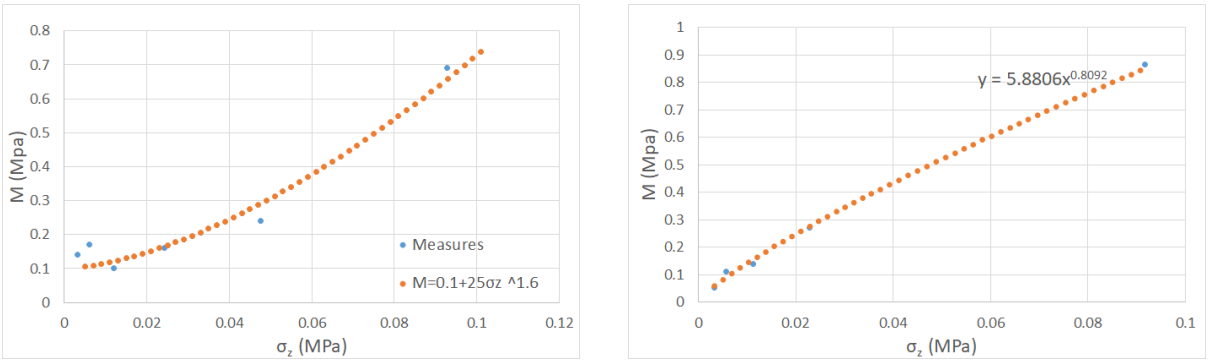

(a) **(b)**

Figure 5.6: Experimental constitutive laws obtained form oedometric tests on the shallowest soil samples from Campalto (a) at a depth 0.05 m and La Grisa (b) at a depth 0.16 m.

Campalto: sample depths	Constitutive law	La Grisa: sample depths	Constitutive law
0.04 m	$M = \frac{1}{C_m} = 0.1 + 25\sigma_z^{1.6}$	0.16 m	$M = \frac{1}{C_m} = 5.88\sigma_z^{0.81}$
0.24 m	$M = \frac{1}{C_m} = 0.45 + 25\sigma_z^{1.6}$	0.65 m	$M = \frac{1}{C_m} = 16.83\sigma_z^{0.81}$
0.5 m	$M = \frac{1}{C_m} = 0.55 + 25\sigma_z^{1.6}$	0.82 m	$M = \frac{1}{C_m} = 10.48\sigma_z^{0.37}$

Table 5.1: Constitutive laws for Campalto and La Grisa marsh soils at different depths from the marsh platform . The general equation describing the relationship between oedometric modulus M and the effective stress σ_z is a power law with general equation $M = \frac{1}{C_m} = a\sigma_z^b + c$. M, σ_z and c are expressed in MPa, a and b are dimensionless.

Being σ_p unique for all the domain, the nonlinear soil layers overcome the preconsolidation threshold in different instants. Deeper layers, characterized by an higher initial σ_z than the shallower layers ($\sigma_{z0} = \gamma_s z$), achieve the preconsolidation threshold before than the latter.

The choice of the nonlinear constitutive law has been taken considering the results of the oedometric tests presented in the Chapter 2. The power law with three parameters (a, b and c) is the relation that allows to better fit the experimental points (σ_z, M) (Eq. 5.1).

A fitting procedure has been applied to the oedometric data sets obtained for La Grisa and Campalto. Fig. 5.6 shows two examples of the fitted law and Table 5.1 represents the constitutive laws for the different soil samples.

These results highlight that in both sites the compressibility of salt-marsh soils generally decreases with depth. Unfortunately, no oedometric tests have been already available

for Le Saline salt marsh, therefore the same constitutive law obtained from La Grisa oedometric data sets has been used for the Le Saline simulation.

5.5 Secondary consolidation

When a saturated soil layer consisting of fine-grained soils is subjected to loading, the resulting deformation occurs in two successive phases, primary consolidation and secondary. During the primary consolidation phase, the soil structure deformation is related to the ability of the pore fluid to drain. Initially, the load is instantaneously transferred to the pore fluid whose pore pressure increases. This excess pore pressure dissipates over time as the soil drains, and the initial total stress applied becomes effective as it transfers from the pore fluid to the soil structure with the increase of effective intergranular stress that causes soil deformation (compaction). When the primary consolidation ends, the excess pore pressure have been completely dissipated. However, the soil continues to deform without pore-water pressure changes, a phase referred to as secondary consolidation. Secondary consolidation is due to the rearrangement of the soil skeleton after a disturbance induced during the primary consolidation. The deformations induced by the secondary consolidations are also known as creep deformations.

The displacements measured during the loading tests carried out in the Venice Lagoon are characterized by evident creep deformation. The simulation used can simulate only primary consolidation process. Consequently, the data measured during the in-situ experiments, presented in Section 3, have been cleaned from the effect of the secondary deformation by removing the displacements recorded after the complete dissipation of the pore-water pressure. To this aim, it is necessary to compute the secondary consolidation coefficient C_α, also known as creep coefficient. The creep coefficient represents the slope of the deformations (ϵ)-logarithm of time curve (Fig. 5.7c), $C_\alpha = \frac{\Delta\epsilon}{\Delta log(t)}$. The deformation has been calculated considering the transducers C0, C10, C50 (C40 for La Grisa experiment) records as $\epsilon = \frac{\Delta h}{H}$. Δh is the difference between displacements and H the thickness of the soil layer between two sensors. C_α has been evaluated for the two loading phases of the in-situ experiments and for two soil layers: the one bounded by sensors C0 and C10 ($C_{\alpha,1}$ for layer 1) with thickness 10 cm and the soil layer within sensors C10 and C50 ($C_{\alpha,2}$ for layer 2).

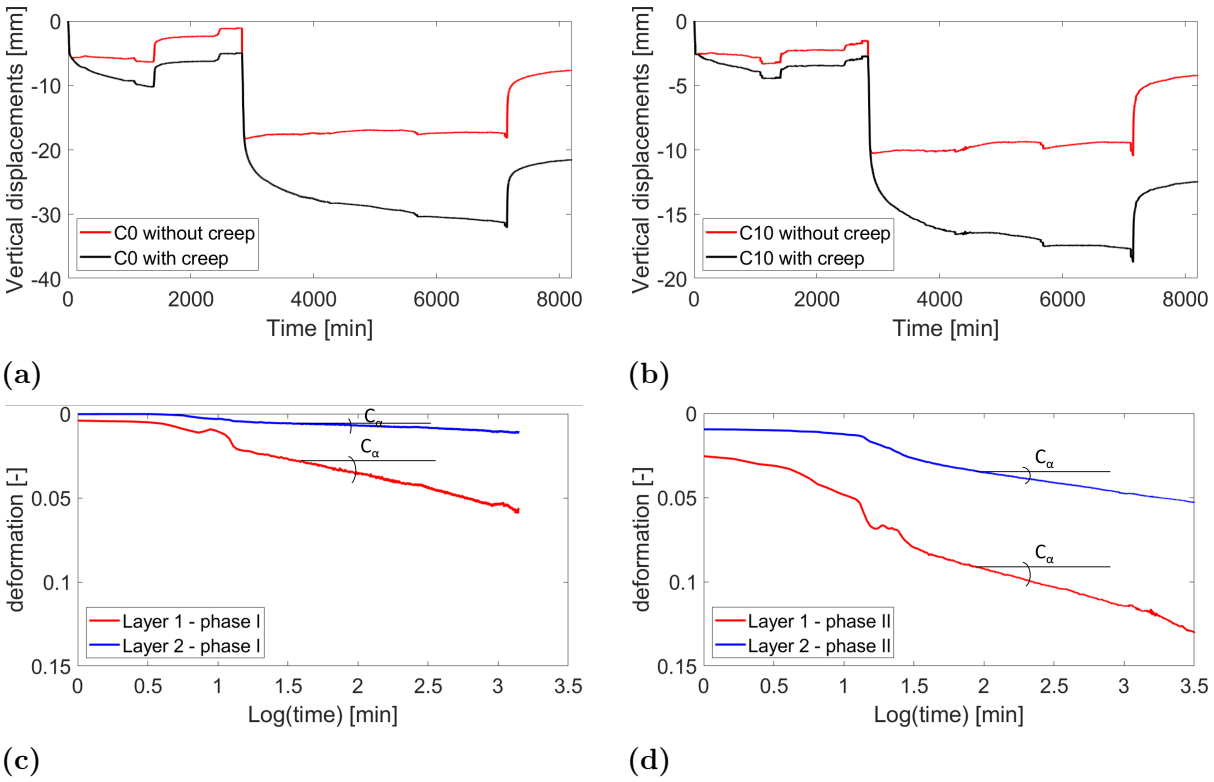

Figure 5.7: Comparison between the recorded displacements in La Grisa experiment with (in black) and without (in red) the creep effect, for displacement transducers (a) C0 and (b) C10, respectively. Plots (c) and (d) shows deformations of the two considered soil layers (layer 1 is bounded by sensors C0 and C10 and layer 2 is within sensors C10 and C40) versus time in a semilogarithmic plot during the first and the second loading phase, respectively of La Grisa in-situ experiment.

Once $C_{\alpha 1,2}$ are known, the amount of vertical displacements due to secondary deformations for the two layers can be evaluated as:

$$\begin{aligned} d_{s,1} &= C_{\alpha,1} H_1 log \frac{t}{t_{ref}} \\ d_{s,2} &= C_{\alpha,2} H_2 log \frac{t}{t_{ref}} \end{aligned} \tag{5.5}$$

with t_{ref} is the time at which all the excess of pore-water pressure have been dissipated and the secondary consolidation starts, and t is the time from the beginning of the loading phase. The cleaned displacements of sensor C0 have been calculated removing $d_{s,1} + d_{s,2}$ from the record provided by the sensor. The cleaned displacements of sensor placed at 10 cm below the ground level (C10, M10, E10) have been calculated by removing $d_{s,2}$ from the record provided by the sensors. Displacements recorded at 50 cm below the ground level C50 (C40 for La Grisa) have not been cleaned by creep deformations.

This procedure has been applied to the measurements of vertical displacements collected in Campalto and La Grisa experiments. The particular evolution of vertical displacements observed at Le Saline loading experiment (Fig. 3.12a) do not allow a proper quantification of creep deformations. Here, the recorded displacements are characterized by a smooth transition between primary and secondary consolidation. In this situation a correct quantification of t_{ref} is very difficult.

At La Grisa $C_{\alpha,1}$ and $C_{\alpha,2}$ for the first loading phase of 5.6 kPa amount to 0.020 and 0.003 for the layer 1 (0-10 cm) and the layer 2 (10-40 cm), respectively, corresponding to a maximum d_s due to creep equal to 3.9 mm for C0 and 1.2 mm for C10, E10, M10. In the second loading phase, the $C_{\alpha,1}$ and $C_{\alpha,2}$ increases up to 0.026 and 0.013, corresponding to a maximum creep deformation (at the end of the loading phase) of 14.5 and 8.6 mm, for C0 and C10, respectively. Fig. 5.7 displays the comparison between displacements with and without creep effect for sensors C0 and C10 for the case of La Grisa togheter with the deformations-logarithm of time curves for both the loading phases used for the computation of C_α coefficient.

At Campalto the computation of creep has been performed only in the second loading cycle due to the very low displacements observed in the first part of the experiment. $C_{\alpha,1}$ and $C_{\alpha,2}$ coefficients for the second loading cycle amounts to 0.025 and 0.006 for layer 1 (0-10 cm) and layer 2 (10-50 cm), respectively. The estimation of C_α has been more difficult due a due to a non-distinguishable single slope of the deformation-log(time) curve. Therefore C_α values have been selected in order to have same vertical displacements at t_{ref} and at the end of the second loading phase (Fig 5.8a).

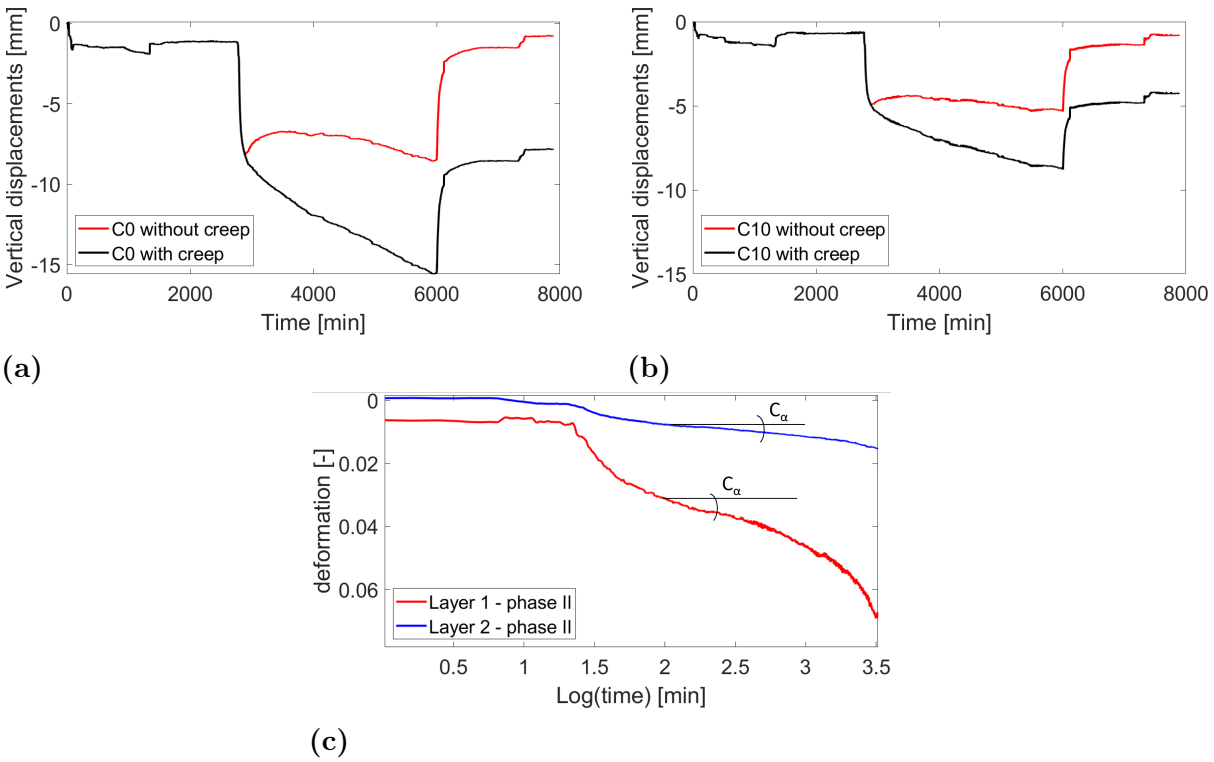

Figure 5.8: Comparison between the recorded displacements in Campalto experiment with (in black) and without (in red) the creep effect, for displacement transducers (a) C0 and (b) C10, respectively. Plots (c) and (d) shows deformations of the two considered soil layers (layer 1 is bounded by sensors C0 and C10 and layer 2 is within sensors C10 and C40) versus time in a semilogarithmic plot during the first and the second loading phase of the Campalto in-situ experiment.

6 Sensitivity analysis of the main soil parameters

Sensitivity analysis consists of understanding the effect of the different parameters on the model response. This study is performed by changing the value of the parameters one at a time and analysing the difference on the soil response. Understanding which parameters most influence the solution is essential for model calibration. In terms of model response, we are most interested in displacements and pore-water pressure evolution.

The most important parameters for the solution are:

- Hydraulic conductivity which mainly affect the value and the evolution of pore-water pressure;
- Soil stiffness in terms of Young's modulus for elastic materials and the preconsolidation stress σ_p, constitutive law parameters(a, b, c) and s which are the parameters defining the stiffness of nonlinear elasto-plastic soil layers (Section 5.3).

The influence of the most important parameters on the solution (displacements and pore-water pressure) is presented in the next subsections. However, it should be emphasized that the following sensitivity analysis has not been carried out assuming the whole domain as an homogeneous material. The model results in terms of vertical compaction and pore-water pressure have been obtained by changing the values of parameters within the different materials composing the model domain.

6.1 Hydraulic conductivity

The hydraulic conductivity k a fundamental property of porous materials in the process of soil consolidation. With small k values the overpressure generated by the load is larger and dissipates slowly causing consolidation to develop over a long time interval. Fig. 6.1 displays the modeled soil response in terms of vertical displacements and pressure for different values of hydraulic conductivity during the first phase. The load of 5.6 kPa is imposed in 15 minutes and then maintained constant. The hydraulic conductivity does not affect the maximum displacements caused by the load but rather the time needed to reach this settlement. The hydraulic conductivity is the most important parameter for the calibration of the (under)overpressure induced by loading-unloading phases. For the three

k values considered in the sensitivity the maximum overpressure is reached at the end of the loading operations (15 minutes after the beginning of the simulations) but its value is strongly dependent on this parameter. A large k results in smaller (under)overpressures and a faster dissipation. On the contrary for small permeability the pore-water pressure change induced by loading-unloading operations are high and their dissipation is slow. Pressure dissipation lasts around 4 hours for lowest value of k (red line) and about 1 hour in the other two cases for which k is 5 and 10 times larger. The obtained plots refer to the case of Campalto in the three cases and they have been obtained using the same value of k for all the materials except wood and geotexile.

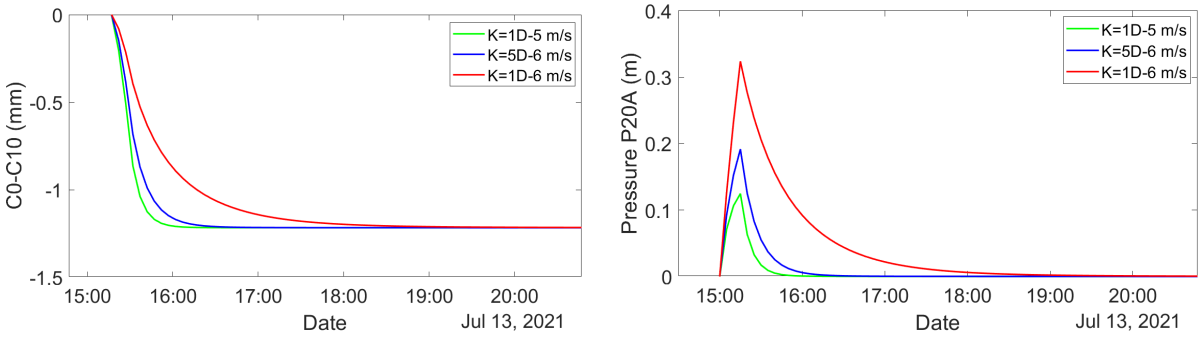

(a) **(b)**

Figure 6.1: Effect of hydraulic conductivity k, assumed to be isotropic in each later, on the model response in terms of vertical compaction below the loading area (C0-C10) of the top 10 cm of soil (a) and pore-water pressures at a depth of 20 cm (b) during the first loading phase of Campalto experiment.

6.2 Constitutive law parameters and elastic modulus

The parameters a, b, and c of the constitutive law control the stiffness of the soil when subjected to a change in effective stress (Eq 5.1). The presented refer to the La Grisa experiment. Fig. 6.2 represents the model response in term of compaction of the top 10 cm of soil (C0-C10) to the loading-unloading cycles for different values of a (first parameter of the constitutive law). According to Eq. 5.1, an increase of a produced a compressibility decrease, i.e. the soil stiffness increases, which results in a reduction of vertical displacements and compaction for the considered layer. Notice that also the amount of settlements recovered during the unloading phases decreases as well. Similar considerations can be extended to the other parameters of the constitutive law b and c recalling that an increase of b or a decrease of c results in a higher compressibility.

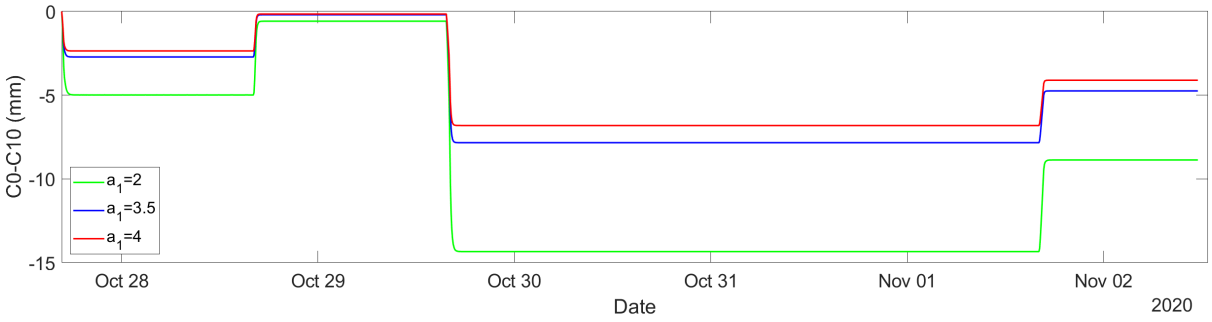

Figure 6.2: Effect of compressibility (stiffness) on the compaction of the uppermost 10 cm of soil. The plots refer to the experiment of La Grisa. The results presented in the plot have been obtained by changing the value of parameter a of the first soil layer of the model which range between depths of 0.0 and 0.12 m.

For linear elastic materials (layers of the model below a depth of 0.25 cm) the analysis is more straightforward. The soil stiffness is directly expressed as a value of the Young's modulus and it is constant during the simulation. The plots in Fig. 6.3 represents the compaction (C40) of modeled soil layers from a depth of 0.4 m to the bottom of the domain for different values of elastic modulus. The results have been obtained by fixing E equal to 0.5, 2 and 4 MPa for the linear soil layers between depths of 0.33 and 0.88 m. An increase of E results in a smaller settlement during the loading phases which are completely recovered during the unloading phases because of the materials elasticity.

In Fig. 6.3 the obtained results are consistent with the values of parameters meaning that compaction C40 increases as E increases. However, the difference between the case with $E = 2$ MPa and $E = 4$ MPa is smaller than the difference between cases with $E = 0.5$ MPa and $E = 2$ MPa even if the variation of the parameter E is similar, it increases of 2 and 1.5 MPa, respectively. This is because the simulation has not been carried out assuming the whole domain as an homogeneous material and the solution is affected the interactions between the different soil layers.

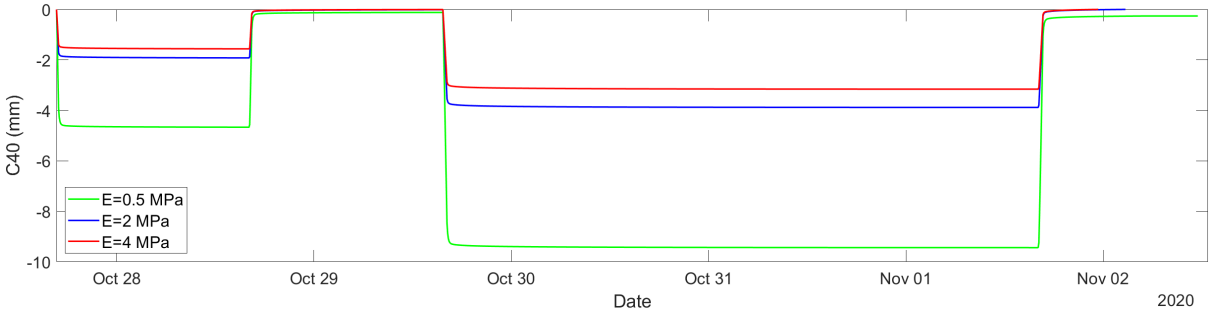

Figure 6.3: Effect of Young modulus on the compaction (C40) of soil layers from a depth of 0.4 m to the bottom of the domain for the experiment of La Grisa.

6.3 Preconsolidation stress

Preconsolidation stress is the maximum vertical effective stress the soil has ever experienced. In this model a single value of preconsolidation stress can be prescribed for all the non elastic materials, meaning that within the nonlinear soil layers, preconsolidation threshold is overcome in different instants because of the load propagation in depth and the different initial stress distribution in the domain ($\sigma_{z0} = \gamma_s z$). As explained in Section 5.4, according to its value, the model compute the compressibility in two different ways to account for the plastic behavior and mechanical hysteresis of marsh soils. When the soil is loaded the vertical effective stress increases and if its value overcomes the preconsolidation stress, soil behavior becomes plastic and characterized by a larger compressibility.

A larger preconsolidation stress yields a soil that behaves elastically for a larger interval of σ_z. By choosing a σ_p value close to the maximum effective stress originated by the loading phases, the displacements during the loading phases are smaller and a larger percentage is recovered when the load is removed. Indeed, as explained in Section 5.4, if the preconsolidation value is not overtaken by the maximum effective stress induced by the load, the compressibility of the soil during the loading phase will be equal to the compressibility during the unloading phase.

Fig. 6.4 shows the compaction of the shallowest 0.1 m of soil, for the model of La Grisa experiment, for the case with $\sigma_p = 8$ kPa which is greater than 5.6 kPa, i.e the applied load in the first phase, and close to 11.3 kPa, i.e. the applied load intensity during the second phase. At the end of the first loading-unloading cycle all the deformation is fully recovered and a small permanent settlement is computed after the second phase (load intensity of 11 kPa$>$ 8 kPa). It should also be noted that, the load is applied on the surface and consquently the resulting effective stress experienced by the soil is lower than the load itself. If the model is run with $\sigma_p = 2$ kPa, which is much smaller than the effective stress induced into the soil by both the two loading phases, much permanent deformation remains at the end of both the recovery phases (Fig. 6.4). For an intermediate value of the preconsolidation stress ($\sigma_p = 4$ kPa) plastic deformation are observed only for the second loading phase (Fig. 6.4).

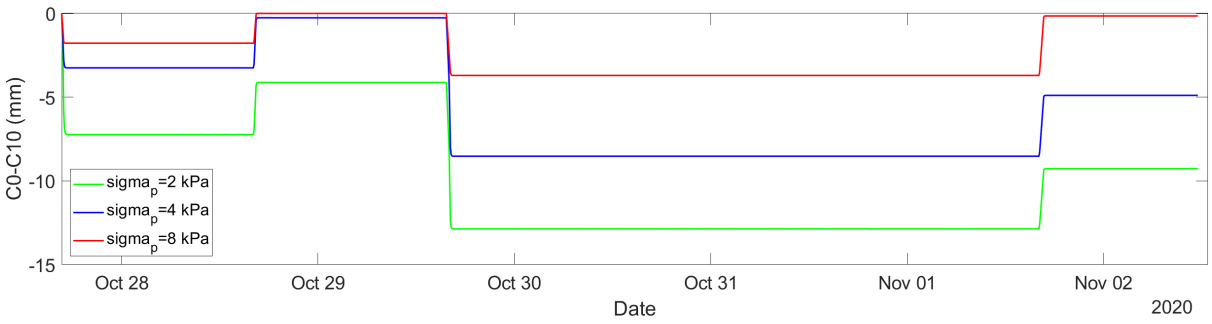

Figure 6.4: Effect of preconsolidation stress on the compaction of the shallowest 0.1 m of soil (C0-C10), expressed in millimeters for the model of La Grisa experiment.

6.4 Parameter s

The s parameter expresses the ratio at the inversion point (switch from loading to unloading conditions) between the compressibility in loading and unloading phases (Eq. 5.3). The plots in Fig. 6.5 has been obtaining running the model of Le Saline experiment fixing the value of s of the first soil layer (depth between 0 and 0.1 m) to 4 and 10. The vertical compaction of the top 0.1 m of soil (C0-C10) is reported in millimeters. The larger the value of s, the greater the difference between the two compressibilities and consequently, the smaller the amount of vertical settlement recovered when the load is removed.

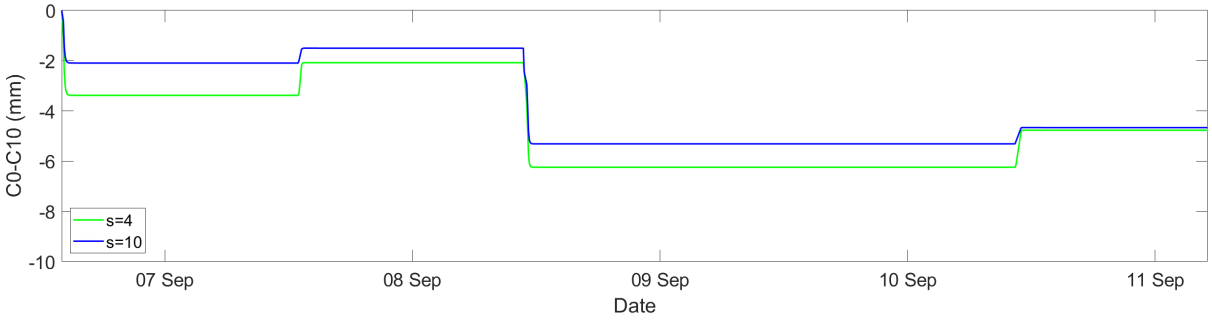

Figure 6.5: Effect of the parameter s on the compaction of the shallowest 0.1 m of soil (C0-C10) in the model of the Le Saline experiment.

7 Model results

Once a set of parameters is selected for each layer of the 3D mesh the simulation described in Section 5 solves the coupled flow and equilibrium equations and provides the distribution of many variables within the whole domain for each time step of the simulation: the displacements along the 3 directions x, y, z, variation of pore-water pressures, effective stress and water flux. The selected time step in the three simulations of La Grisa, Campalto and Saline experiments is 300 s, constituting a good compromise between results accuracy and computational time. Figures 7.1 and 7.2 display an example of model output in terms of vertical displacements and pore-water pressure on a vertical section of the domain in the middle of the loading area, in correspondence of the second loading phase obtained by modeling the La Grisa in-situ experiment.

The most interesting physical variables are the pore-water pressure variation computed at element level and the displacements along the vertical direction calculated on each domain node. These quantities can be compared with the observations recorded during the in-situ experiments by the pressure and displacements transducers. To compare the modeled and measured pressures, the latter has been converted from MPa to water level, expressed in m, and it is increased of a quantity equal to the depth of the pressure transducer considered. For the displacements the comparison has been performed considering the soil compaction of three soil layers: the shallow layer within displacements transducers C0 and C10 (depth between 0 and 0.1 m) , the intermediate layer bounded by displacements transducers C10 and C50, C40 for La Grisa (depth between 0.1 and 0.5 m, 0.4 for La Grisa) and the deep layer below C50 (C40 for La Grisa). The compaction is computed as the difference between the vertical displacements obtained by the model at the soil surface and at a depth of 0.1 m for the shallow layer, and between 0.1 m and at a depth of 0.5 m (0.4 m for La Grisa) for the intermediate layer. The compaction of the deep layer is given by the vertical displacements at 0.5 m (0.4 m for La Grisa).

The comparison between model output and recorded data in terms of soil compaction and pore-water pressure for the three modeled sites are presented in the next sections along with the stratigraphy used in the model and the set of parameters for each layer used in the simulations as obtained by a trial-and-error calibration procedure.

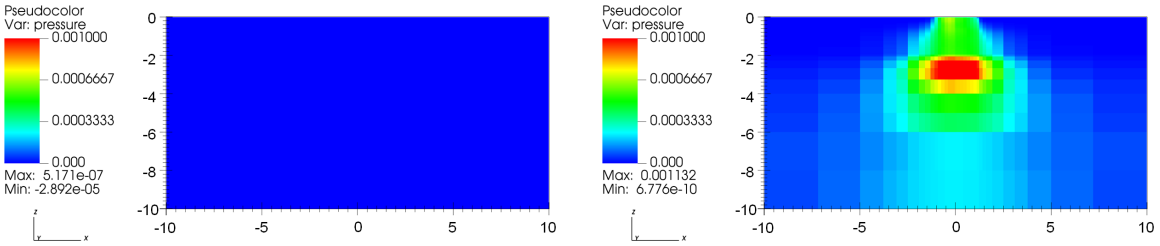

(a) t=0 s beginning of the loading phase

(d) t=1800 s end of the loading phase.

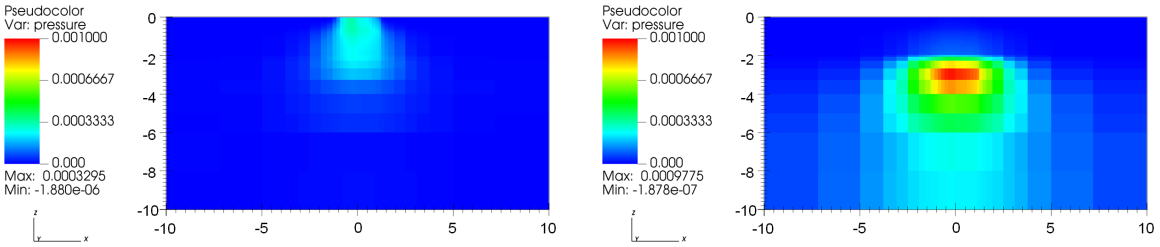

(b) t=300 s

(e) t=2700 s constant load

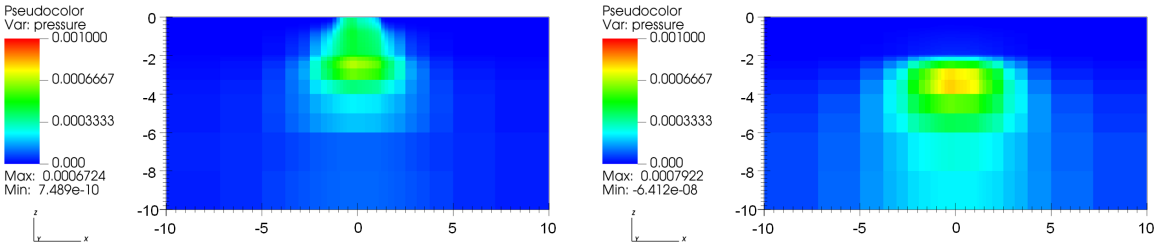

(c) t=900 s half of the loading phase

(f) t=3600 s constant load

Figure 7.1: Variation of pore-water pressure, in MPa, over time, during the second loading phase of 11.3 kPa at La Grisa along a vertical section parallel to the y-axis in the middle of the loading area. (a) At the beginning of the loading phase pressure is null. During a loading phase the overpressure increases near to the surface (b), (c), consistently with the load up to its maximum (d) in correspondence of the end of the pumping procedure (t = 1800 s). When the load remains constant (after t = 1800 s) overpressure dissipates (e), (f). Similar considerations can be derived for the unloading procedure during which, underpressures are obtained due to the load removal.

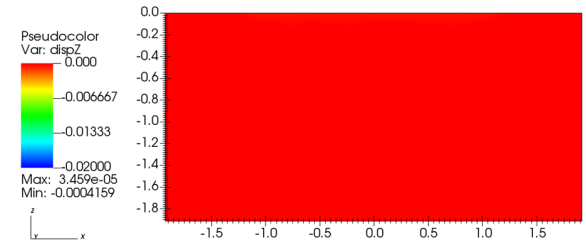

(a) t=0 s beginning of the loading phase

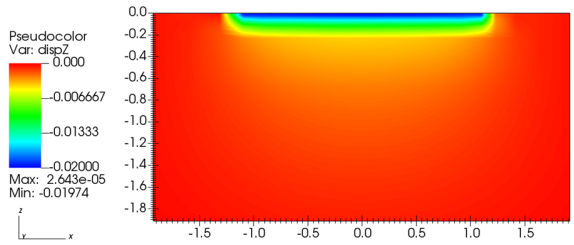

(d) t=1800 s end of the loading phase.

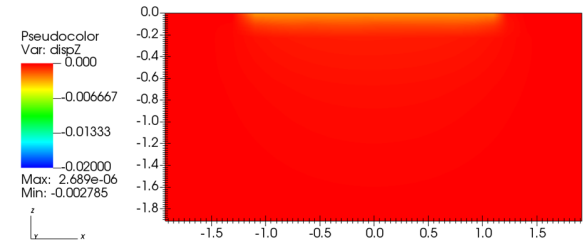

(b) t=300 s

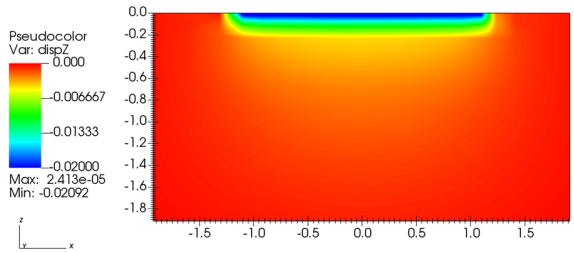

(e) t=2700 s constant load

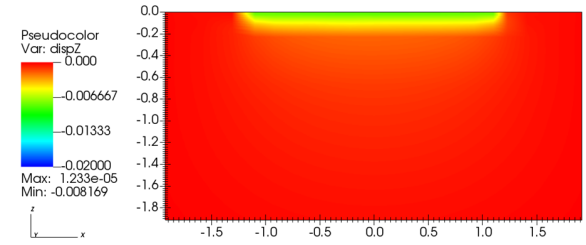

(c) t=900 s half of the loading phase

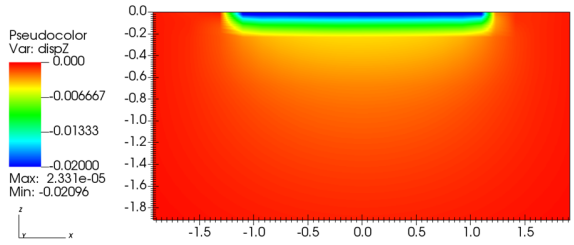

(f) t=3600 s constant load

Figure 7.2: Vertical displacements, in m, over time, during the second loading phase of 11.3 kPa at La Grisa along a vertical section parallel the y-axis in the middle of the loading area. The upper 2 m of the domain are shown, only. The load does not produce any displacement below a depth of 2 m. Vertical displacements increase as the load increases ($0 - 1800$ s), when external forcing is constant displacements increases more due to primary consolidation process (pore pressure dissipation) until the overpressure is completely dissipated. Then, the displacements remain constant.

7.1 La Grisa

The choice of layering to be used in the model of La Grisa in-situ experiment has been taken considering the results of the stratigraphic analysis described in the Section 2. The 3D mesh is composed by 12 materials of which only the two most superficial soil layers (depth ranging from 0 to 0.23 m), represented in red and green in Fig. 7.3, are modeled with an elasto-plastic relationship. The superficial elements corresponding to the wooden pallets and geotexile are represented in yellow and blue respectively, the remaining colors represent the other soil layers modeled as linear elastic materials. Each material is characterized by different hydraulic and geomechanical properties as discussed is Section 5.3.

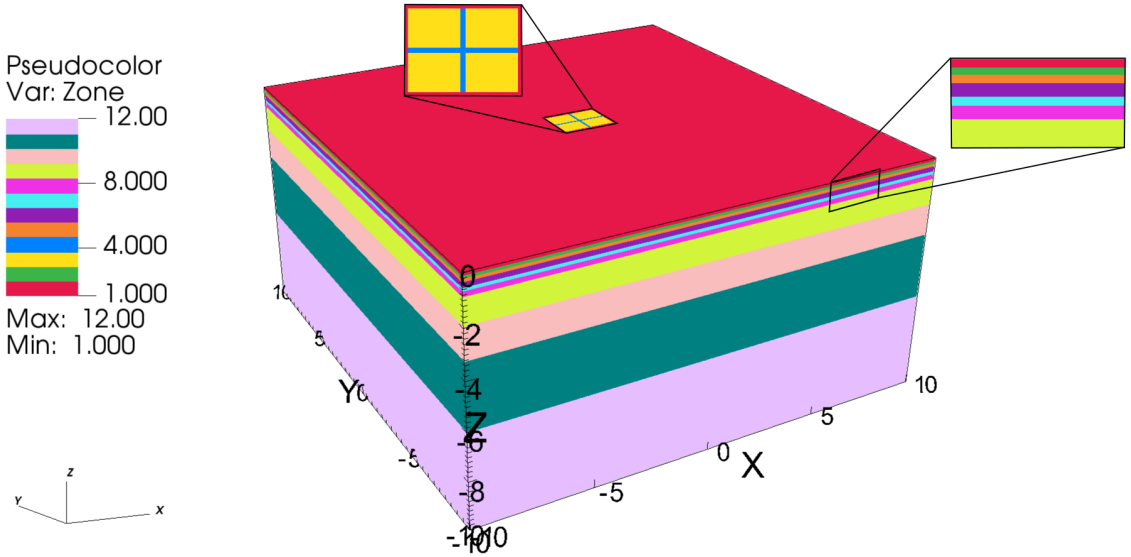

Figure 7.3: Model layering at La Grisa. The variable zone indicates the different materials. Materials 1 and 2 are modeled as nonlinear soil layers, materials 3 and 4 are the wooden pallets and the geotexile respectively and the remaining zones (5-12) constitute the linear elastic soil layers.

The calibration allows to select the set of parameters that allows the best representation of the measured data. Table 7.1 summarizes the optimal set of the main parameters used for the simulation. Poisson's ratio ν is set to 0.2 for the soil layers and to 0.15 for the wooden pallets and the geotexile. The porosity is fixed to 0.44 in the whole domain. Preconsolidation stress is set to 4 kPa for all the domain, which is lower than the applied load in the two phases.

The E values of the linear elastic layers equals 2 MPa for the intermediate layers depth

Material	Depth (m)	k (m/s)	E (MPa)	Constitutive law	s (-)	ν
1. Organic	0-0.12	$2.5 \cdot 10^{-4}$	/	$\frac{1}{C_m} = 3(\sigma_z)^{0.81}$	3.0	0.20
2. Organic	0.12-0.23	$2.5 \cdot 10^{-4}$	/	$\frac{1}{C_m} = 6(\sigma_z)^{0.81}$	2.0	0.20
3. Wood	0-0.01	$5.0 \cdot 10^{-8}$	10^4	/	/	0.15
4. Geotexile	0-0.01	$5.0 \cdot 10^{-8}$	10^4	/	/	0.15
5. Peaty sand	0.23-0.33	$2.0 \cdot 10^{-5}$	2.0	/	/	0.20
6. Sand	0.33-0.55	$2.0 \cdot 10^{-5}$	2.0	/	/	0.20
7. Silty clay	0.55-0.68	$8.0 \cdot 10^{-6}$	2.0	/	/	0.20
8. Silty clay	0.68-0.88	$8.0 \cdot 10^{-6}$	3.0	/	/	0.20
9. Sandy silt	0.88-1.96	$1.0 \cdot 10^{-5}$	4.0	/	/	0.20
10. Peat	1.96-3.26	$2.0 \cdot 10^{-7}$	8.0	/	/	0.20
11. Sandy silt	3.26-6	$1.0 \cdot 10^{-7}$	12.0	/	/	0.20
12. Consolidated	6-10	$1.0 \cdot 10^{-7}$	20.0	/	/	0.20

Table 7.1: Calibrated set of parameters for the La Grisa model.

(0.23-0.68 m). The soil stiffness of the deeper layers (0.68-10 m) has been assumed to increase with depth (Tab. 7.1). Because no displacement records are available below 0.4 m, and the load effect becomes negligible as the depth increases, values from literature have been used [15], [29]. The evolution of E in the middle of the two nonlinear soil layers below the center of the loading area is depicted in Fig. 7.4. The soil stiffness of the second soil layer is about twice that of the first layer. The stiffness of the two most superficial layers is about one order of magnitude smaller than that of the intermediate underlying soil layers.

The soil hydraulic conductivity ranges from 10^{-7} to 10^{-4} m/s and decreases with depth. The two upper layers are one order of magnitude more permeable than the underlying soil.

7.1.1 Compaction

The behaviour of the soil responding to the application of the load, as provided by the model, has been compared with the measured data collected during the in-situ experiment. The comparison has been performed considering the compaction of the shallow (C0-C10),

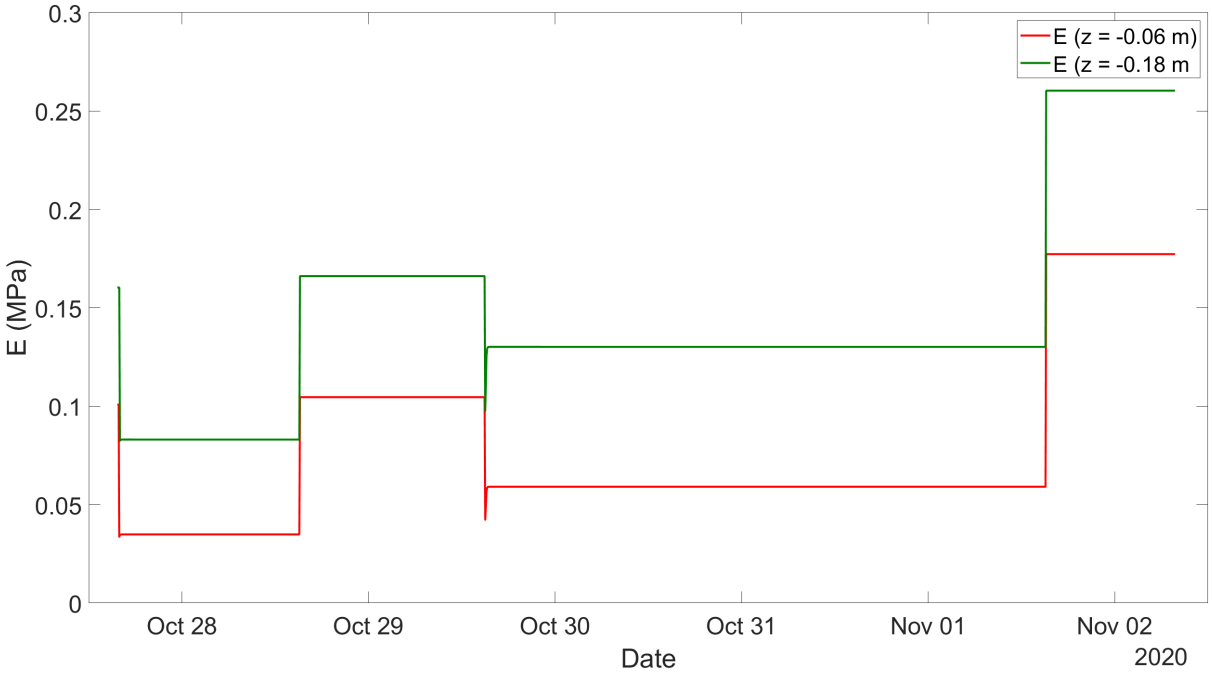

Figure 7.4: Evolution versus time of E in two points located in the middle of the two nonlinear soil layers (depths 0.06 and 0.18 m) below the center of the loading area during the two loading-unloading cycles at the La Grisa experiment. This evolution reflects the case (c) in Fig. 5.5.

intermediate (C10-C40) and deep (C40) soil layers below the center of the loading area:

- compaction C0-C10 is obtained as the difference between the vertical displacements on the soil surface and at a depth of 0.1 m (10 cm) in the center of the loading area ;
- compaction C10-C40 is obtained as the difference between the vertical displacements at 0.1 m below the soil surface and at a depth of 0.4 m (10 cm) in the center of the loading area;
- compaction C40 of the soil layers below a depth of 0.4 m is expressed by the vertical displacement at a depth of 0.4 m in the center of the loading area.

In Fig. 7.5, the modeled compaction are compared with the measured compaction, obtained by the records of the displacement transducers C0, C10 and C40, cleaned by the creep deformations (Section 5.5). The recorded data and the model output are shown by a black and red profile, respectively. Notice that sensor C40 belongs to the sixth material, while C0 and C10 are placed in the most superficial soil layer.

The heterogeneity of the soil features has been satisfactorily represented, since both the computed superficial (C0-C10) and the intermediate (C10-C40) soil compaction reproduces

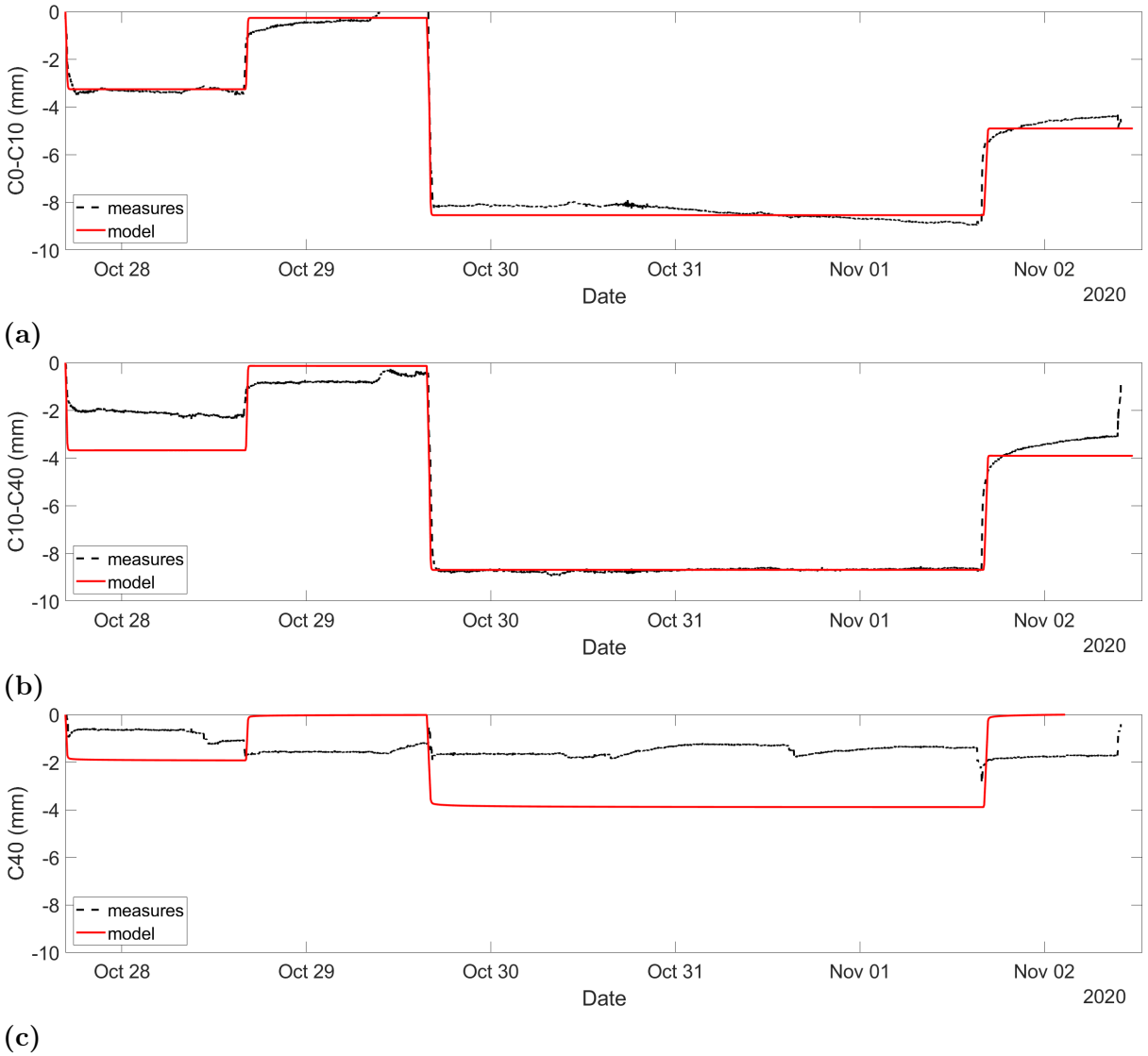

Figure 7.5: Vertical compaction of shallow (C0-C10), intermediate (C10-C40) and deep (C40) soil layers, underneath the center of the loading area during both phases of the La Grisa experiment. In black the recorded data cleaned by the effect of the creep deformations, in red the model output.

satisfactorily the recorded data. The selected plastic constitutive law implemented in the two most superficial layers allows to match very well the measured compaction (C0-C10) in both the loading phases (Fig. 7.5a). The model overestimate of 2 mm the compaction of the intermediate layer (C10-C40) during the first loading phase (Fig. 7.5b). A possible explanation is that a single value of preconsolidation stress for all the domain, as it is allowed by the available release of the simulation, is not sufficient to adequately represent the compaction behavior of soil layers located at different depths and characterized by different initial degrees of consolidation. Notice also that soil layers below 0.23 m depth are described using a linear elastic constitutive law. The model overestimates by a factor 2 the compaction of the deep layers (C40), characterized by zero recovery in both unloading phases, suggesting that a linear elastic constitutive relationship is likely too simple to capture this soil behavior (Fig. 7.5c).

7.1.2 Pore-water pressure changes

The five pressure transducers (P25A, P25B, P50A, P50B, P100) placed along the portion of the soil between the two lines of tanks at different depths (Fig. 3.5) recorded the groundwater pressure. The model used in this study computes, instead, the variation of the pore-water with respect to an initial condition. This means that the model provides the (over)underpressure produced by loading-unloading cycles, in the hypothesis of saturated porous medium and initial hydrostatic pressure. Water level evolution during the test is strongly affected by the tide (Fig. 3.5). The peaks of pore-water pressure observed when the load is constant are caused exclusively by tidal oscillations. During high tide conditions, when the marshland is submerged the pore-water pressure follows the tidal level. Consequently, pressure evolution are more challenging to be interpreted than the displacements as the pressure in the porous matrix depends on the imposed load and on the tide. If the loading-unloading operations take place during high or low tide conditions it is difficult to distinguish the two contributions.

Therefore, the model has been calibrated to match the measured (under)overpressures during the load produced only by the load. As expected in correspondence of loading-unloading operations the simulation provides overpressures during the two loading phases and underpressure when the soil is unloaded (Fig 7.6). For the pressure transducer P50A, no variation of pore-water pressure have been recorded during the experiment since it is

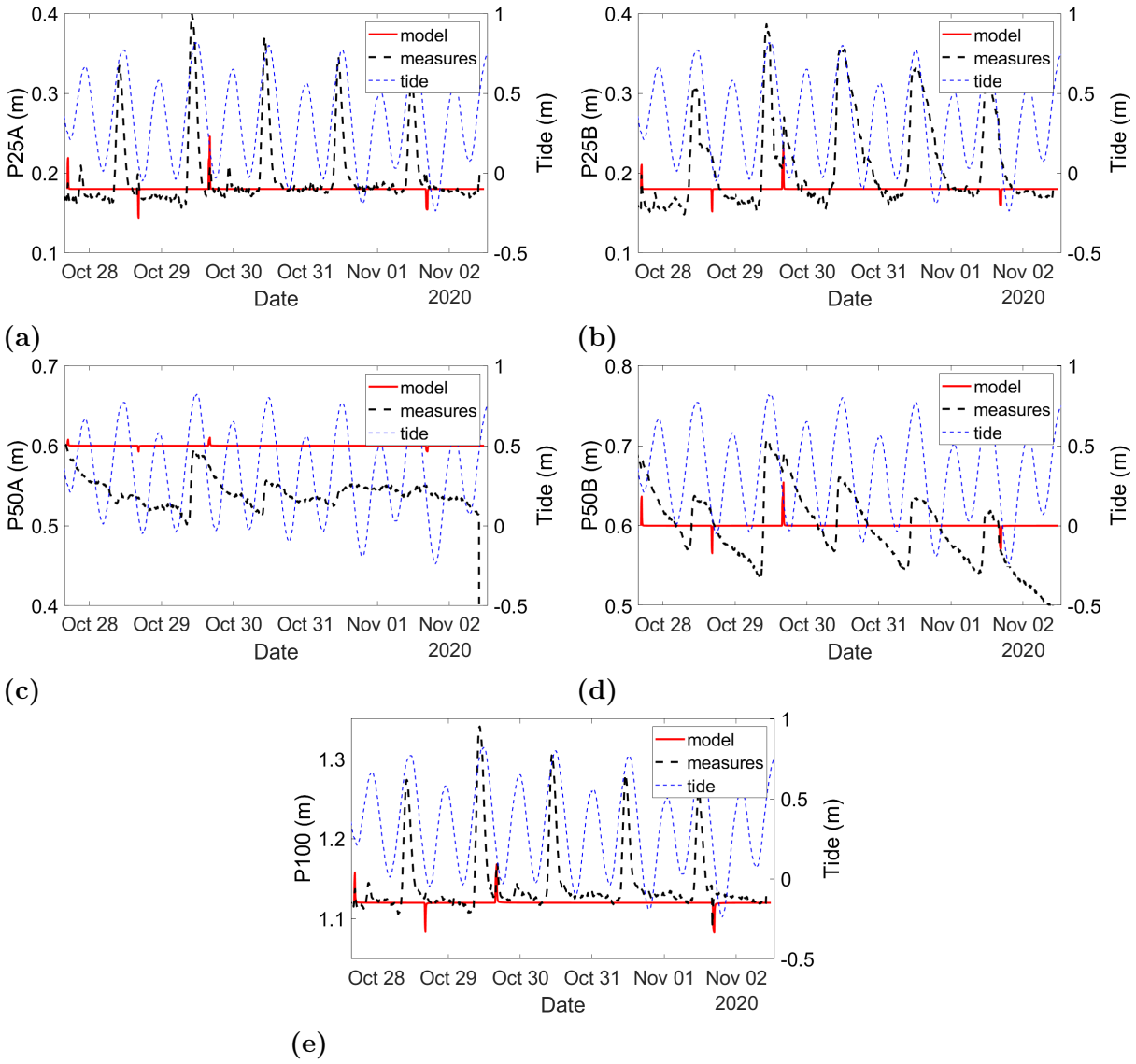

Figure 7.6: Pore-water pressure (left axis) in m during the La Grisa experiment for each pressure transducer (P25A, P25B, P50A, P50B, P100) plotted with the tidal fluctuations (right axis) for a better interpretation of the results shown using a red curve

located far from the loading area (Fig. 3.3). Also the (over)underpressures simulated by the model are basically null. Overall, the model simulates well the overpressures produced by the load during the second loading phase (started at 15:49 of October 29) of the in-situ experiment (Figures 7.7a and 7.8b). On the other side, the model overestimates of few centimeters the measured underpressures produced during the emptying of the tanks (unloading phases), except for P100 (Fig. 7.7b) for which the second unloading phase is well represented by the simulation. The model overestimates of few centimeters the measured overpressures during the first loading phase (16:30 of October 27) for all the pressure transducers. For example, the overestimation for sensor P25A amount to 3 cm

(Fig. 7.8a). Regarding the water dynamics, the dissipation rate of the pore-water pressure simulate well the observations during the first loading phase (Fig. 7.8a) while it is gently overestimated during the second loading-unloading phase (Figures 7.7a, 7.8b and 7.7b). However, a smaller k value, which would allow to match the dissipation rate, results in (over)underpressures much higher than the records (see Section 6).

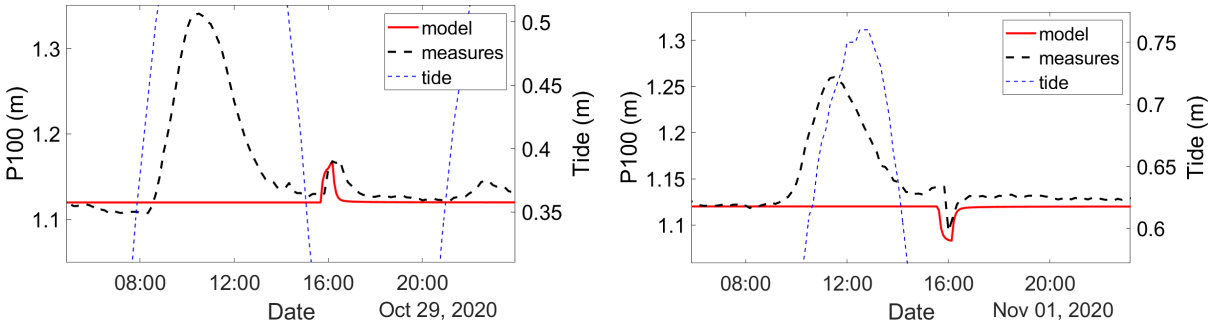

(a) **(b)**

Figure 7.7: Pore-water pressure evolution (left axis), during the second tank (a) filling and (b) emptying operations during the Grisa experiment for the pressure traducer P100 plotted with the tidal fluctuations (right axis).

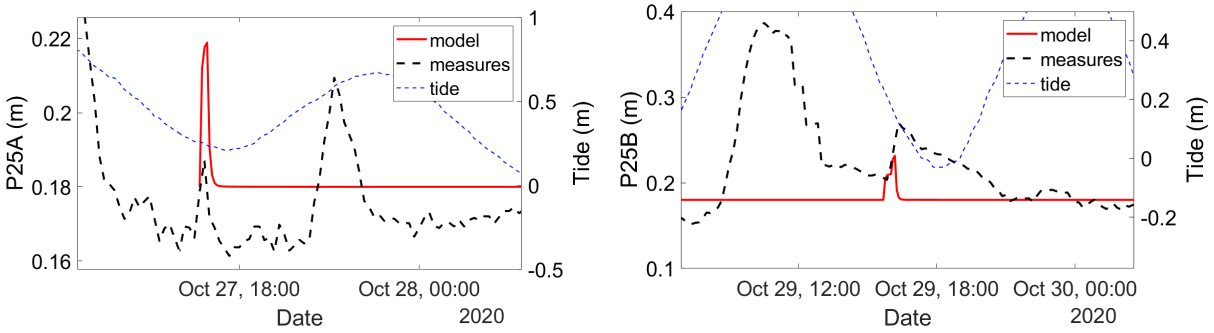

(a) **(b)**

Figure 7.8: (a) Pore-water pressure evolution (left axis), during the first tank filling for pressure transducers P25A. (b) Pore-water pressure evolution (left axis), during the second tank filling for pressure transducers P25B.

7.2 Campalto

The layering used to represent the Campalto in-situ experiment is composed of 8 materials, with the two most superficial soil layers (depth ranging from 0 to 0.3 m) that are modeled as elasto-plastic materials (Fig. 7.9). The superficial elements corresponding to the wooden pallets and geotexile (represented in yellow and blue, respectively) and the other soil layers are modeled as linear elastic materials. Table 7.2 summarizes the optimal set of the

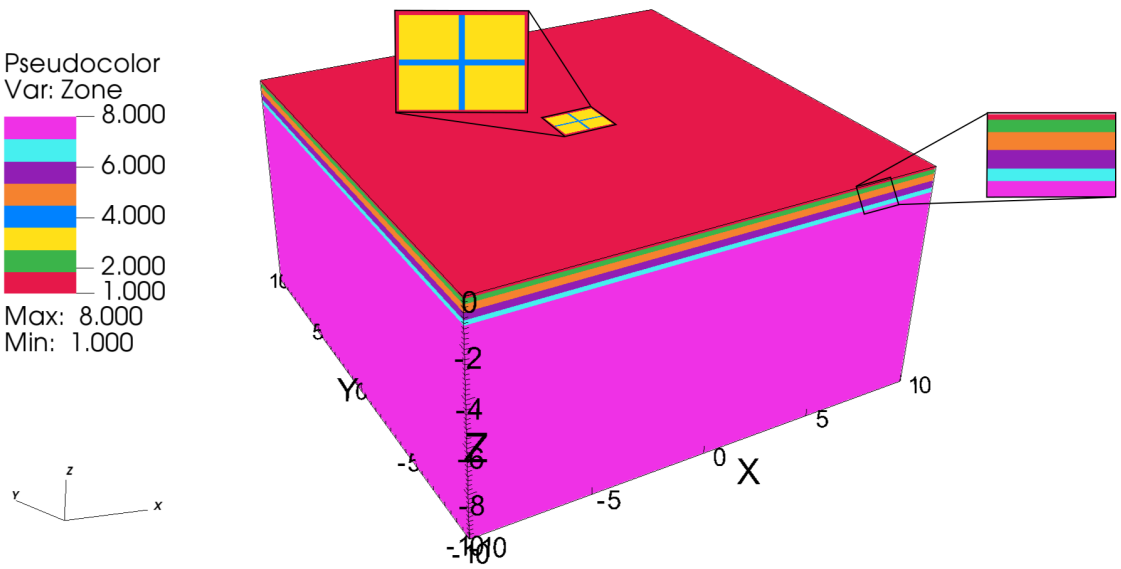

Figure 7.9: Definition of model layering at Campalto.

main parameters as obtained by the model calibration and the thickness of the various soil layers. Poisson's ratio ν is set to 0.2 for the soil layers and to 0.15 for the wooden pallets and the geotexile. The porosity is fixed to 0.44 in the whole domain. Preconsolidation stress is set to 8 kPa for all the domain.

The E of the linear elastic layers equals 3-4 MPa for the intermediate layers (depth 0.30-1.10 m) and picks to 20 MPa for the more consolidated material. In nonlinear soil layers (materials 1 and 2), the evolution of E in the middle of the two nonlinear soil layers below the center of the loading area is depicted in Fig. 7.10. In the first loading phase, the soil stiffness remain constant since the effective stress does not overcome the preconsolidation threshold (the applied load of 5.6 kPa is lower than the initial σ_p). The soil stiffness of the second soil layer is larger than of the one of the first layer. The stiffness of the two most superficial layers results about one order of magnitude smaller than that of the underlying soil layers.

As concern the hydraulic conductivity, its distribution in the domain differs from the case of La Grisa to match the records of pore-water pressure obtained during the in-situ loading experiment. The intermediate soil layers with depths from 0.3 to 1.1 m must be more permeable than the two shallowest materials.

Material	Depth (m)	k (m/s)	E (MPa)	Constitutive law	s (-)	ν
1. Silty clay (organic)	0-0.10	$1.0 \cdot 10^{-6}$	/	$\frac{1}{C_m} = 8(\sigma_z)^{1.6} + 0.1$	2.7	0.20
2. Silty clay (organic)	0.10-0.30	$1.0 \cdot 10^{-6}$	/	$\frac{1}{C_m} = 25(\sigma_z)^{1.6} + 0.35$	1.8	0.20
3. Wood	0-0.01	$5.0 \cdot 10^{-8}$	10^4	/	/	0.15
4. Geotexile	0-0.01	$5.0 \cdot 10^{-8}$	10^4	/	/	0.15
5. Clay	0.30-0.60	$7.0 \cdot 10^{-5}$	3.0	/	/	0.20
6. Silty clay	0.60-0.90	$7.0 \cdot 10^{-5}$	4.0	/	/	0.20
7. Clayey silt	0.90-1.10	$7.0 \cdot 10^{-5}$	4.0	/	/	0.20
8. Consolidated	1.10-10.0	$1.0 \cdot 10^{-7}$	20.0	/	/	0.20

Table 7.2: Calibrated set of parameters for the Campalto model.

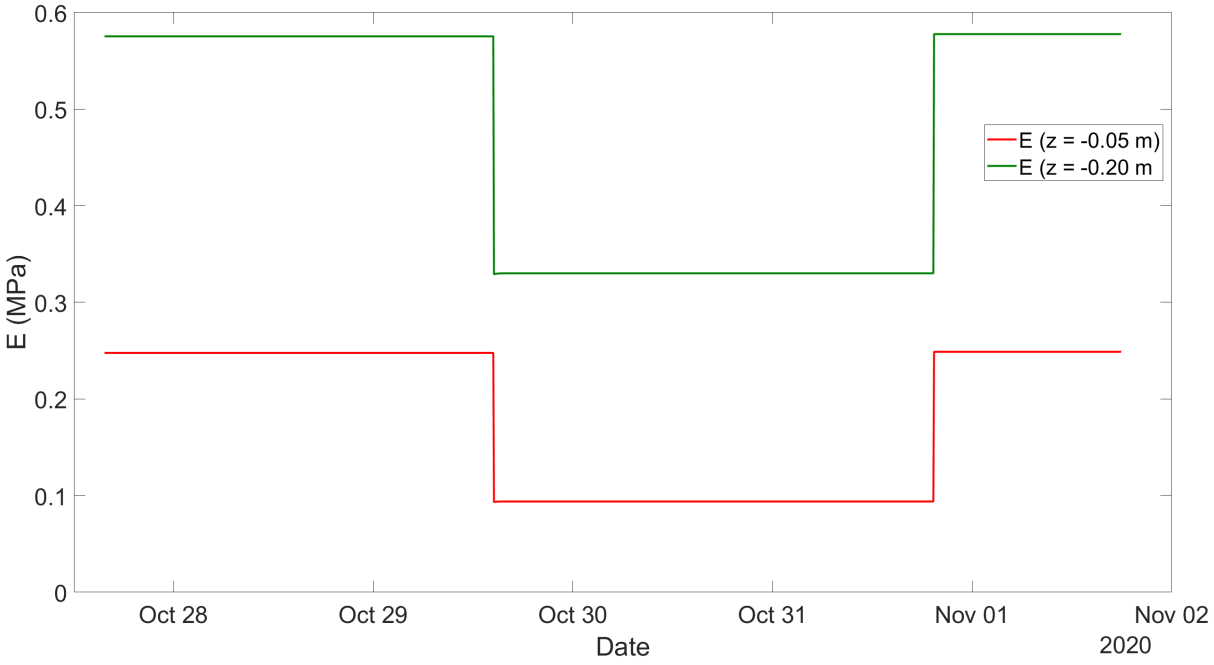

Figure 7.10: Evolution versus time of E in two points located in the middle of the two nonlinear soil layers (depths 0.05 and 0.20 m) below the center of the loading area during the two loading-unloading cycles of the Campalto experiment. This evolution reflects the cases (b) and (c) of Fig. 5.5, during the first and in the second loading phase, respectively.

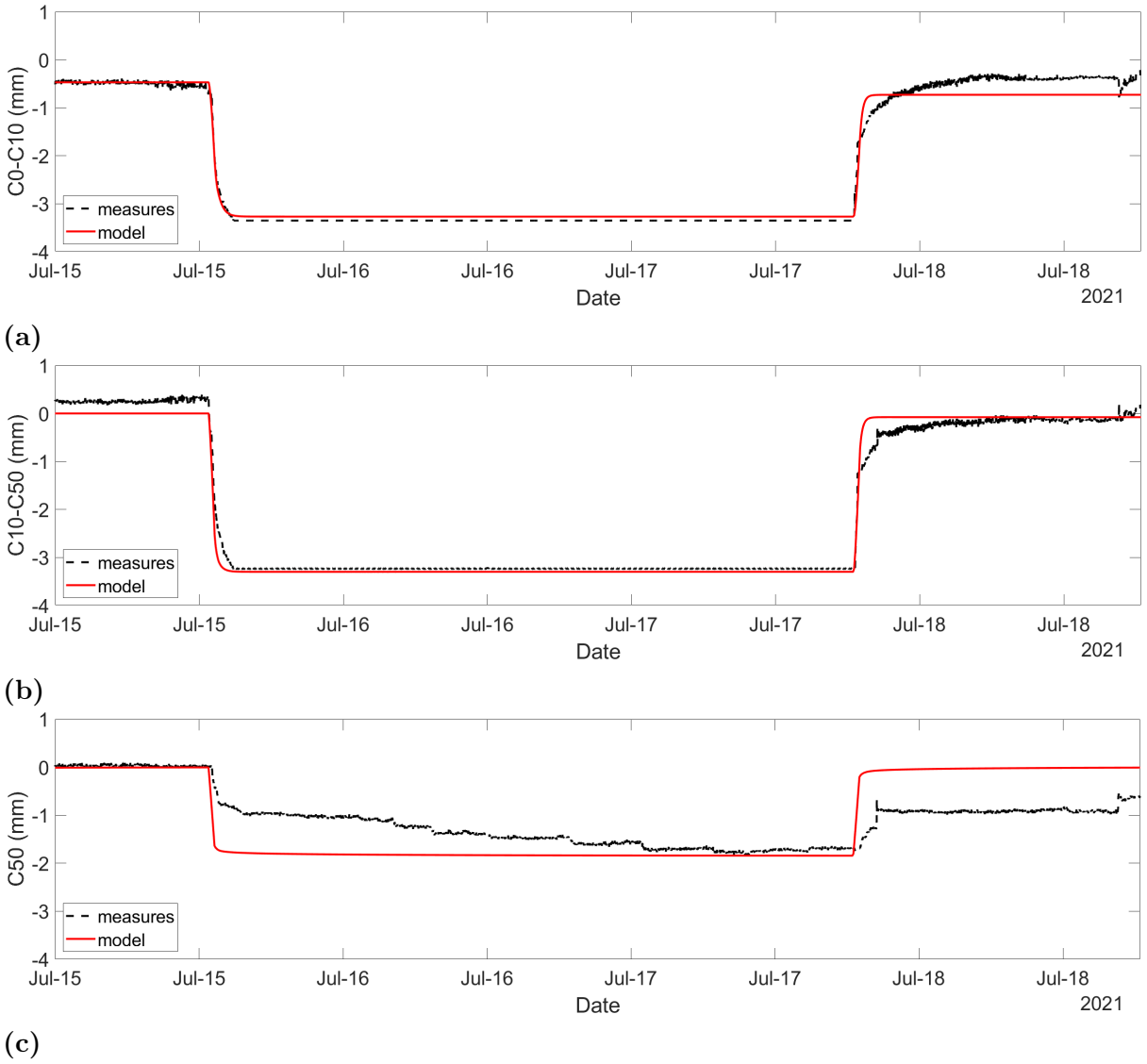

Figure 7.11: Compaction of shallow (C0-C10), intermediate (C10-C40) and deep (C40) soil layers, underneath the center of the loading area during the second loading phase of the Campalto experiment. In black the recorded data cleaned by the effect of the creep deformation, in red the model output.

7.2.1 Compaction

As in the previous case, the compaction of the shallow (C0-C10), intermediate (C10-C40) and deep (C50) soil layers obatined by the model has been compared with the measured compaction computed from the records of the displacement transducers C0, C10, C50, positioned in the center of the loading area during the Campalto experiment, and properly cleaned by the creep deformations (Section 5.5). The recorded data and the model outputs are plotted in Fig. 7.11 by a black and red profile, respectively. In this experiment, the calibration has been performed on the second loading phase only because during the first

loading phase the displacements transducers recorded an expansion in the layer C10-C50, with the displacements measured at 0.5 m depth (sensor C50) larger than those at 0.1 m depth (sensor C10).

The results show that the model is able to reproduce quite well the soil compaction of the three monitored soil layers. The high value of $\sigma_p = 8$ kPa close to the the maximum load applied during the second loading phase, which is equal to 11.3 kPa, allows to reproduce the almost elastic soil behavior as observed by the transducers. Excluding creep deformations, all vertical displacements recovers during the unloading phase. The linear elastic constitutive law implemented for the deeper soil layers yields to overestimate by a factor of 2 the rebound at the end of the second loading phase for C50 (Fig. 7.11c).

7.2.2 Pore-water pressure changes

The data recorded by the six pressure transducers (Fig. 3.9), deployed at different depths and positions (Fig. 3.7), during the in-situ experiment at Campalto have been compared with the pore-water pressure evolution simulated by the model. As in the previous case, to compare the two data sets, the recorded data form the six pressure transducers have been converted into water level and the modeled pressure variation over time is converted into water level and increased of a quantity proportional to the depth of the sensor.

Fig. 7.12 shows the comparison between the model outputs and the records for the six pressure transducers. The most important model parameter for the calibration of the pressure variation during the loading-unloading cycles is the hydraulic conductivity. Looking at the measures, it is evident that the pore-water pressure variation is larger in the shallow soil (P25A, P25B) than in the intermediate (P50B) and deep soil (P100A, P100B). To model this behavior k is assumed to be slightly smaller in the two shallowest layers, whose depths ranges from 0 to 0.3 m, than the one of the intermediate soil layers (depth between 0.3 and 1.1 m) .

The comparison between model output and records is very challenging (Fig. 7.12) because during the first cycle the tank filling (14:47 of July 13) and emptying (15:00 of July 14) operations have been conducted in correspondence of a tidal peak. The same condition occured during the second soil unloading (18:40 of July 17). The only case when the pore-water pressure change due to loading is more easily recognizable correspond to the

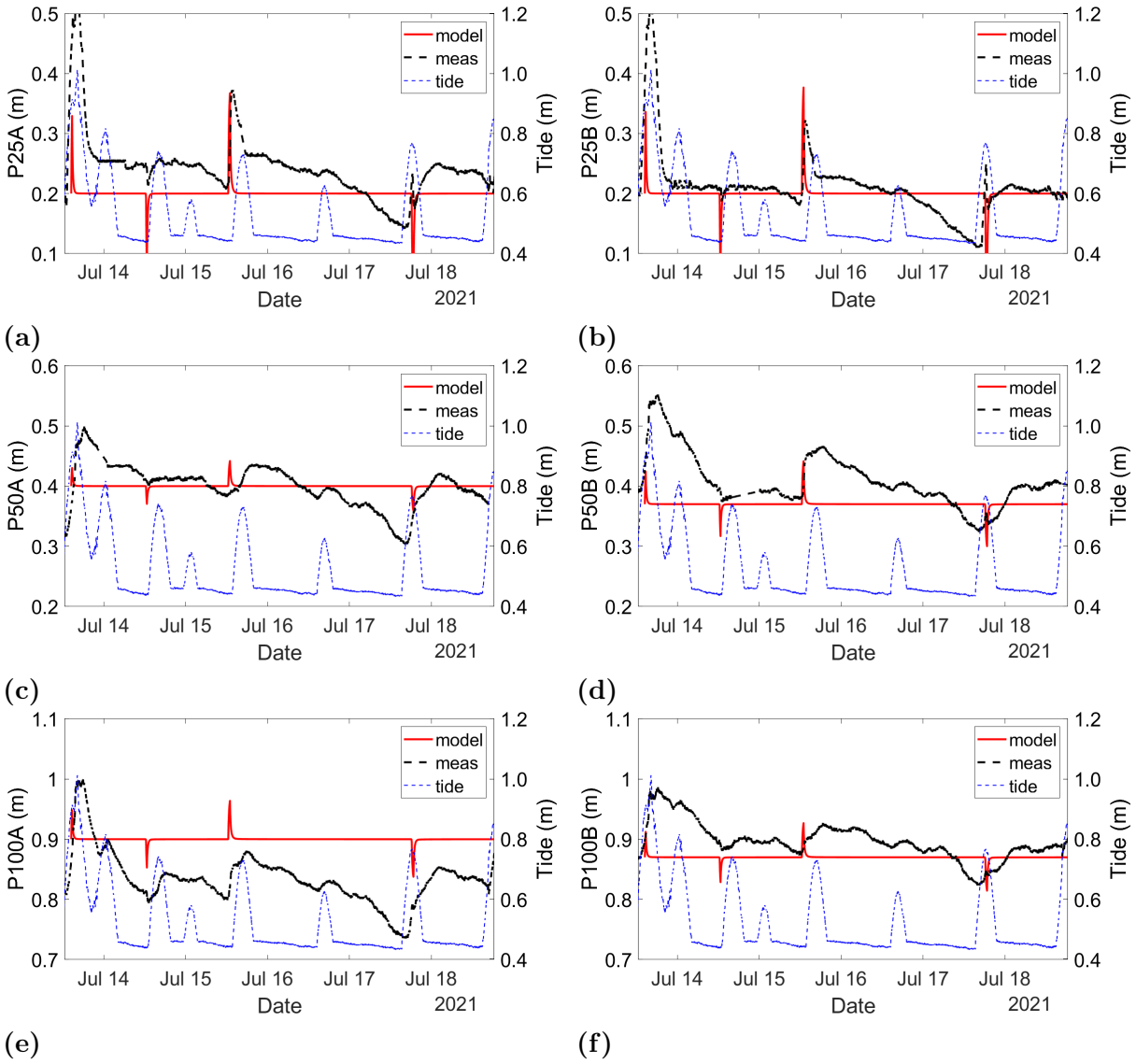

Figure 7.12: Pore-water pressure evolution (left axis) during the Campalto experiment for each pressure transducer (P25A, P25B, P50A, P50B, P100A, P100B) plotted with the tidal fluctuations (right axis) for a better interpretation of the results shown usign a red line.

second loading phase (12:40 of July 15). Consequently, the calibration has been focused on the second loading phase.

In Fig. 7.13 the comparison of recorded data and the simulated pore-water pressure during the second loading phase is represented. In this part of the simulation, the model mimics satisfactorily the recorded pressure trend, expecially for sensors P25A and P25B. The peak of overpressure and the left part of the curve are well captured by the model. The model overestimates the velocity with which the excess of pore-water pressure is dissipated. The increase of tidal level observed immediately after the loading phase may have slowed the

pore-water pressure dissipation. Fig. 7.14 shows the comparison of recorded data and the simulated pore-water pressure during the second unloading phase for sensors P25A and P25B. During the unloading phase the model overestimates by 0.1 m the underpressures. Probably the measured underpressures would have been higher (in modulus) without the influence of the tidal peak. The pore-water underpressure dissipation rate is overestimated due to tidal effect too. It is interesting to notice that the tanks are emptied simply by opening some caps located at the bottom of the tanks, meaning that the water falls on the ground surface. This water that infiltrate into the soil may interfere with the pore-water pressure dissipation.

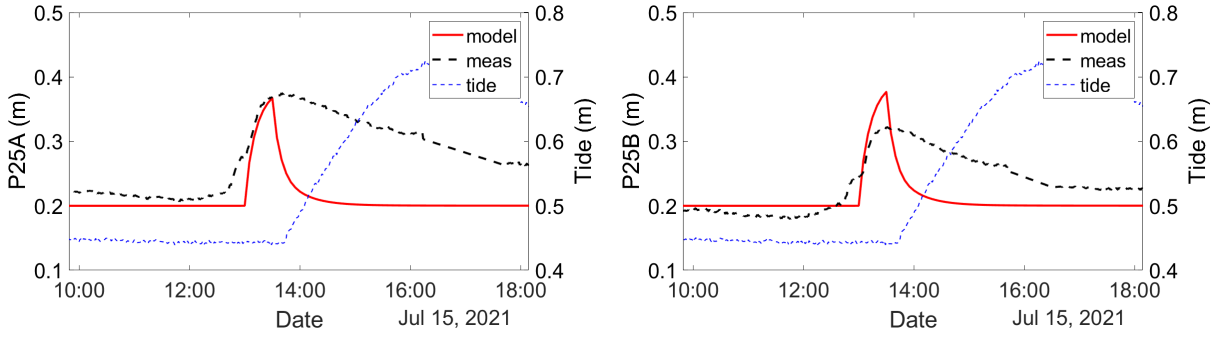

(a) **(b)**

Figure 7.13: Pore-water pressure evolution (left axis), during the second tank filling operation, expressed as water level in m during the Campalto experiment the pressure transducer P25A (a) and P25B (b) plotted with the tidal fluctuations (right axis). Model results are expressed in red, measures with a dashed red line and the tide with a dashed blue line.

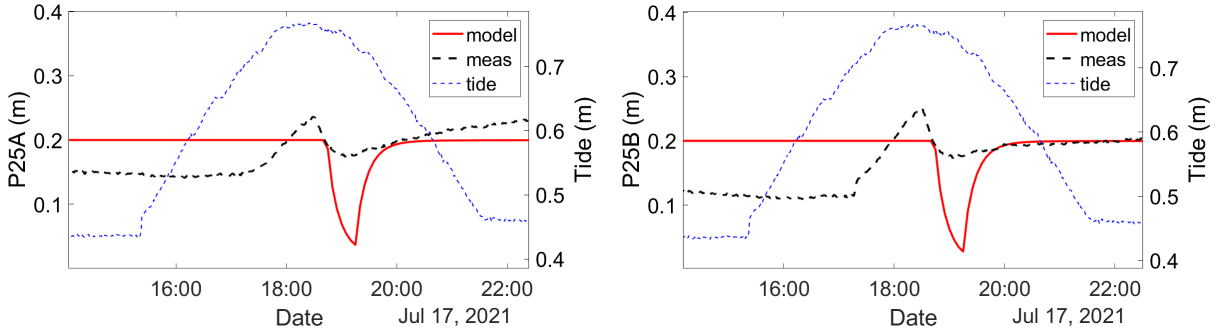

(a) **(b)**

Figure 7.14: Pore-water pressure evolution (left axis), during the final tank emptying operation, expressed as water level in m during the Campalto experiment the pressure transducer P25A (a) and P25B (b) plotted with the tidal fluctuations (right axis). Model results are expressed in red, measures with a dashed red line and the tide with a dashed blue line.

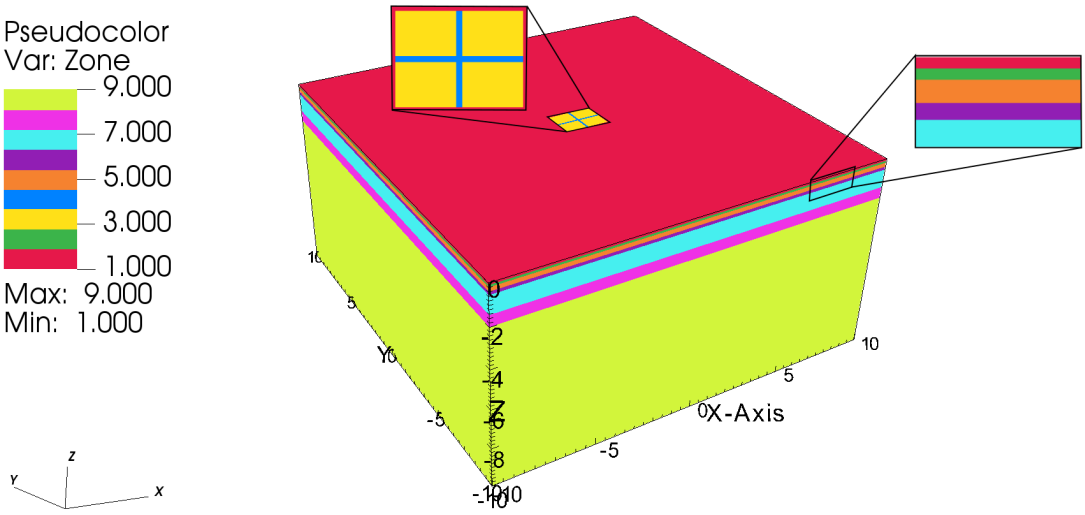

Figure 7.15: Model layering at Le Saline.

7.3 Le Saline

The layering used to represent Le Saline in-situ experiment is composed of 9 materials. Only the two most superficial soil layers (depth ranging from 0 to 0.2 m) are modeled as elasto-plastic materials (Fig. 7.15). The superficial elements corresponding to the wooden pallets and geotexile (represented in yellow and blue, respectively), and the other soil layers are modeled as linear elastic materials. Table 7.3 summarizes the calibrated set of the main parameters used for the simulation for each material and the thickness of the various soil layers. Poisson's ratio ν is set to 0.2 for the soil layers and to 0.15 for the wooden pallets and the geotexile. The porosity is fixed to 0.44 in the whole domain. Preconsolidation stress is initially set to 2 kPa for all the domain, which is lower than the applied load in the two phases.

The E of the nonlinear layers increases with depth. It is equal to 2-3 MPa for intermediate soil layers (depth 0.2-2.0 m) and 20 MPa for the more consolidated material. The evolution of E in the middle of the two nonlinear soil layers below the center of the loading area is depicted in Fig. 7.16. The soil stiffness of the second soil layer is about twice of the one of the first layer. The stiffness of the two most superficial layers during the loading phases is about one order of magnitude smaller than that of the intermediate underlying soil layers.

The hydraulic conductivity k ranges between 10^{-7} and 10^{-4} m/s and it increases with

Material	Depth (m)	k (m/s)	E (MPa)	Constitutive law	s (-)	ν
1. Clayey silt	0-0.10	$9.0 \cdot 10^{-5}$	/	$\frac{1}{C_m} = 6(\sigma_z)^{0.81}$	3.7	0.20
2. Clayey silt	0.10-0.20	$9.0 \cdot 10^{-5}$	/	$\frac{1}{C_m} = 13(\sigma_z)^{0.81}$	2.7	0.20
3. Wood	0-0.01	$5.0 \cdot 10^{-8}$	10^4	/	/	0.15
4. Geotexile	0-0.01	$5.0 \cdot 10^{-8}$	10^4	/	/	0.15
5. Clayey silt	0.20-0.40	$3.0 \cdot 10^{-6}$	2.0	/	/	0.20
6. Sand	0.40-0.55	$3.0 \cdot 10^{-6}$	2.3	/	/	0.20
7. Silty clay	0.55-1.45	$1.0 \cdot 10^{-6}$	2.7	/	/	0.20
8. Silty clay	1.45-2.00	$2.0 \cdot 10^{-7}$	3.0	/	/	0.20
9. Consolidated	2.00-10	$1.0 \cdot 10^{-7}$	20.0	/	/	0.20

Table 7.3: Calibrated set of parameters for the Le Saline model.

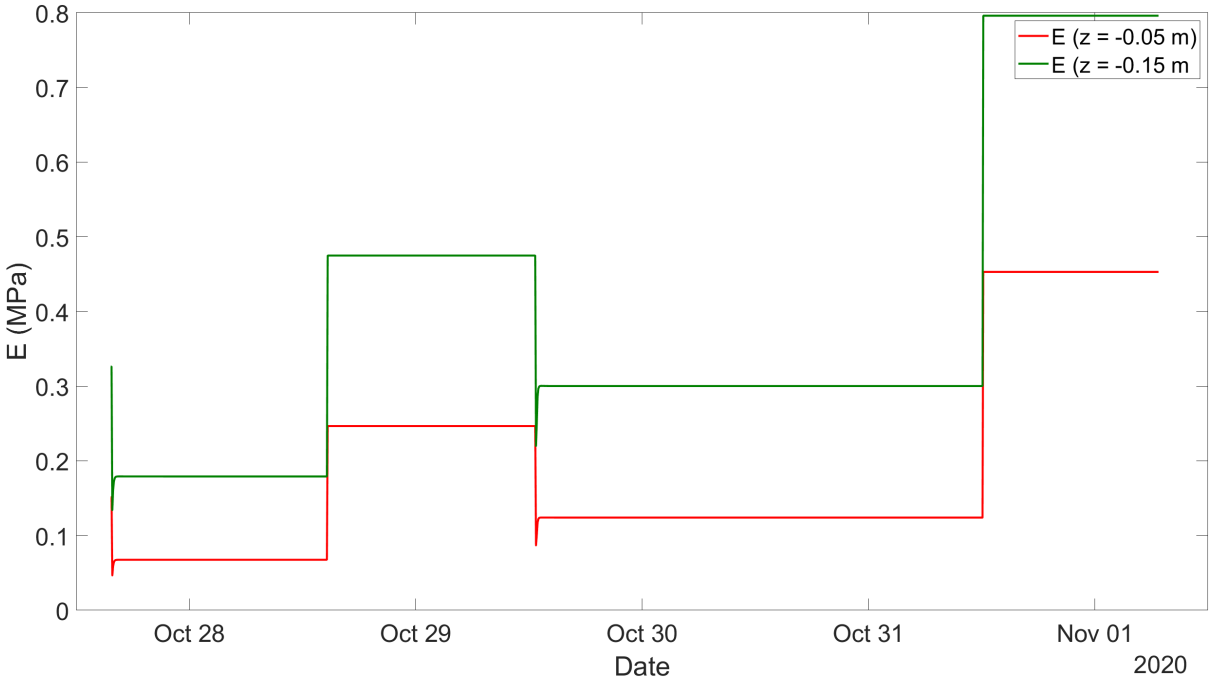

Figure 7.16: Evolution versus time of E in two points located in the middle of the two nonlinear soil layers (depths 0.06 and 0.18 m) below the center of the loading area during the two loading-unloading cycles at the Le Saline experiment. This evolution reflect the case (c) in Fig. 5.5.

depth to match the records of (under)over pressures during the (un)loading cycles. The two most superficial soil layers (material 1 and 2) are much more permeable than the underlying soil layers.

7.3.1 Compaction

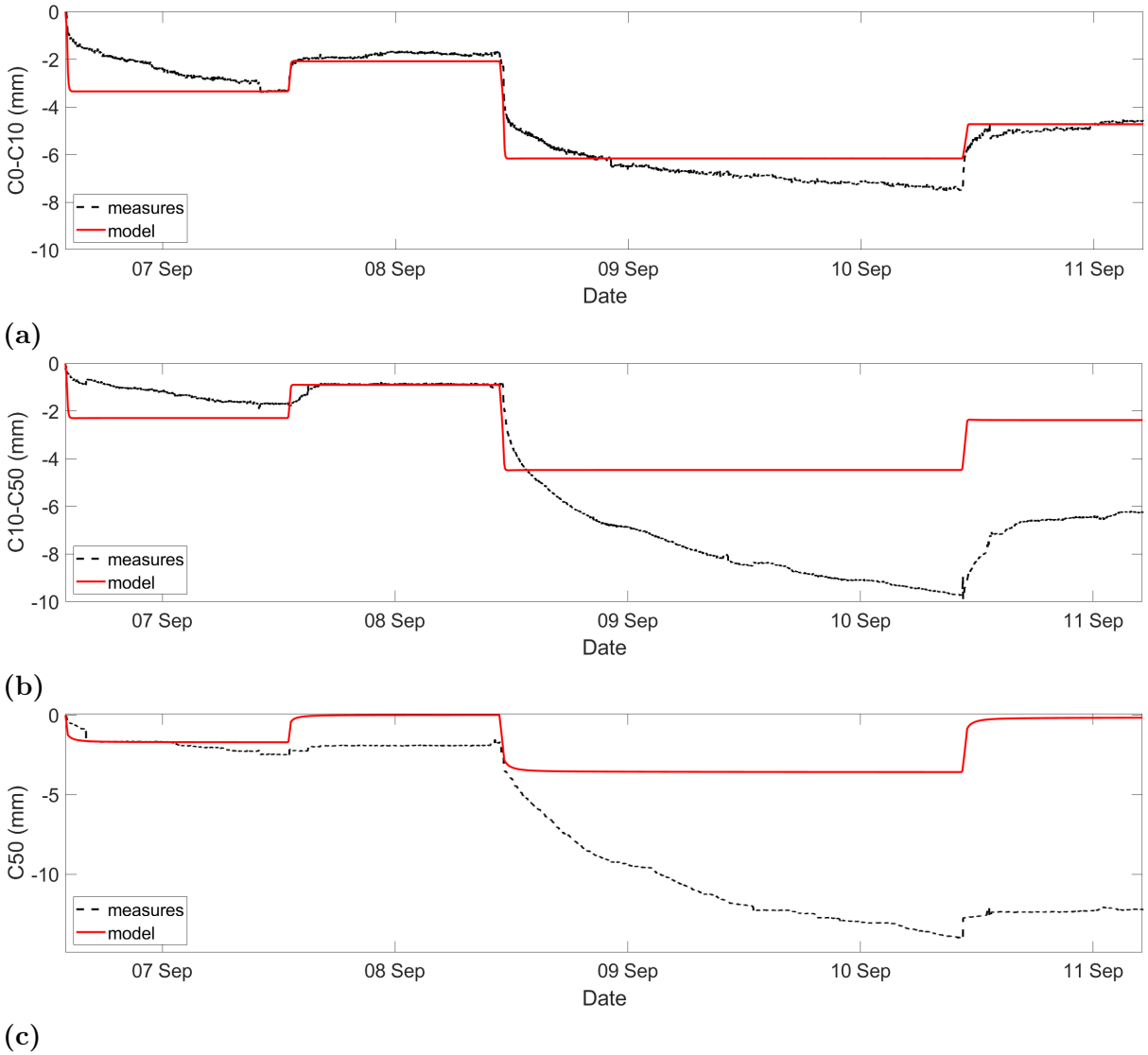

Figure 7.17: Compaction of shallow (C0-C10), intermediate (C10-C50) and deep (C50) soil layers, underneath the center of the loading area during the whole Le Saline experiment. In black the recorded data, in red the model output.

The soil response to the load application, as provided by the model, has been compared with the measured data collected during the in-situ experiment. The comparison has been performed considering the compaction of the shallow (C0-C10), intermediate (C10-C50) and deep (C50) soil layers below the center of the loading area (Fig. 7.17). In the Le Saline experiment, it was not possible to remove the effect of creep process from the

displacement records. Therefore the modeled compaction is directly compared to the plots displayed in Fig. 3.12b.

The simulation is unable to properly replicate the measured vertical compaction of the soil layers during the two loading phases with the exception of the shallowest one (C0-C10). The model underestimates the soil vertical compaction of layers C10-C50 and and the soil at larger depth (C50). However, the recovery phases are well represented for the layers C0-C10 and C10-C50. The model overestimates by a factor equal to 2 the expansion of the deep layers (C50). The measurements are characterized by very small recoveries in both unloading phases, suggesting that a linear elastic constitutive relationship is likely too simple to capture this soil behavior.

7.3.2 Pore-water pressure changes

Also in this case, recorded and simulated pore-water pressure have been expressed into water level (expressed in meters) to compare the two data sets. In this experiment the effect of tide on pore-water pressure can be easily separated from the one related to the load application and removal. The recorded data have been cleaned by the effect of tidal fluctuations on water level. The peaks of water level observed when the load is constant are caused exclusively by tidal oscillation and, therefore, they have been removed. In correspondence of the filling and emptying of the tanks, i.e. variable load, the symmetric water level curve produced by the tide has been subtracted to the asymmetric water level records produced by the combined effect of tidal fluctuations and load (Fig. 3.13), allowing to quantify the isolated effect of the load.

The comparison between the simulated and the observed water level for the six pressure transducers during the experiment is reported in Fig. 7.18. The water level fluctuations measured in correspondence of the laoding-unloading phases are satisfactorily simulated by the model for all the pressure transducers (P25A, P25B, P50A, P50B, P100A, P100B). P50A is located outside the load area and the simulated pressure change is basically zero during the simulation. The dissipation rate of the pore-water pressure is gently overestimated by the model for all the sensors meaning that the field water dynamics is a bit slower. However, a smaller k value, which would allow to match the dissipation rate, results in (over)underpressures much higher than the records (see Section 6).

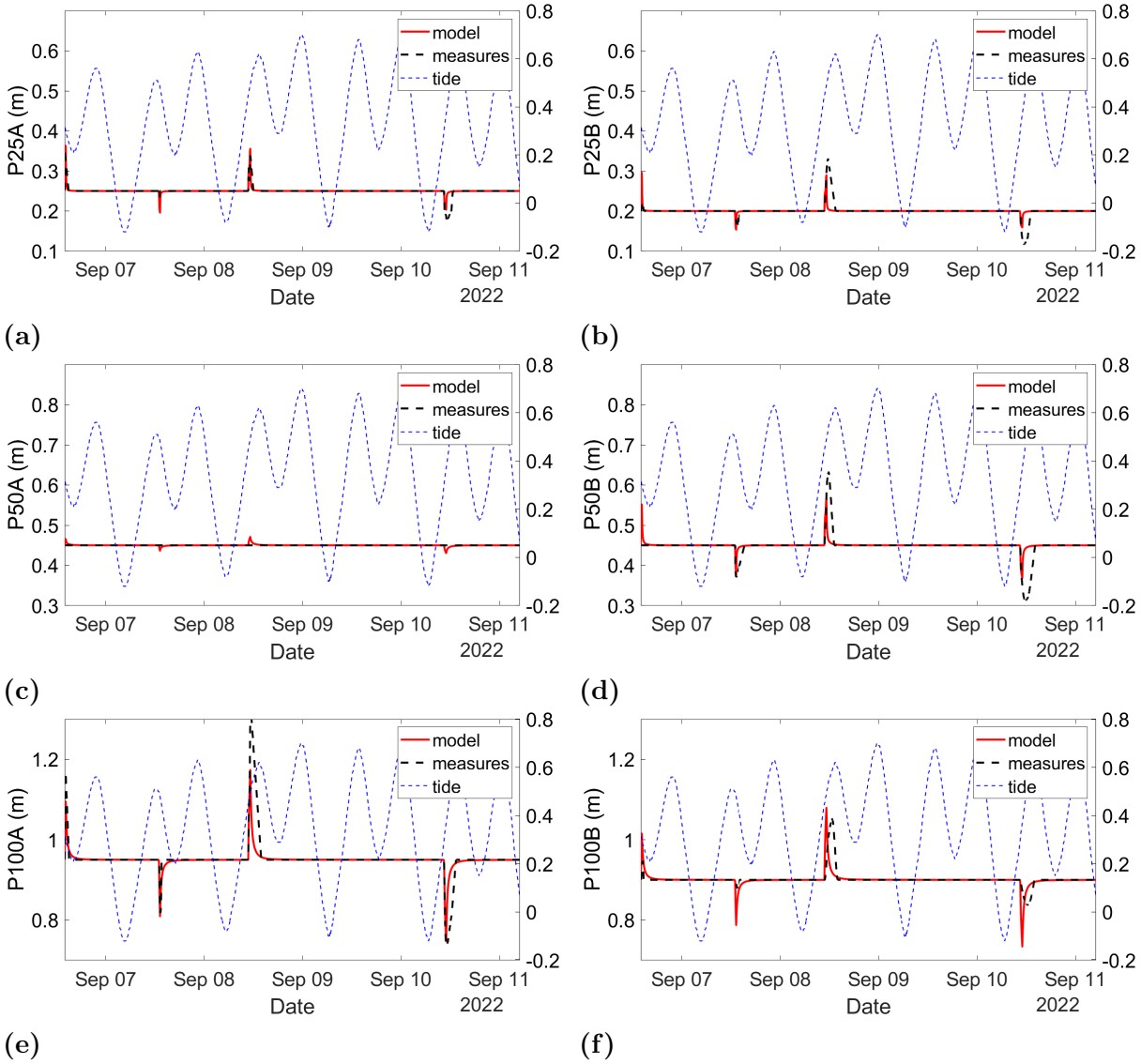

Figure 7.18: Pore-water pressure evolution during the Le Saline experiment for each pressure transducer (P25A, P25B, P50A, P50B, P100A, P100B).

8 Conclusive discussion

Salt marshes are fundamental landforms to preserve the delicate equilibrium of the Venice Lagoon. A main determining factors for coastal marsh survival under relative sea level (RSL) rise is their ability to thicken following the sea rise. This implies that the marsh body must be able to carry the load exerted on their surface by new (natural or artificial) sediments. This thesis aims to characterize the hydro-geomechanical response of shallow marsh deposits in the Venice Lagoon. The results of three in-situ experiments, designed to resemble a lab oedometric test, geologic surveys, geotechnical investigations and portable loading tests have been analysed in three sites, namely La Grisa, Campalto and Le Saline. The primary consolidation of the marsh soil has been investigated by reproducing the loading experiments by means of a poromechanical model based on mixed finite elements. Secondary consolidation has also been estimated from the recorded displacements.

The experimental results demonstrate that, within the same coastal system, the soil compressibility is spatially highly variable and largely depends on the characteristics of the soil that composes the marsh landform, i.e. on the specific depositional environments where a marsh grows and thickens. The vertical settlements observed during the in-situ loading experiment at Campalto are significantly smaller than the other two sites for both the loading phases while the rebounds during the unloading phases are the largest between the three experiments, thus suggesting that here the soil has already experienced a larger preconsolidation. The displacements records at Le Saline are characterized by a particular behavior, i.e. by a very smooth and unclear transition between primary and secondary consolidation, that differs significantly from the other two sites. This could be associated to the recent formation of this salt marsh. Also, the pore water pressure behavior varies from site to site even if the loading-unloading phases are the same. The portable loading tests results highlight that soil compaction can vary even within the same salt marsh due to soil heterogeneity.

The cross-comparison of results from laboratory tests, and the loading experiments in the field (La Grisa and Campalto) allows to evaluate the pros and cons of the in-situ testing approach. The general consistency between field and lab quantifications demonstrates that the designed loading test ensures the validity of the oedometric assumption, i.e.

vertical deformation with no lateral expansion (detailed explanation is in Subsection 3.4.4). Laboratory and in-situ loading tests highlight that soil is more deformable during loading than during unloading, as only a part of the deformation is reversible. However, the results of lab oedometric tests carried out on the samples collected in two sites suggest s ∼5-20 (ratio between compressibility under loading and unloading conditions), with a decreasing trend with depth while results achieved from the in-situ tests (both at large and small scale) suggest values of s ∼2, being the rebounds after the load removal ∼ 40-50 % of the compaction.

In the in-situ loading tests at La Grisa and Campalto, a creep behavior has been pointed out because of the long duration of the constant loading phases. It develops after the dissipation of pore overpressure (causing primary compression) following an increase in loading. Referring to the second loading phase at La Grisa, the C_α coefficient, amounts to 0.026 and 0.013 for the shallow (surface to 0.1 m) and the deeper (0.1 m to 0.4 m) depth intervals, respectively. At Campalto, C_α during the second loading phase is equal to 0.025 and 0.006 for the shallow (surface to 0.1 m) and the deeper (0.1 m to 0.5 m) depth intervals, respectively. At Le Saline the creep effect is even more evident form the recorded displacements but the observed smooth transition between primary and secondary consolidation does not allow a proper evaluation of C_α. This could be associated to the recent formation of this salt marsh.

A poromechanical simulator, based on mixed finite elements, has been applied to simulate the primary consolidation process (creep process is not represented) during the three loading experiments and to quantify the most important hydro-geomechanical parameters. The two most important hydro-geomechanical parameters are the soil stiffness E and the hydraulic conductivity k.

In the three simulations E has been defined with a nonlinear elasto-plastic constitutive law for shallow depth (surface to ∼0.2-0.3 m) as a function of preconsolidations stress σ_p, effective stress σ_z, and s. A linear elastic constitutive relationship has been used for deeper depth intervals (from ∼0.2-0.3 m to the domain bottom). Each simulation has been carried out with a 3D domain discretization that allows to reproduce the soil stratigraphy obtained from geological surveys. The parameters calibration allows to match the records of vertical displacements and pressures during the in-situ experiments.

The model application on the three experiments highlight that the three salt marshes are characterized by different stiffness especially considering the shallow depth intervals. Campalto is the stiffest followed by Le Saline and La Grisa. However, some peculiarities are in common between the three simulations. Modeled E decreases with depth and the E of the shallow elasto-plastic layers (surface to ∼0.25 m) is about one order of magnitude larger than that of the underlying layers. In the three cases the modeled E ranges between 0 and 1 MPa in the two shallowest layers and it is equal to 2-4 MPa in the underlying layers. Generally, in the three cases the implementation of the nonlinear constitutive law allows a good simulation of the vertical soil compaction of the shallow layers while the linear elastic constitutive law implemented in deeper layer is generally too simple to represent the recorded vertical displacements.

To mimic soil compaction behavior three different initial σ_p have been selected for the three simulations. σ_p equal to 2, 4 and 8 kPa have been selected, respectively for Le Saline, La Grisa and Campalto experiment. However, a single value of σ_p for the whole domain, as the simulation allows to use, seems to be not enough to represent the compaction properties of soil layers located at different depths and characterized by different initial degrees of consolidation.

Regarding the hydraulic parameters, k plays a fundamental role in the model for the evolution of the (under)overpressure during the (un)loading phases. The modeled k (assumed to be isotropic) for Le Saline and La Grisa simulations is $\sim 10^{-4}$ m/s for the shallow soil (surface to ∼0.2-0.3 m) and it decreases with depth, meaning that underlying soil layers are less permeable than the shallow ones. For example (Table 7.1), in La Grisa simulation the conductivity of the soil layer within depths 0.23-0.55 m is one order of magnitude lower than the k characterizing the most shallow layers (surface to 0.23 m). Conversely, in Campalto simulation, shallow (surface to 0.3 m) conductivity is lower than in the intermediate layers (0.3-0.6 m) to match pressure records. A summary of the calibrated parameters as obtained by this thesis is reported in Table 8.2. Table 8.1 summarize the simulated soil stiffness of the nonlinear elasto-plastic soil layers during loading-unloading cycles of the three experiments.

Notice that in the modeling procedure the correct evaluation of the creep deformations is fundamental since the model is not able to simulate viscous deformations. At Le Saline,

it was not possible to quantify properly the creep displacements, therefore matching the recorded vertical compaction not cleaned by creep deformation is not possible with the selected model. Similar considerations can be done for the pressures evolution which is affected by tidal oscillation. For an accurate simulation of the groundwater pressure fluctations the effect of tidal oscillation must be quantified accurately. An attempt about removing the effect tidal oscillation on pressure fluctuations by the effect of the load has been made in this thesis for the Le Saline experiment (Fig. 7.18a). However a further development on this procedure is needed for a more accurate simulation of pore-water pressures.

Next steps of this study will be focused on the implementation of a constitutive law able to model also creep deformations (visco-elasto-plastic constitutive law) and on a better understanding of tidal oscillation on pore-water pressure fluctuations for a more accurate simulation of the consolidation process in these soft soils.

	E (MPa) during the La Grisa loading-unloading phases				
Depth (m)	I load	I unload	II load	II unload	σ_p (kPa)
0.06	0.04	0.10	0.05-0.06	0.16	4.0
0.18	0.08	0.16	0.1-0.13	0.26	4.0
	E (MPa) during the Campalto loading-unloading phases				
Depth (m)	I load	I unload	II load	II unload	σ_p (kPa)
0.05	0.25	0.25	0.1	0.25	8.0
0.20	0.58	0.58	0.32	0.58	8.0
	E (MPa) during the Le Saline loading-unloading phases				
Depth (m)	I load	I unload	II load	II unload	σ_p (kPa)
0.06	0.06-0.07	0.25	0.10-0.13	0.48	2.0
0.18	0.15-0.19	0.50	0.22-0.30	0.80	2.0

Table 8.1: Summary of the evolution of E, underneath the loading area, during the loading-unloanding phases of the three experiments in the centroids of the two uppermost soil layers modeled using an nonlinear elasto-plastic constitutive law. Also, the value of preconsolidation stress for the three simulations is reported.

	La Grisa		Campalto		Le Saline	
Layer (m)	k (m/s)	E (MPa)	k (m/s)	E (MPa)	k (m/s)	E (MPa)
Shallow	$2.5 \cdot 10^{-4}$	0.04-0.26	$1.0 \cdot 10^{-6}$	0.10-0.58	$9.0 \cdot 10^{-5}$	0.06-0.80
Intermediate	$10^{-5} - 10^{-6}$	3.00	$7.0 \cdot 10^{-5}$	4.00	10^{-6}	2.00
Deep	10^{-7}	20.00	10^{-7}	20.00	10^{-7}	20.00

Table 8.2: Summary of the two most important geomechanical parameters (k and E) derived from the three simulations in the shallow (depth from surface to ∼0.25 m) , intermediate (depth between ∼0.25-2.00 m) and deep (depth between ∼2.00-10.00 m) layers of the domain.

References

[1] D. M. Alongi. "Carbon Balance in Salt Marsh and Mangrove Ecosystems: A Global Synthesis". In: *Journal of Marine Science and Engineering* 8.10 (2020). DOI: 10.3390/jmse8100767.

[2] J. Adams et al. "Salt Marsh Restoration for the Provision of Multiple Ecosystem Services". In: *Diversity* 13 (Dec. 2021), p. 680. DOI: 10.3390/d13120680.

[3] S. E. King and J. N. Lester. "The value of salt marsh as a sea defence". In: *Marine Pollution Bulletin* 30.3 (1995), pp. 180–189. DOI: https://doi.org/10.1016/0025-326X(94)00173-7.

[4] I. Valiela et al. "Global Losses of Mangroves and Salt Marshes". In: Jan. 2009, p. 22.

[5] S. Silvestri and M. Marani. "Salt-Marsh Vegetation and Morphology: Basic Physiology, Modelling and Remote Sensing Observations". In: *The Ecogeomorphology of Tidal Marshes, Coastal Estuarine Stud.* 59 (Mar. 2013). DOI: 10.1029/CE059p0005.

[6] M. J. Brain et al. "Exploring mechanisms of compaction in salt-marsh sediments using Common Era relative sea-level reconstructions". In: *Quaternary Science Reviews* 167 (2017), pp. 96–111. DOI: https://doi.org/10.1016/j.quascirev.2017.04.027.

[7] K. L. Jankowski, T. E. Törnqvist, and A. M. Fernandes. "Vulnerability of Louisiana's coastal wetlands to present-day rates of relative sea-level rise". In: *Nature Communications* 8.1 (2017), p. 14792.

[8] C. Da Lio et al. "Understanding land subsidence in salt marshes of the Venice Lagoon from SAR Interferometry and ground-based investigations". In: *Remote sensing of environment* 205 (2018), pp. 56–70.

[9] M. J. Brain et al. "Compression behaviour of minerogenic low energy intertidal sediments". In: *Sedimentary Geology* 233.1 (2011), pp. 28–41. DOI: https://doi.org/10.1016/j.sedgeo.2010.10.005.

[10] H. Brooks et al. "How strong are salt marshes? Geotechnical properties of coastal wetland soils". In: *Earth Surface Processes and Landforms* 47.6 (2022), pp. 1390–1408. DOI: https://doi.org/10.1002/esp.5322.

[11] M. J. Brain et al. “Modelling the effects of sediment compaction on salt marsh reconstructions of recent sea-level rise”. In: *Earth and Planetary Science Letters* 345-348 (2012), pp. 180–193. DOI: https://doi.org/10.1016/j.epsl.2012.06.045.

[12] C. Zoccarato et al. “In-situ loading experiments reveal how the subsurface affects coastal marsh survival”. In: *Communications Earth Environment* 3 (Nov. 2022). DOI: 10.1038/s43247-022-00600-9.

[13] J.R.L. Allen. “Morphodynamics of Holocene salt marshes: a review sketch from the Atlantic and Southern North Sea coasts of Europe”. In: *Quaternary Science Reviews* 19.12 (2000), pp. 1155–1231. DOI: https://doi.org/10.1016/S0277-3791(99)00034-7.

[14] C.L. Amos et al. “The coastal morphodynamics of Venice lagoon, Italy: An introduction”. In: *Continental Shelf Research* 30.8 (2010). The Coastal Morphodynamics of Venice Lagoon and its Inlets, pp. 837–846. DOI: https://doi.org/10.1016/j.csr.2010.01.014.

[15] S. Cola and P. Simonini. “Mechanical behavior of silty soils of the Venice lagoon as a function of their grading characteristics”. In: *Canadian Geotechnical Journal* 39.4 (2002), pp. 879–893. DOI: 10.1139/t02-037.

[16] A. Bondesan and P. Furlanetto. “Artificial fluvial diversions in the mainland of the Lagoon of Venice during the 16th and 17th centuries inferred by historical cartography analysis”. In: *Géomorphologie: relief, processus, environnement* 18.2 (2012), pp. 175–200.

[17] Z. Zhu, Z. Yang, and T. J. Bouma. “Biomechanical properties of marsh vegetation in space and time: effects of salinity, inundation and seasonality”. In: *Annals of Botany* 125.2 (May 2019), pp. 277–290. DOI: 10.1093/aob/mcz063.

[18] A. Verruijt. *PoroElasticity Theory and Problems*. 2008.

[19] K. Terzaghi. *Erdbaumechanik auf bodenphysikalischer Grundlage*. F. Deuticke, 1925.

[20] M. A. Biot. “General Theory of Three-Dimensional Consolidation”. In: *Journal of Applied Physics* 12.2 (Apr. 2004), pp. 155–164. DOI: 10.1063/1.1712886.

[21] M. A. Biot. “Consolidation Settlement Under a Rectangular Load Distribution”. In: *Journal of Applied Physics* 12.5 (Apr. 2004), pp. 426–430. DOI: 10.1063/1.1712921.

[22] A. Verruijt. "Darcy's Law". In: *Theory of Groundwater Flow*. London: Macmillan Education UK, 1970, pp. 6–13. DOI: 10.1007/978-1-349-00175-0_2.

[23] C. Janna et al. "A geomechanical transversely isotropic model of the Po River basin using PSInSAR derived horizontal displacement". In: *International Journal of Rock Mechanics and Mining Sciences* 51 (2012), pp. 105–118. DOI: https://doi.org/10.1016/j.ijrmms.2012.01.015.

[24] M. Ferronato, N. Castelletto, and G. Gambolati. "A fully coupled 3-D mixed finite element model of Biot consolidation". In: *Journal of Computational Physics* 229.12 (2010), pp. 4813–4830. DOI: https://doi.org/10.1016/j.jcp.2010.03.018.

[25] N. Castelletto, J. A. White, and M. Ferronato. "Scalable algorithms for three-field mixed finite element coupled poromechanics". In: *Journal of Computational Physics* 327 (2016), pp. 894–918. DOI: https://doi.org/10.1016/j.jcp.2016.09.063.

[26] R. W. Lewis and B. A. Schrefler. "The finite element method in the deformation and consolidation of porous media". In: (1987).

[27] H. A. van der Vorst. "Bi-CGSTAB: A Fast and Smoothly Converging Variant of Bi-CG for the Solution of Nonsymmetric Linear Systems". In: *SIAM Journal on Scientific and Statistical Computing* 13.2 (1992), pp. 631–644. DOI: 10.1137/0913035.

[28] M. Ferronato, G. Pini, and G. Gambolati. "The role of preconditioning in the solution to FE coupled consolidation equations by Krylov subspace methods". In: *International Journal for Numerical and Analytical Methods in Geomechanics* 33.3 (2009), pp. 405–423. DOI: https://doi.org/10.1002/nag.729.

[29] N. Castelletto, G. Gambolati, and P. Teatini. "A coupled MFE poromechanical model of a large-scale load experiment at the coastland of Venice". In: *Computational Geosciences* 19 (2015). DOI: 10.1007/s10596-014-9450-y.